SAPIENZA
UNIVERSITÀ DI ROMA

Scuola di Dottorato "Vito Volterra"
Dottorato di Ricerca in Fisica – XXII ciclo

High energy neutrino detection with the ANTARES underwater Čerenkov telescope

Thesis submitted to obtain the degree of
Doctor of Philosophy ("Dottore di Ricerca") in Physics
October 2009

by

Manuela Vecchi

Program Coordinator
Prof. Vincenzo Marinari

Thesis Advisors
Prof. Antonio Capone
Dr. Fabrizio Lucarelli

to my parents

Contents

Introduction

Cosmic rays were discovered a century ago, but it is still uncertain *where* and *how* they are accelerated: since the Universe is opaque to very high energy photons, with energies higher than about 100 TeV, *traditional* astronomy cannot be successfully used to solve this puzzle.
Multi-messenger astronomy is a very promising field of research in which photons are not the only probes, but the information coming from cosmic rays, neutrinos and gravitational waves are also used.
Charged particles, whose paths are deflected by magnetic fields, cannot carry the information on the arrival direction up to ultra high energies, so that a close look at production and acceleration sites of cosmic rays is only possible with neutral and weakly interacting particles.
Neutrinos are thought to be produced in the interaction of accelerated particles (protons and nuclei) with matter and radiation surrounding the sources. In these interactions a massive production of hadrons with short lifetime (mostly pions and kaons, both charged and neutral) is expected to take place: charged pions decays produce ν_e and ν_μ in the final state. Because of neutrino flavor oscillations, we expect ν_e, ν_μ and ν_τ, together with their antiparticles, to arrive on Earth with equal fluxes.
The identification of sources producing neutrinos with energies higher than some TeV could thus provide an unambiguous key for the identification of Cosmic Rays acceleration sites. Neutral hadrons, produced along with the charged particles generating neutrinos, are expected to decay into couples of high energy photons, so that astrophysical sources which are simultaneous emitters of neutrinos and γ-rays are very likely to exist.
Potential sources of high-energy neutrinos include supernova remnants, binary systems, e.g. microquasars, active galactic nuclei and gamma-ray bursts: the detection of neutrinos from such sources will shed light on the physical processes involved in their creation.
The recent results obtained by the Pierre Auger Collaboration indicate the existence of ultra high energy protons acceleration sites along or nearby the supergalactic plane. Several models indicate these sites as possible candidate for high energy neutrino production.

This PhD thesis work has been developed within the ANTARES Collaboration, that has completed the realization of the largest high energy neutrino telescope currently operating in the Northern hemisphere.
The ANTARES Collaboration has realized an underwater neutrino telescope with

an area of about 0.1 km^2, aiming to search for high-energy muon neutrinos originating from galactic and extra-galactic sources. The detection principle relies on the observation of Čerenkov light, whose emission is stimulated by the propagation in water of the charged leptons resulting from charged current neutrino interactions in the medium surrounding the apparatus. The detector is a 3-dimensional array of photomultiplier tubes, arranged on twelve vertical lines, placed at a depth of about 2500 meters, 40 km off the coast of Toulon, France. The telescope was completed in May 2008 and it has been working in its 12-lines configuration for almost one year. The detection of neutrinos is based on the identification of muons which are created in the charged-current interactions of muon-neutrinos. These muons, at sufficiently high-energies, retain information on the direction of the incident neutrino and can traverse several kilometers of sea water. From the measured arrival time of the Čerenkov light, the direction of the muon can be determined and the neutrino arrival direction can be identified.
Data collected during 2007, when the detector was only composed by 5 lines, have been analyzed and compared to Monte Carlo expectations, in order to study the distribution of neutrino arrival directions over an extended region of the sky that surrounds part of the supergalactic plane, where a wide number of candidate sources of high energy neutrinos are located.
Sensitivity studies for the specific analysis concerning the performance of the full ANTARES detector after one year data taking have also been performed.
In this analysis no assumption has been made on the nature of the sources. The idea is to investigate a dense extended region of the sky where huge matter target is expected to give raise to the production of high energy neutrinos.

The thesis is organized as follows:

- In **chapter 1** the sources of astrophysical neutrinos with energies from μeV up to some Joule will be reviewed. Scientific motivations for high energy neutrino astronomy in the context of multi-messenger approach will be also discussed.

- In the first part of **chapter 2** the *state of the art* of neutrino physics will be shortly reported, providing references for a more complete description. In the second part of the chapter the techniques for the detection of astrophysical neutrinos with energies between hundreds of GeV up to several EeV will be outlined.

- In **chapter 3** the ANTARES detector will be described in detail, together with environmental properties of the site where the telescope has been deployed. An evaluation of the biofouling effect at the ANTARES site will be given in section 3.3.

- In **chapter 4** a review of the physics analysis topics that are relevant for the ANTARES telescope will be given. First results obtained in the analysis of 2007 data will be shortly reported.

- In the first part of **chapter 5** the Monte Carlo tools that are used to simulate the signal and background events as well the detector response will be reviewed. In the second part, the two main reconstruction algorithms that are in use

within the ANTARES Collaboration will be described. The *Full Likelihood* algorithm, specifically designed for the search of neutrinos from point-like sources, has been used in the analysis described in the following chapter.

- In the first part of **chapter 6** recent experimental results concerning the arrival directions of ultra high energy cosmic rays will be reported, together with neutrino flux predictions from the same sources. In the second part the survey method will be described, together with results obtained from the analysis of the data collected by the ANTARES experiment during 2007. The study of the sensitivity of the proposed search method for the full ANTARES detector will be also presented, showing results obtained from a one year data taking simulation.

Chapter 1

Neutrino astronomy in the context of multimessenger approach

1.1 Astrophysical Neutrinos

The existence of an electrically neutral half-spin particle was postulated by W. Pauli in 1930, as a *"desperate remedy"* to preserve conservation of energy and momentum in beta decay. Enrico Fermi named this particle the *neutrino* in 1934, within the formulation of his theory for beta decay.
In 1942 K.C. Wang first suggested the use of beta-capture to detect neutrinos and in 1956 electron neutrinos were detected for the first time by F. Reines [1], C. Cowan *et al*, observing the inverse beta decay produced by anti-neutrino interactions.
In 1962 muon neutrinos were discovered by L.M. Lederman, M. Schwartz and J. Steinberger [2], while the first direct detection of tau neutrino was announced in summer of 2000 by the DONUT collaboration at Fermilab, making it the latest particle of the Standard Model to have been directly observed.
Being electrically neutral leptons, neutrinos are only weakly interacting particles: for these reasons direct neutrino detection has always been a challenging task.
Great interest in neutrino physics was raised by the discovery of lepton flavor non-conservation. The first hints for this phenomenon date back to the late 1960s, when several experiments found that the number of electron neutrinos arriving from the Sun was between one third and one half of the number predicted by the Standard Solar Model [34], a discrepancy which became known as the *solar neutrino problem*, and remained unresolved for about thirty years.
The Standard Model of particle physics formerly assumed that neutrinos were massless and couldn't change flavor. As a consequence of the observed flavor oscillations we have to assume that neutrinos are massive particles. The absolute mass scale is still not completely understood, since oscillation experiments are only sensitive to the difference of the squared values of neutrino masses. The mechanism responsible

[1] Nobel Prize in Physics 1995 "for the detection of the neutrino".
[2] Nobel Prizes in Physics 1988 "for the neutrino beam method and the demonstration of the doublet structure of the leptons through the discovery of the muon neutrino".

for the generation of the neutrino masses can neither be investigated using oscillation experiments.
Being neutral fermions, neutrinos could be described by a Majorana field, instead of the usual Dirac field used to describe charged fermions. If this condition is verified, neutrinos are indistinguishable from their own anti-particles and lepton number is not conserved: a striking difference with respect to what is expected in the Standard Model of particle physics.

Neutrinos are very abundant in the Universe, playing an important role in many

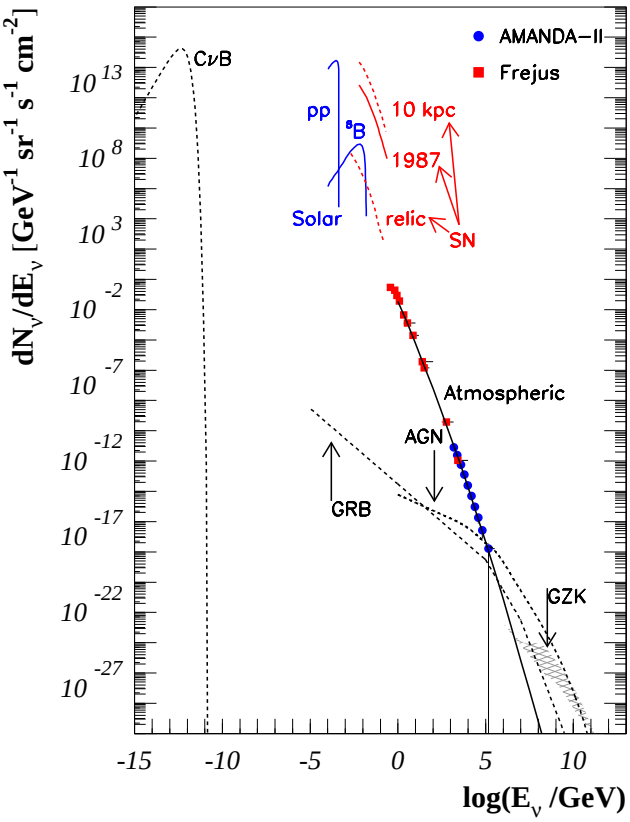

Figure 1.1. Astrophysical neutrinos spectrum ranging from μeV to EeV energies [43]. The fluxes based on mere predictions are shown as dashed lines, the solid lines represent measured fluxes, while the atmospheric neutrino data are from the FREJUS and AMANDA experiments.

astrophysical and cosmological mechanisms: figure 1.1 shows the energy spectrum of astrophysical neutrinos that extends over more than twenty orders of magnitude in both energy and intensity.
Cosmological $sub-eV$ neutrinos, the relic left over from the early epochs of the Universe, have a density of about $56\,cm^{-3}$ (for each neutrino species), and a black-body spectrum with a temperature $T_\nu \simeq 1.947K$.
Neutrinos are also produced in several thermonuclear reactions occurring in the Sun,

with energies around MeV. Picture 1.2, a neutrino heliograph, shows neutrinos from the Sun detected by the Super Kamiokande experiment.
Core-Collapse Supernovae produce bursts of neutrinos of energies $E \sim 10 \div 25 MeV$. Neutrinos are produced in stars with masses not smaller than the solar mass, as a

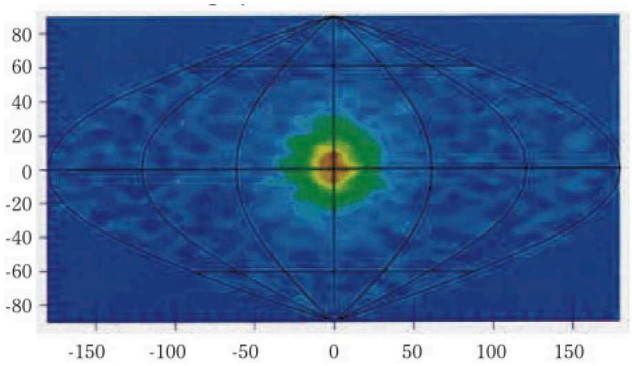

Figure 1.2. Neutrino heliograph from Super Kamiokande. Picture from Kamioka Observatory pamphlet 2006, Institute for Cosmic Ray Research, the University of Tokio, Japan (available at http://www-sk.icrr.u-tokyo.ac.jp/lib).

consequence of the catastrophic phenomena occurring when the stellar iron core is no longer supported by the electron degeneracy pressure. Stars are stable as long as elements lighter than iron are burnt in nuclear fusion processes. When the *nuclear fuel* is no longer available, stars become unstable and collapse. The compressed core heats, producing energetically favorable conditions to capture electrons on free protons in the *neutronization* process:

$$p + e^- \rightarrow n + \nu_e \tag{1.1}$$

These reactions generate a burst of neutrinos that rapidly escape from the core.
Supernova *SN 1987A* occurred approximately 50 kpc from Earth, in the outskirts of the *Tarantula Nebula* in the *Large Magellanic Cloud*, a nearby dwarf galaxy. Approximately three hours before the visible light from SN 1987A reached the Earth, a burst of neutrinos was observed at three separate neutrino observatories.
On the 23rd of February 1987, at 7:35am Universal time, Kamiokande II detected 11 antineutrinos, IMB 8 antineutrinos and Baksan 5 neutrinos, in a burst lasting less than 13 seconds. This was the first time that neutrinos emitted from a Supernova had been observed directly, and the observations were consistent with theoretical supernova models in which 99% of the energy of the collapse is radiated away in neutrinos.
At energies greater than hundreds of MeV, neutrinos produced in the interactions of primary Cosmic Rays with the atmosphere constitute the main component of the flux, up to energies of the order of $10^{12} eV$, where astrophysical signal from various galactic and extra-galactic sources start to be predominant.
These latter component of the astrophysical neutrino flux will be discussed in the following sections.

1.2 The multi-messenger connection

The production of cosmic neutrinos of energies higher than some GeV is strongly connected to that of high energy radiation and Cosmic Rays: in the most widely accepted models high energy neutrinos are produced in the interaction of accelerated charged protons (and nuclei) with high energy photons or other hadrons in the vicinity of cosmic rays sources, where shockwave formation occurs, as will be described in paragraph 1.3.1. The main channels for neutrinos and high energy photons production are:

$$p + \gamma \rightarrow \Delta^{+} \rightarrow \begin{cases} p + \pi^{0} \\ n + \pi^{+} \end{cases} \tag{1.2}$$

$$p + p \rightarrow \Delta^{++} \rightarrow \begin{cases} p + p + \pi^{0} \\ n + p + \pi^{+} \end{cases} \tag{1.3}$$

At higher energies also kaons contribute to the spectrum. While the resulting neutrons are likely to interact before decaying, pions decay. Neutral pions decay in two photons, charged pions produce neutrinos of electron and muon flavour, with the decay chains:

$$\pi^{+} \rightarrow \mu^{+} + \nu_{\mu},\ \mu^{+} \rightarrow e^{+} + \nu_{e} + \bar{\nu_{\mu}} \tag{1.4}$$

$$\pi^{-} \rightarrow \mu^{-} + \bar{\nu_{\mu}},\ \mu^{-} \rightarrow e^{-} + \bar{\nu_{e}} + \nu_{\mu} \tag{1.5}$$

Assuming that the same amount of π^{+} and π^{-} is produced, the production flavor ratio of neutrinos at the source is the following:

$$(\nu_{e} : \nu_{\mu} : \nu_{\tau}) = (\bar{\nu_{e}} : \bar{\nu_{\mu}} : \bar{\nu_{\tau}}) = (1 : 2 : 0) \tag{1.6}$$

Being massive particles, neutrinos have non-zero mass eigenvalues: this implies flavor oscillations [86] from their way from the source to Earth, flavor eigenstates $|\nu_{\alpha}>, \alpha = e, \mu, \tau$ being connected to mass eigenstates $|\nu_{j}>, j = 1, 2, 3$ by the following relation:

$$|\nu_{\alpha}(t)>= \sum_{j=1,2,3} U_{\alpha j} exp(-iE_{j}t)|\nu_{j}> \tag{1.7}$$

where E_j is the eigenvalue for the Hamiltonian in vacuum, i.e. the energy of the mass eigenstate, and $U_{\alpha j}$ the mixing unitary matrix, which is a function of three angles and a phase. The probability for a neutrino to oscillate from a flavor state α to a flavor state β in a time t, starting from the emission of the neutrino at the source, at time $t = 0$,is given by:

$$P_{\nu\alpha \rightarrow \nu\beta} = |<\nu_{\beta}(t)|\nu_{\alpha}(t=0)>|^{2} = \delta_{\alpha\beta} - 4\sum_{j>1} U_{\alpha i}U_{\beta i}U_{\alpha j}U_{\beta j} sin^{2}(\frac{\delta m_{ij}^{2} L}{4E_{\nu}}) \tag{1.8}$$

The flavor transition probability depends on several parameters: the mixing matrix elements, the neutrino energy E, the distance L between the production and the interaction point, and the difference of neutrino squared masses. In particular the oscillation probability vanishes for massless neutrinos.
The sin^2 term in equation 1.8 depends on the experimental conditions. If the argument of this term approaches to zero, the transition probability vanishes. If instead

it is much greater than one, as it is the case for the detection of high energy neutrinos from astrophysical sources, uncertainties on the measurement of L and E result in this term to be averaged to $\frac{1}{2}$, the transition probability being dependent only on the mixing matrix elements.
We can obtain the composition of a neutrino flavor vector observed at Earth, starting from the vector at the source $(\nu_e^{source}, \nu_\mu^{source}, \nu_\tau^{source}) = (1, 2, 0)$. Using the probability matrix described above, we obtain $(\nu_e^{Earth}, \nu_\mu^{Earth}, \nu_\tau^{Earth}) = (1, 1, 1)$ for path length bigger than the size of the Solar System: an equal number of electron, muon and tau neutrinos are expected to be observed at Earth.
High energy neutrinos have not been observed yet, their detection being challenging due to both the low fluxes expected, as seen in figure 1.1, and the low probability of interaction with matter, as described in chapter 2.2. Being neutral and only weakly interacting particles, they can keep the information on their source position, making *neutrino astronomy* feasible, moreover providing an unambiguous proof of the occurrence of hadronic mechanisms inside Cosmic Rays (CRs) sources.
Neutrino flux predictions are based on the direct connection between the observed CRs and the non-thermal radiation from astrophysical sources.
Neutrino astronomy plays a fundamental role in the energy range between $100\,GeV$ and $10\,PeV$, where charged CRs are deflected by magnetic fields, and electromagnetic radiation starts to be absorbed in the interaction with the matter targed traversed. Combining informations obtained detecting Cosmic Rays, electromagnetic radiation, neutrinos and, in the near future, gravitational waves, several astronomical and physical aspects will be understood in detail: this is the goal of *multi-messenger astronomy.*
The spectrum of hadronic CRs observed at Earth is shown in figure 1.3, covering approximately 11 orders of magnitude up to $E \simeq 10^{20}\ eV$. This spectrum can be approximated by a broken power law ($\Phi \sim E^{-\alpha}$). The most important spectral features are the transition regions: the "Knee" at $E \simeq 3 \times 10^{15}$ eV, where the spectrum steepens from a slope $\alpha \simeq 2.7$ to $\alpha \simeq 3$, and the "Ankle" at $E \simeq 10^{19}$ eV, where the spectrum flattens to $\alpha \simeq 2.7$ [83].
At $E \simeq 6 \times 10^{19}$ eV there is now clear evidence (from the HiRes [1] and Auger [6] collaborations) of a sharp steepening of the spectrum, as can be seen in figure 1.4. This process, the so-called *GZK cut-off*, was predicted in the 60's by Greisen [74], Zatsepin and Kuzmin [127]: it is visible at energies higher than the threshold value needed for the pion photoproduction in the interaction between ultra high energy protons or nuclei and the Cosmic Microwave Background Radiation, at temperature of 2.725 K, corresponding to an energy of 0.25 eV.
The so called *second Knee*, at $E \simeq 4 \times 10^{17}$ eV, has recently emerged as potentially very significant, corresponding to the a less evident steepening with the slope increasing from $\alpha \simeq 3$ to approximately 3.3.
Explanations for the origin of the *Knee*, the *second Knee* and the *Ankle* are still disputed, and are considered as of central importance in cosmic rays physics.
Most of the observed CRs are *galactic*, confined by galactic magnetic fields around the visible disk of the Milky Way. Extragalactic space should also be filled by a gas of CRs, produced by the ensemble of all sources in the Universe during their cosmological history. All galaxies should be sources of CRs, as the particles that *leak out* of magnetic confinement are injected into extragalactic space. The extra-galactic

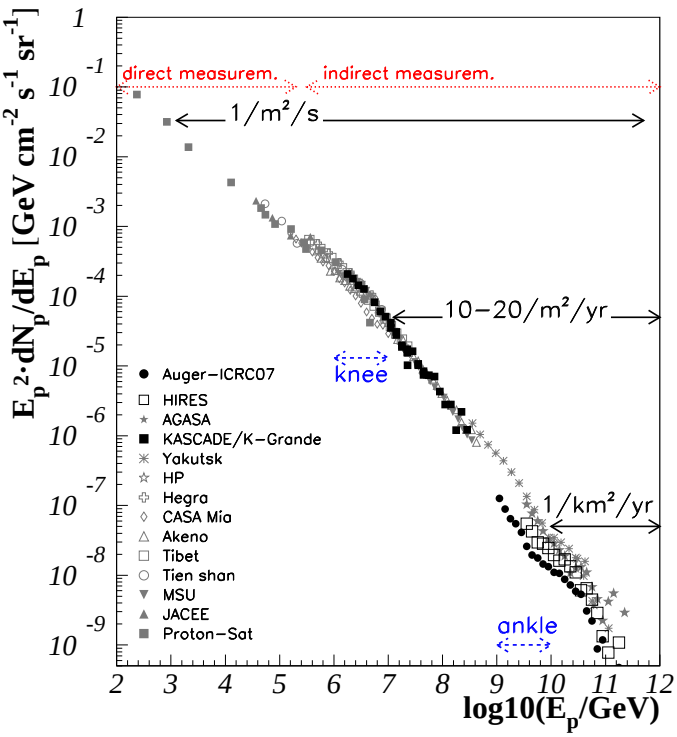

Figure 1.3. Spectrum of the differential flux of Cosmic Rays measured at Earth [43].

component is expected to have a harder energy spectrum, and should emerge above the foreground of galactic CRs at sufficiently high energies. The determination of a "transition energy" that marks the point where the extragalactic CR component becomes dominant is also a highly debated issue.

1.3 Galactic Sources of High Energy Neutrinos

Ultrarelativistic charged particles produced inside our Galaxy remain trapped by the galactic magnetic field, that has a typical strength $B \simeq 3\,\mu Gauss$.
The Larmor radius, or gyroradius, of a charged particle of atomic number Z in a magnetic field B is given by [70]:

$$r_{\rm Larmor} = \frac{E}{Z\,e\,B} \simeq \frac{1.08}{Z} \left(\frac{E}{10^{18}\ {\rm eV}}\right) \frac{\mu{\rm Gauss}}{B}\ {\rm kpc} \tag{1.9}$$

Magnetic confinement becomes impossible when the gyroradius is comparable with the linear dimensions of the Galaxy. This corresponds to energy:

$$E \geq Z\,e\,B\,R_{\rm Halo} \simeq 2.7 \times 10^{19}\ Z \left(\frac{B}{3\ \mu{\rm Gauss}}\right) \left(\frac{R_{\rm Halo}}{10\ {\rm kpc}}\right) \tag{1.10}$$

Most CR particles have much lower energy and a gyroradius that is much smaller than the galactic size. The motion of these particles can be well approximated as a

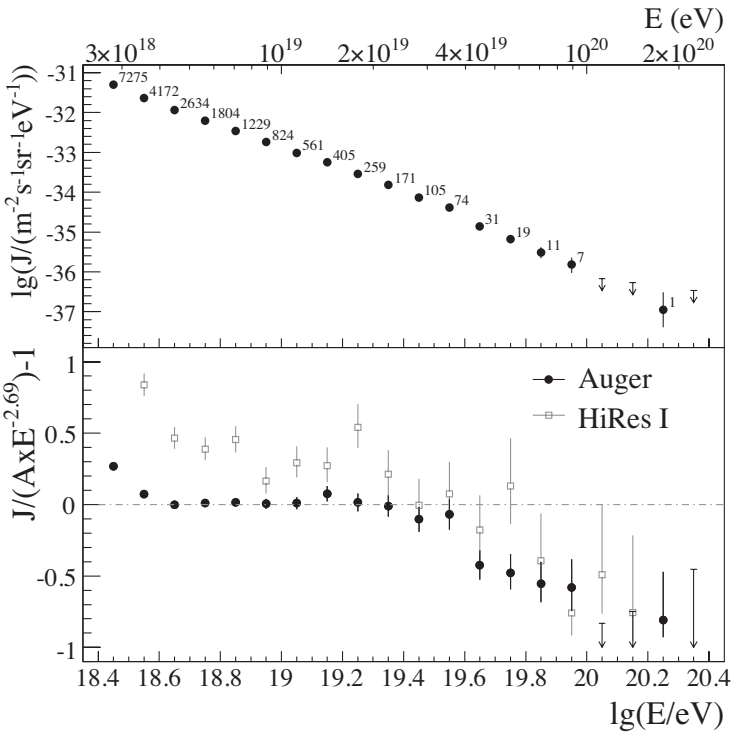

Figure 1.4. Upper panel: The differential flux J as a function of energy, with statistical uncertainties. Lower panel: The fractional differences between Auger and HiResI data compared with a spectrum with an index of 2.69 [6].

diffusive process controlled by the random component of the galactic magnetic field. The time needed for a CR particle to diffuse out of the galactic halo is a function of its rigidity (which is given by E/Z for ultra-relativistic particles). An important consequence is that (assuming stationarity) the number $N_A(E)$ of CRs of type A and energy E in the Galaxy is:

$$N_A(E) \simeq Q_A(E)\ \tau(E/Z) \tag{1.11}$$

where $Q_A(E)$ is the injection rate and $\tau(E/Z)$ is the confinement time. Therefore the observed CRs spectrum has not the same energy distribution of the particles near their sources, but is distorted and steepened by confinement effects.
Relative abundances of "secondary nuclei" (such as Lithium, Beryllium and Boron) in the CRs are used to evaluate the confinement time τ: these nuclei are rare in the Solar System, since they are almost absent in final phases of the stellar nucleosynthesis. On the other hand, these light elements are relatively abundant in CRs, because they are produced in the spallation of parent nuclei, like Oxygen and Carbon, each time they interact with the Interstellar Medium. In the same way Sc, Ti and V are produced in Ni and Fe spallation processes.
Given the relative abundances of these elements in our Galaxy, a confinement time $\tau_{cr} \simeq 3\ \cdot 10^6\, yrs$ is obtained.

1.3.1 Super Nova Remnants

A confinement time of a few million years is very short with respect to the age of the Galaxy, and therefore CRs must continuously be produced in our Galaxy.
The power of the ensemble of CR sources in the Milky Way can be estimated as the ratio between the total energy of CRs in the Galaxy, divided by their average confinement time:

$$L_{\rm cr}^{\text{Milky Way}} \simeq \frac{\rho_{\rm cr}\, V_{\rm eff}}{\langle \tau_{\rm cr} \rangle} \simeq 2 \times 10^{41} \left(\frac{\rm erg}{\rm s}\right) \tag{1.12}$$

where $\rho_{\rm cr} = 1.6\, eV\, cm^{-3}$ is the local CR energy density, V_{eff} is the effective volume of 170 kpc^3 and $< \tau_{cr} >$ is the average confinement time.
On the basis of this luminosity evaluation, Super Novae are the most likely sources to produce galactic CRs. In addition to these energy balance considerations, in the 1970's a dynamical argument emerged in favour of the Super Nova (SN) hypothesis, when it became clear that the spherical *shock waves* produced in the interstellar medium by the (supersonically moving) SN ejecta can provide the environment where charged particles are accelerated up to very high energies, generating a power law spectrum with a well defined slope $\alpha \simeq 2$: that is well compatible with the injection spectrum needed to generate the observed CRs.
The basic concept behind this theory is an extension of the ideas developed by Enrico Fermi, who in 1949 made the hypothesis that the acceleration of CRs is a stochastic process, where each CR particle acquires its high energy in many collisions with moving plasma clouds [97]. The clouds carry (in their own rest frame) turbulent magnetic fields and act as *magnetic mirrors* transferring on average a positive amount of energy to the scattering particles with $\langle \Delta E \rangle / E \propto \beta^2$ (β indicates the cloud velocity). This process generates a power law spectrum, with higher energy particles having performed a larger number of collisions.
The crucial new element introduced in the 1970's is the presence of the *shock wave*. In this updated version of the acceleration model, charged particles are accelerated by the scattering against magnetic irregularities present both upstream and downstream of the shock front that act as Fermi's clouds. The new geometry allows for a more efficient acceleration,$(\langle \Delta E \rangle / E)_{\rm crossing} \propto \beta_{\rm shock}$, and the (mass, momentum and energy conservation) constraints of the fluid properties across the shock determine the slope ($\alpha \simeq 2 + \epsilon$) of the accelerated particle spectrum.
This mechanism (diffusive acceleration in the presence of shock waves) can operate every time a shock wave in an astrophysical fluid is present. The spherical blast waves of SN ejecta are one example of this situation, but several other are known to exist. Shocks are generated every time that macroscopic amounts of matter move at supersonic speed. Particularly interesting case are the jets emitted by Gamma Ray Bursts, by accreting Black Holes of stellar mass (microquasars) or by Active Galactic Nuclei. In all these objects there is in fact evidence for charged particle acceleration.
In the vicinity of young SuperNova Remnant (SNR) one should find a population of relativistic hadrons (protons an nuclei) with a spectrum close to the injection one ($E^{-(2+\epsilon)}$) and a total energy of order $\sim 0.2 \times 10^{51}$ erg. These relativistic particles can interact with the interstellar medium around the SN producing neutral and charged pions that then decay generating photons and neutrinos with a spectrum

that approximately follows the same power law of the parent proton spectrum.
In 2004 the H.E.S.S. experiment observed the SuperNova Remnant RX J1713.7-3946 [21] as a very bright source of TeV photons, as shown in figure 1.5. The property

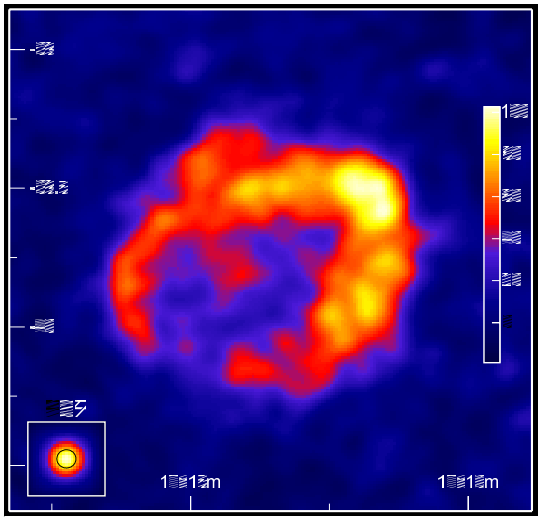

Figure 1.5. Combined H.E.S.S. image of SNR RX J1713.7-3946 in $\gamma - rays$, from 2004 and 2005 H.E.S.S. data [21].

of the photons from this source are consistent [23] with the expectation of the "SNR paradigm" for galactic cosmic rays. Several other young SNR have also been detected by identifying TeV photons: these observation gives support to the possibility that Super Nova Remnants are sites for CRs acceleration. This conclusion is however not unambiguous: also for the best candidate source RX J1713.7-3946 a "leptonic origin" of the radiation (syncrotron radiation and inverse Compton effect of relativistic $e^{\mp}$ on the radiation fields around the SN) cannot be entirely excluded. A recent estimation of neutrino event rates coming from these sources [84] shows that a detection seem possible in a cubic-kilometer scale neutrino telescope placed in the Northern hemisphere.

1.3.2 Microquasars

Microquasars display, on a reduced scale, some of the properties of quasars, including strong emission across a broad range of wavelengths, from radio to X-rays, rapid variability in X-rays, and radio jets. A microquasar consists of a binary system in which a normal star orbits around, and loses matter to, a nearby compact object (either a black hole or a neutron star). The lost matter enters a fast-spinning accretion disk, is heated to millions of degrees, and then either falls onto the compact object or is ejected as a bipolar flow. Several authors proposed microquasar jets as possible sites for the acceleration of charged particles, up to energies of the order of $10^{16}\ eV$: microquasars have also been proposed as sites for high energy neutrino production.
Aharonian *et al.* discussed in [22] different scenarios to describe the recent observation of $\gamma - rays$ from $LS\,5039$ by the H.E.S.S. Collaboration. Both leptonic and hadronic mechanisms were considered to occur: the latter could be invoked as re-

sponsible for the production, together with the observed TeV $\gamma - ray$ flux, of a TeV neutrino flux of the order of $10^{-12}\, cm^{-2}\, s^{-1}$.

1.4 Extra-Galactic Sources of High Energy Neutrinos

1.4.1 Gamma Ray Bursts

In the 60's both American and Soviet Union military satellites reported the observation of short and intense γ-rays from extra-terrestrial directions.
The first systematic studies on Gamma Ray Bursts (GRBs in the following) were performed in the 90's with the launch of the NASA project BATSE (Burst And Transient Source Experiment), on board of the CGRO (Compton Gamma Ray Observatory): the BATSE mission observed more than 2700 bursts, with energies between 20 and 2000 KeV, in its 9 year activity. BATSE observations showed com-

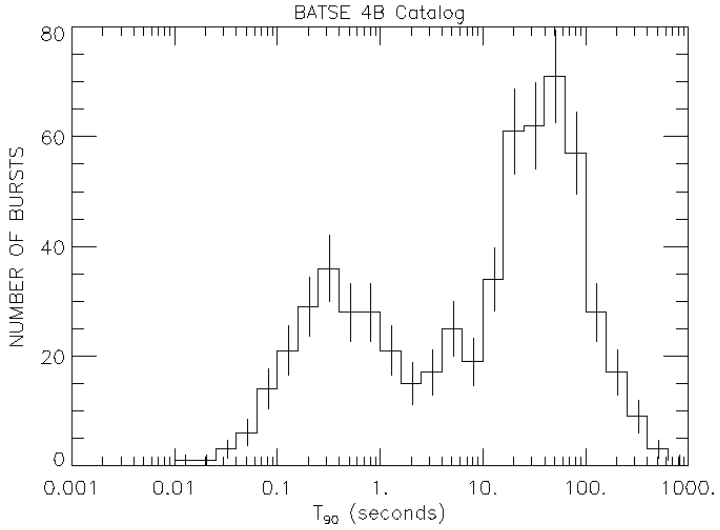

Figure 1.6. Distribution of t_{90} for 1234 GRBs in the BATSE 4B Catalog. t_{90} is defined as the time at which 90% of the signal is detected.

plete isotropy of GRBs in the sky, providing a strong evidence against their galactic origin. No optical follow-up was possible with BATSE, implying no redshift measurements. Beppo-SAX, an Italian project launched in 1997, performed the first redshift measurements: since these redshift were discovered to be cosmological, GRBs were finally known to happen outside our Galaxy.
GRBs are between the brightest sources, their total luminosity under the hypothesis of isotropic emission being around $L_{GRB} \simeq 10^{51}$ erg/s: these source are four orders of magnitude brighter than Active Galactic Nuclei, the most luminous steady sources in the sky , with luminosity $L_{AGN} \simeq 10^{44 \div 47}\, erg/s$. While GRBs emit only for a short time, AGNs are active for long periods, so that the integrated luminosity is comparable, being about $10^{62}\, erg$.
Figure 1.6 shows the distribution of the duration t_{90} of the bursts, the time at which 90% of the signal was recorded. Two populations of bursts can be identified, classified as "short" ($t_{90} < 2$s) and "long" bursts ($t_{90} > 2$s).

The *standard* model for GRBs is the *fireball model* [104], schematically described in figure 1.7. This model does not provide any constraint on the progenitor, but yelds

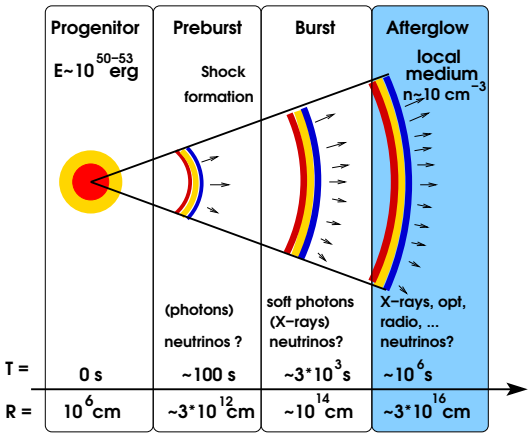

Figure 1.7. Schematic representation of the GRBs fireball model [43].

a phenomenological description of the actual bursts observations.
The basic idea is that a large amount of mass is ejected within a short time window. The plasma is later ejected in shells. At some point, the outer shells slow down and are reached by inner and younger shells, producing a shock wave that accelerates charged particles up to very high energies: while protons can be accelerated loss-free up to very high energies ($E \simeq 10^{21} eV$), electrons loose their energy emitting synchrotron radiation, that escapes from the shock region as soon as it becomes optically thin. This is observed as *prompt emission* from GRBs.
Those shocks resulting from collisions are called *internal shocks*, while *external shocks* result from collisions of the shells with the interstellar medium, leading to *afterglow* emission. While during the prompt emission $\gamma - rays$ of energy $E_\gamma > 100 KeV$ are detected, afterglow emission is observed in almost all wavelengths bands.

Gamma Ray Bursts as neutrino sources

A summary of the photon and neutrino emission mechanisms from GRBs is shown in figure 1.8. Only prompt gamma and neutrino emission will be described.
The prompt GRB photon spectrum N_γ follows a broken power law, as introduced by Band *et al* [38], the two spectral indexes being $\alpha \simeq -1$ and $\beta \simeq -2$. The value of the energy break ϵ_b is usually between 100 KeV and 800 KeV.
The neutrino spectrum can be derived assuming that protons and electron have the same energy spectrum at the source. The neutrino spectrum can be described using the following expression, from [124]:

$$E_\nu^2 \frac{dN}{dE} \simeq \frac{F_\gamma f_\pi}{8 \epsilon ln(10) t_{90}} \begin{cases} (\frac{E_\nu}{\epsilon_{b\nu}})^{-\beta-1} & \text{if } E_\nu < \epsilon_{b\nu} \\ (\frac{E_\nu}{\epsilon_{b\nu}})^{-\alpha-1} & \text{if } \epsilon_{b\nu} < E_\nu < \epsilon_{b\pi} \\ (\frac{E_\nu}{\epsilon_{b\nu}})^{-\alpha-1} (\frac{E_\nu}{\epsilon_{b\pi}})^{-2} & \text{if } E_\nu > \epsilon_{b\pi} \end{cases} \tag{1.13}$$

The normalization factor is given by the product of the gamma-ray fluence (f_γ) with the fraction of proton energy transferred to the pions (f_π) and also the factor

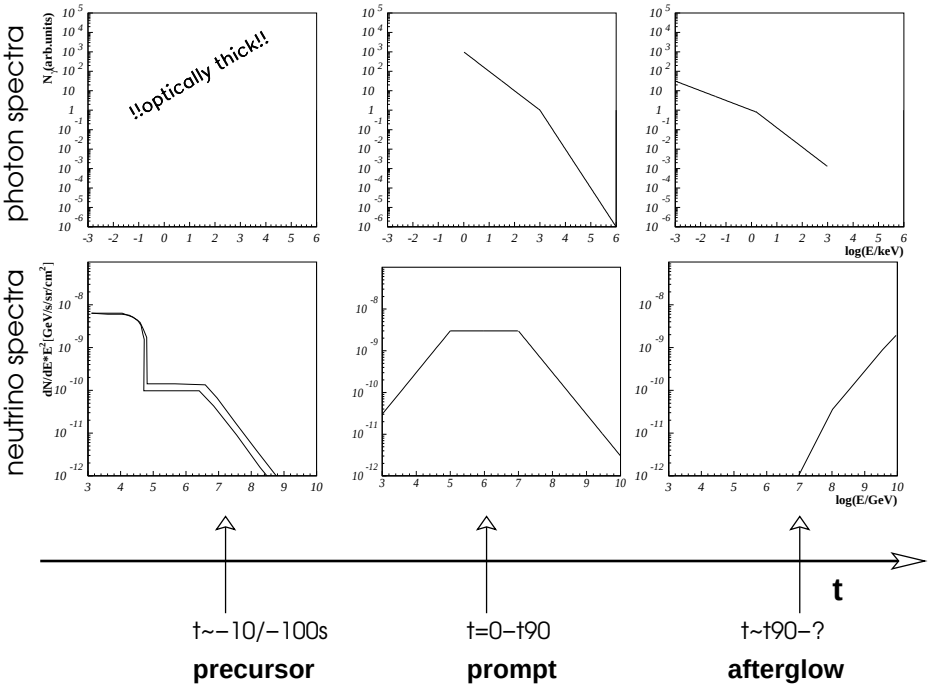

Figure 1.8. Overview of different neutrino production scenarios during the three different phases of a GRBs, together with the corresponding radiation flux [43].

1/8, taking into account that half of the photohadronic interactions result in four neutrinos). The factor $1/\epsilon$ accounts for the fraction of total energy in electrons compared to protons in the jet, while t_{90} represents the time needed to accumulate 90% of the signal.
Given the transient nature of this kind of sources, GRBs are the neutrino emitters that have highest probability to be detected, since the background events which are expected in the narrow time window typical of prompt emission is such that signal-to-noise ratio is optimal.
A statistically significant neutrino signal from a single burst is unlikely to occur in a neutrino telescope with an area smaller than the km^2, like ANTARES, nonetheless a sufficient statistics for a significant detection of neutrino signal from these sources is expected within 4-5 years of data taking [100].

1.4.2 Active Galactic Nuclei

Some galaxies were discovered to have a luminosity much higher than normal over a wide range of the electromagnetic spectrum: $L_\gamma \simeq 10^{44 \div 47}$ erg/s. The radiation from these active galaxies (AGN in the following) is believed to be powered by a rotating supermassive black hole at the centre of the host galaxy.
A schematic picture of the AGN structure is shown in figure 1.9.
The core is active due to the accretion disk which forms around the central black hole and radiates strongly at optical frequencies. The disk is fed by matter from

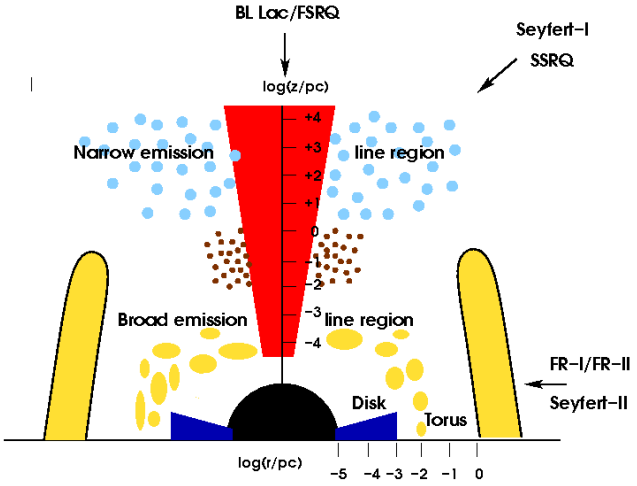

Figure 1.9. Scheme of a cilindrically symmetric AGN shown in the r-z-plane, both axes logaritmically scaled to 1 pc. It is indicated which objects are believed to be seen, and from which direction [43].

a dust torus. Perpendicular to the accretion disk, two relativistic jets are emitted, transporting matter in form of lobes. Knots and hot spots along the jets emit the strong observed radio signal of AGN. It is expected that these knots and hot spots represent shock environments in which particles are accelerated up to ultra high energies, of the order of $E \sim 10^{21}\, eV$.
AGN observed radiation spectrum is mostly in the form of a non-thermal radiation, ranging from very low frequency radio to extremely energetic gamma rays. The non-thermal spectrum consists of synchrotron radiation in the radio to X-ray range, and inverse Compton emission in the X-ray to γ-ray region. A thermal spectrum with a peak in the ultraviolet region, showing faint optical emission lines, is also present in some cases.
The structure of these sources shows some peculiar aspects which are common to all of them: a classification can be done, as a result of observations, as shown in figure 1.10, based on the morphology of the host galaxy, the luminosity and the inclination of the vieweing angle.
AGN are usually divided in *radio-quiet* and *radio-loud* according to the intensity of radio emission with respect to the optical flux.

Active Galactic Nuclei as neutrino sources

A particular class of AGN, *blazars*, have their jet axis aligned close to the line of sight of the observer.
Blazars, like all AGN, are thought to be ultimately powered by material falling onto a supermassive black hole at the center of the host galaxy. Gas, dust and the occasional stars are captured and spiral into this central black hole creating a hot accretion disk which generates enormous amounts of energy. There is also a larger opaque torus extending several parsecs from the central black hole, containing a hot gas with embedded regions of higher density. These “clouds” can absorb and then re-emit energy from regions closer to the black hole. On Earth the clouds are

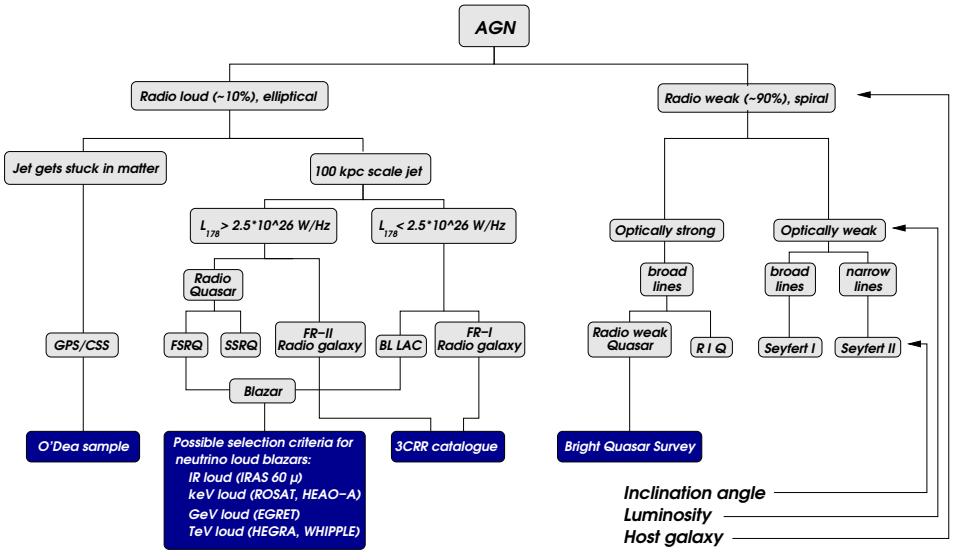

Figure 1.10. AGN classification according to host galaxy, luminosity and inclination angle [9].

detected as emission lines in the blazar spectrum. Perpendicular to the accretion disk, a pair of relativistic jets carry a highly energetic plasma away from the AGN. The jet is collimated by a combination of intense magnetic fields and powerful winds from the accretion disk and torus. Inside the jet, high energy photons and particles interact with each other and the strong magnetic field. These relativistic jets can extend as far as many tens of kiloparsecs from the central black hole.
The observed radiation emission from a blazar is greatly enhanced by relativistic effects in the jet, while the special jet orientation explains the general peculiar characteristics: high observed luminosity, very rapid variation, high polarization (when compared with non-blazar quasars), and the apparent superluminal motions detected along the first few parsecs of the jets in most blazars.
Since blazar jets are in the direction of the observer, they are interesting sources of neutrinos that could be produced in the jets, as schematically described in figure 1.11. Radio galaxies with extended radio jets are also considered as potential neutrino sources.
They were classified in two categories by Faranoff and Riley in 1974. *FR - II* galaxies show high luminosity and have radio lobes at the outer edge of the jet, at distances of the order of kpc from the core. *FR - I* galaxies show lower luminosity power, with radio knots along the jet. The observed non-thermal spectra, mainly arises from electron acceleration. Since jets do not point towars us, thus the expected neutrino flux is weaker than for blazars. Nonetheless neutrino production in the disk is expected to be isotropic compared to the case of jet emission, making neutrino observation feasible, as discussed in [9].

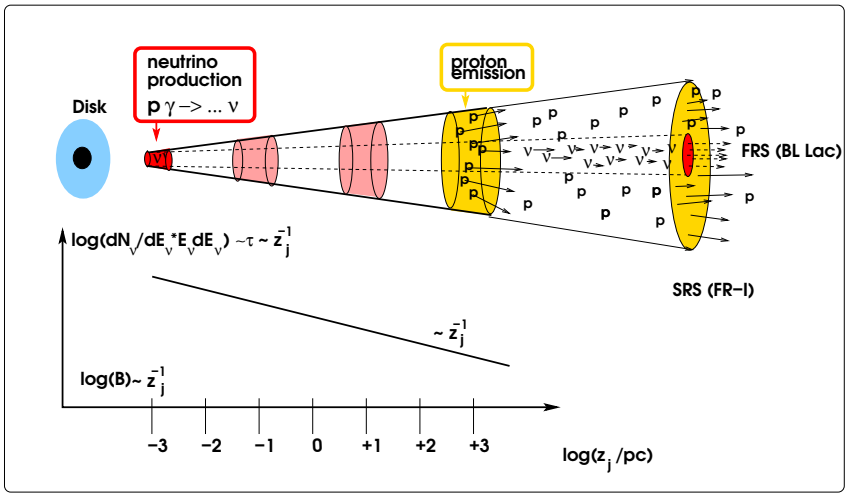

Figure 1.11. Schematic description of the AGN jet. The colored regions represent the emission regions. While neutrino emission happens in early, dense shocks, protons are more likely to come from the last shocks, which are optically thin to proton-photon interactions.

Chapter 2

High energy neutrino detection

2.1 Recent developments in neutrino physics

Neutrino oscillation experiments opened a window to a previously unexplored aspect of particle physics: neutrino masses and lepton flavor mixing [86].
The first hints for the hypothesis of lepton flavor non conservation came from the experimental evidence that atmospheric and solar neutrino fluxes were smaller than expected. However it was not straightforward to conclude that this deficit was due to the neutrino oscillations, as the effect observed could be also ascribed to uncertain theoretical predictions.
Solar neutrinos were first detected in the 1960s with the Homestake [59] radiochemical experiment: the solar ν_e flux was measured to be smaller than the one predicted by the Standard Solar Model [34].
In the following years other experiments observed a deficit in the solar neutrino flux: the conclusive solution to the *solar neutrino problem* came in 2002 with results of SNO[1] [19], [20], that being able to detect neutral current interactions, measured the total number of events due to interactions of neutrinos from the Sun. SNO observed that the missing ν_e were actually converted into neutrinos of other flavors. SNO results were later confirmed by KamLAND[2] [4], a liquid scintillator experiment able to detect reactor $\bar{\nu_e}$ traveling on average $\simeq$ 180 km before reaching the detector.
Evidence for atmospheric neutrino oscillations was first obtained by the Super Kamiokande experiment [69], which observed an asymmetry in the rate of *upward* and *downward* going muon neutrinos. Disappearence of muon neutrinos was later confirmed by neutrino accelerator experiments such as MINOS [99] and K2K [25]. Accelerator experiments measured the ν_μ flux both in the vicinity of the production point, where no oscillation was expected, and far away from the source. Besides observing a deficit in the number of muon neutrinos in the *far detector*, with respect to what expected from the *near detector* measurements, these experiments found a distortion in the energy spectrum of surviving muon neutrinos, which was consistent with the oscillation hypothesis.
The probability to detect at a generic time t a neutrino of flavor f', after that a

[1] Solar Neutrino Observatory
[2] KAMioka Liquid scintillator Anti-Neutrino Detector

state with flavor f has been produced at t=0 is given by:

$$P(\nu_f \rightarrow \nu_{f'} : t) = sin^2 2\theta sin^2(\frac{\Delta m^2 L}{4E}) \tag{2.1}$$

with θ the mixing angle between the flavor f and f', Δm^2 the square of the mass difference between the two eigenstates, E the energy and L is the distance from the source at which the neutrino is detected.
Considering the three neutrino flavors, the flavor oscillations mechanism is characterised by three angles, two mass splittings and one phase. Two additional phases have to be included in the computation, if the neutrino is considered a Majorana particle, i.e. it is coincident with its antiparticle. Up to now, having been able to measure the neutrino mass-squared differences and two of the three mixing angles, oscillation experiments have greatly improved our understanding of neutrino physics [67].
Table 2.1 reports current values for neutrino oscillations parameters extracted from a global fit on most recent experimental data: two mass splittings, as well as two out of three mixing angles have been measured with reasonable precision, while the mixing angle θ_{13} is constrained by an upper limit.
Some parameters remains to be identified: the value of mixing angle θ_{13}, indicating

Table 2.1. Neutrino oscillation parameters from global fit on most recent experimental data [113]. The value of the solar mass splitting Δm^2_{21} has been determined together with its sign, while the sign of the atmospheric mass splitting is not yet known.

Parameter	Central Value	3σ
$\Delta m^2_{21}[10^{-5}eV^2]$	$7.65^{+0.23}_{-0.20}$	$7.05 \div 8.34$
$\Delta m^2_{23}[10^{-3}eV^2]$	$2.40^{+0.12}_{-0.11}$	$2.07 \div 2.75$
$sin^2\theta_{12}$	$0.304^{+0.022}_{-0.016}$	$0.25 \div 0.37$
$sin^2\theta_{23}$	$0.50^{+0.07}_{-0.06}$	$0.36 \div 0.67$
θ_{13}	$0.01^{+0.016}_{-0.011}$	≤ 0.056

the ν_e component in ν_3, the phase δ, whose value could indicate the violation of CP-invariance in the lepton sector, the mass splitting Δm^2_{31} and the sign of the atmospheric mass splitting Δm^2_{23}.
One of the most striking consequences of the neutrino oscillation phenomena is that neutrinos are massive particles: a number of questions about neutrinos masses have still to be answered, concerning absolute neutrino masse scale, mass hierarchy and nature of neutrino masses.

Neutrino mass hierarchy

Neutrino oscillation data is compatible with three types of neutrino mass spectra, depending on the unknown values of the mass of the lightest neutrino and the sign of the atmospheric mass splitting Δm^2_{23} (see figure 2.1):

- If $\Delta m^2_{23} > 0$, neutrino mass eigenstates are arranged according to the so called *normal mass hierarchy* and the following relation holds: $m_1 < m_2 < m_3$.

- If instead $\Delta m^2_{23} < 0$, mass eigenstates are arranged according to the *inverted mass hierarchy*. In this case the lightest neutrino is ν_3, and the two other mass eigenstates are almost equal: $m_3 < m_1 \simeq m_2$.
- There is also the possibility that the absolute value of the smaller neutrino mass is much bigger than the big atmospheric mass splitting. In this case, no matter whether the normal or inverted hierarchy holds, all the three neutrino mass eigenstates are almost degenerate.

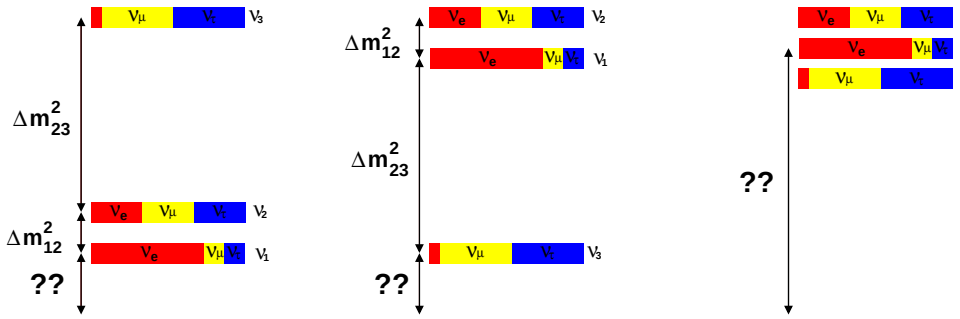

Figure 2.1. Pictorial representation of the three mass hierarchy schemes that are compatible with current experimental data. The left picture represents the so-called normal hierarchy. The central picture represents the so called inverted hierarchy, while the right picture represents the degenerate case, where the three neutrino masses are almost equal, and are much bigger than the solar and atmospheric mass splittings. The three colors on each neutrino mass eigenstate represent the respective projection on the three flavor eigenstates.

Absolute measurement of neutrino mass

Limits on absolute neutrino masses come from cosmological constraints and from non-oscillation experiments, based on the study of single and double beta decay. Direct neutrino mass measurements are based on the analysis of the kinematics of charged particles emitted together with neutrinos in various weak decays. The most sensitive measurements, involving electron neutrinos, are based on the study of the shape of the β spectrum end-point. Current best limits come from tritium β-decay experiments [102]: $m_\beta \leq 2.1$ eV. Cosmological constraints on neutrino masses come from the observation of the Cosmic Microwave Background anisotropies and from the study of large scale structures [67].

Dirac and Majorana neutrinos

Oscillation experiments and direct search for neutrino mass are not affected by the nature of the neutrino. The physics involved in these kind of measurements is the same, regardless of whether neutrinos are Dirac or Majorana particles.
Under the action of the $\mathcal{C}$ operator, a left-handed field goes into a right-handed one, and viceversa. As a consequence of the fact that neutrino has no electric charge, it is possible that the right handed component of the neutrino field is simply the $\mathcal{C}$ - conjugated of the left handed field. If this possibility is verified, neutrino is a

Majorana particle. In contrast with the Dirac case, where the two components of the field are completely independent, for a Majorana field they are related to each other by particle-antiparticle conjugation:

$$\begin{aligned} Dirac: &\qquad \psi_D = \psi_L + \psi_R \\ Majorana: &\qquad \psi_M = \psi_L + (\psi_L)^c \end{aligned} \tag{2.2}$$

Particles described by a Majorana field are purely neutral, i.e. they coincide with their own anti-particles. It is then clear that the possibility of describing a fermion by a Majorana field only arises for neutrinos, as other fermions have electric charge. The most promising approach to discriminate between these two possibilities is to search for neutrinoless double beta decay ($\beta\beta 0\nu$). If accompanied by the emission of two neutrinos, double beta decay is a second order process allowed in the Standard Model ($\beta\beta 2\nu$): this decay conserves lepton number, cannot discriminate between Dirac and Majorana neutrinos and does not depend significantly on neutrino masses. There is also the possibility for double beta decay to occur without emission of neutrinos. This decay mode is forbidden in the Standard Model, as it violates the lepton number by two units. Apart for a controversial claim [39], neutrinoless double beta decay has never been observed: only experimental lower limits have been set for some commonly studied isotopes.

2.2 High energy neutrino detection methods

When a neutrino $\nu_l = \nu_e, \nu_\mu, \nu_\tau$ interacts with a nucleon N via charged current interaction, a lepton $l = e, \mu, \tau$ is produced:

$$N + \nu_l \rightarrow X + l \tag{2.3}$$

where X indicates the hadronic product of the interaction, leading, eventually, to a hadronic cascade. Indirect detection of high energy neutrinos is thus possible via the identification of the outcoming charged leptons. Charged particles, propagating with velocity $\beta c > c/n$ in a transparent medium, e.g. water or ice, with refractive index n, polarize the medium inducing the emission of coherent Čerenkov[3] radiation along the surface of a cone, whose axis is coincident with the particle direction. The wave front propagates along a direction which forms a fixed angle, indicated as θ_C, with the direction of the charged lepton. The value of this angle depends on charged particle velocity β and on the environmental properties:

$$cos\theta_C = \frac{1}{n\beta} \tag{2.4}$$

The radiation per unit length x and wavelength λ is given by the Franck-Tamm formula [92]:

$$\frac{d^2N}{dxd\lambda} = \frac{2\pi\alpha z^2}{\lambda^2}(1 - \frac{1}{n^2\beta^2}) \tag{2.5}$$

[3]Nobel Prize in Physics in 1958, together with I. M. Franck and I. Y. Tamm, "for the discovery and the interpretation of the Čerenkov effect"

where z is the charge of the particle which propagates at superluminal velocity in the medium, and $\alpha = \frac{1}{137}$ is the fine structure constant.
Optical frequencies are the most interesting concerning the detection of cosmic neutrinos of energies between 100 GeV and 10 PeV. At wavelengths in the range $\lambda \sim 300 \div 700$ nm, corresponding to a large transmission length in a natural media like water or ice, the number of radiated photons per unit distance x is given by:

$$\frac{dN}{dx} \sim 200\, cm^{-1} \tag{2.6}$$

Emitted radiation decreases as a function of the wavelength:

$$\frac{dN}{dx} \propto \lambda^{-2} \tag{2.7}$$

Due to low fluxes expected, as described in the previous chapter, cubic kilometer-scale neutrino telescopes are required to detect neutrinos of all flavors. The realization of a high energy neutrino telescope thus requires a large amount of a transparent medium, together with a *shield* to reduce the background of atmospheric muons, produced in the interactions of cosmic rays with air molecules. Deep sea water or deep ice are very suitable solutions to the location of such a large detectors, giving the opportunity to exploit the good light transmission properties of these natural radiators.
The maximum detection efficiency is possible at frequencies corresponding to blue visible light ($\lambda \simeq 440$ nm), where the absorption of light in sea water and ice in minimised. This wavelength also corrensponds to the value wich maximises the quantum efficiency of a photomultiplier tube (PMT).
A detector for high energy neutrinos with energies between 10 GeV and 10 PeV is thus basically a three-dimensional array of PMTs, where large volumes of water or ice are used as natural radiators for the propagation of Čerenkov light.
The probability to detect neutrinos raises as a function of the neutrino energy, since the cross section of neutrino-nucleon interactions increases with energy, as shown in figure 2.2.
Neutrino telescopes detect the secondary particle showers initiated by neutrinos of all flavors as well as the leading secondary muon tracks initiated by ν_μ only: a sketch of the signatures of the event topologies occurring for different neutrino flavours and different kinds of interactions is shown in figure 2.3, while a brief overview of peculiar detection aspects for the three neutrino flavors will be given in the following.

Muon Neutrinos

Secondary muons initiated by muon neutrinos interacting via charged current, propagate over kilometers at PeV energy, up to tens of kilometers at EeV energy, generating showers along their track by bremsstrahlung, pair production at TeV energy and photonuclear interactions. The typical signature of a high energy muon propagating through the detector is a light cone, whose axis is coincident with the muon direction, as in figure 2.5. High energy muons loose energy catastrophically according to:

$$\frac{dE}{dx} = -\alpha - \beta E\,, \tag{2.8}$$

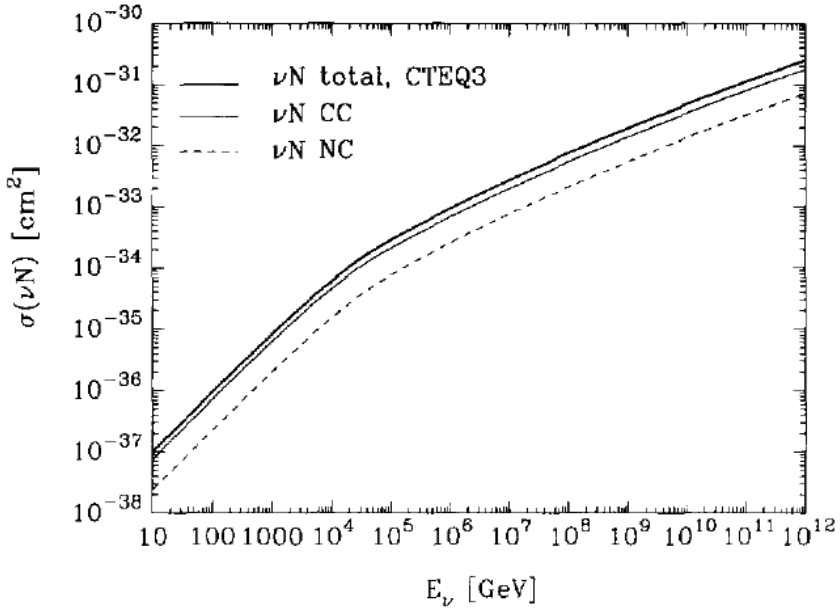

Figure 2.2. Neutrino cross section as a function of neutrino energy [71].

$\alpha = 2.0\times10^{-6}$ TeV cm^2/g, accounts for ionisation processes and $\beta = 4.2\times10^{-6}$ cm^2/g, accounts for radiative losses [96].
If we assume that a muon of initial energy E_μ, traversing each layer Δx of a certain medium, always looses the expected average amount of energy, we can compute the muon *range*, i.e. the distance a muon travels before its energy drops below some energy threshold, $E_\mu^{\rm thr}$, obtaining:

$$R = \frac{1}{\beta} ln(1 + \frac{E_\mu}{\epsilon}) \tag{2.9}$$

where $\epsilon = \frac{\alpha}{\beta}$ is defined as the muon critical energy at which the ionisation loss equals the radiation loss. The distribution of the muon range in rock and water for different muon energies, expressed in water equivalent km, is shown in figure 2.4. This is a good expression for the muon range up to energies $E_\mu < \epsilon$. At higher energies the energy loss due to radiation emission starts to dominate.
To be identified, a ν_μ must interact via charged current and produce a muon with sufficient range to reach the detector. The detection probability is the product of the interaction probability and the range of the muon:

$$P_{\nu\to\mu} \simeq n\sigma_\nu R \tag{2.10}$$

where n is the number density of target nucleons, σ_ν is the charged current interactions cross section and R is the muon range.

Electron Neutrinos

High energy electron neutrinos deposit 0.5-0.8% of their energy into an electromagnetic shower, initiated by the electron produced in the final state of the charged

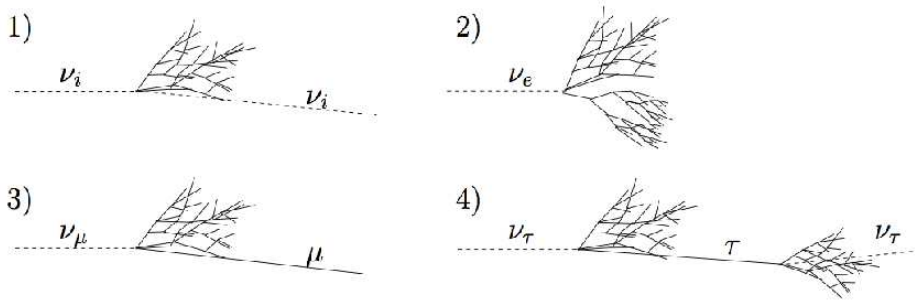

Figure 2.3. Signatures of the event topologies occurring for different types of neutrino interactions. 1) Neutral current interaction producing only a hadronic shower. 2) Charged current (CC) interaction of a ν_e initiating an electromagnetic shower. 3) Charged current interaction of a ν_μ producing a long range muon. 4) Charged current interaction of a ν_τ producing a τ that decays after some distance.

current interactions with nucleons of the medium surrounding the detector. The rest of the energy goes into the fragments of the target, that produce a second subdominant shower. The signature of electrons propagating through a neutrino telescope is that of a moving *sphere-like* surface, whose radius increases with the shower energy (figure 2.5). Because the shower and its accompanying Čerenkov light are not totally symmetric, but elongated in the direction of the electron (and incident neutrino), its direction can be reconstructed. Pointing accuracy is however poorer than what can be achieved with muon neutrinos and estimated around $\simeq 10^\circ$ only.
On the other hand, if compared to ν_μ, the energy reconstruction for ν_e induced charged current events is more accurate and the background of atmospheric neutrinos is significantly reduced, since at higher energies atmospheric muons decay is less probable, reducing the content of high energy ν_e.

Tau Neutrinos

We believe that the relevant component of neutrino fluxes in astrophysical sources is due to ν_μ and ν_e, mainly coming from pion photoproduction and following decays. Only a faint flux of ν_τ could be expected due to production, and decay, of charmed mesons. In the absence of oscillations, ν_τ of astrophysical origin would be a small part of the total neutrino flux, as seen in section 1.2: after traveling over cosmological distances, approximately 1 out of 3 neutrinos arriving at Earth is of τ flavor.
In a kilometer-scale neutrino detector, tau neutrinos can be identified at PeV energies. *Double bang* events occur when a τ lepton is produced along with a hadronic shower in a charged current interaction within the detector volume, and the τ decays producing electromagnetic and hadronic showers before exiting in the detector. Below a few PeV, the Lorentz factor γ is such that the τ lepton travels a short distance before decaying. A short path from the production to the decay point implies that the two showers cannot be distinguished.
Lollypop events occur when only the second shower produced in the *double bang*

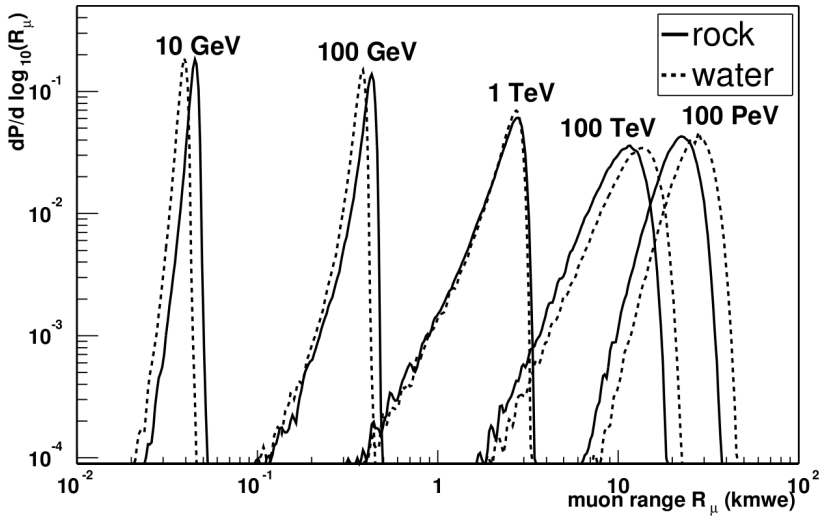

Figure 2.4. Distribution of the muon range in rock and water for different muon energies, expressed in water equivalent km.

develops within the detector volume, and a τ lepton track is identified entering the shower over several hundreds meters. Below several PeV energies, τ tracks are not long enough to be identified.
An important aspect on ν_τ is that they are not depleted in number by the absorption in the Earth: τ neutrinos which interact producing a τ lepton generate another τ neutrino when the tau lepton decays, thus only degrading the energy of the neutrino.

2.3 High energy neutrino telescopes

In the following sections a review of past, current and future high energy neutrino experiments will be given, describing different detection techniques. Figure 2.6 describes the most suitable techniques for neutrino detection, for different neutrino energy scales.

2.3.1 Čerenkov high energy neutrino detectors

The project who pioneered the field of high energy neutrino Čerenkov telescopes was DUMAND[4] [91], whose main goal was the realization of an underwater neutrino observatory in the Pacific Ocean. Successful deployment of the basic infrastructure, including the shore cable, the underwater junction box, and an environmental module was accomplished in 1993. One optical module string was also deployed and operated for a brief period of time. Feasibility studies towards acoustic neutrino detection were also performed. The DUMAND project was stopped in 1995, before the construction of the detector was initiated.

[4]Deep Underwater Muon and Neutrino Detector

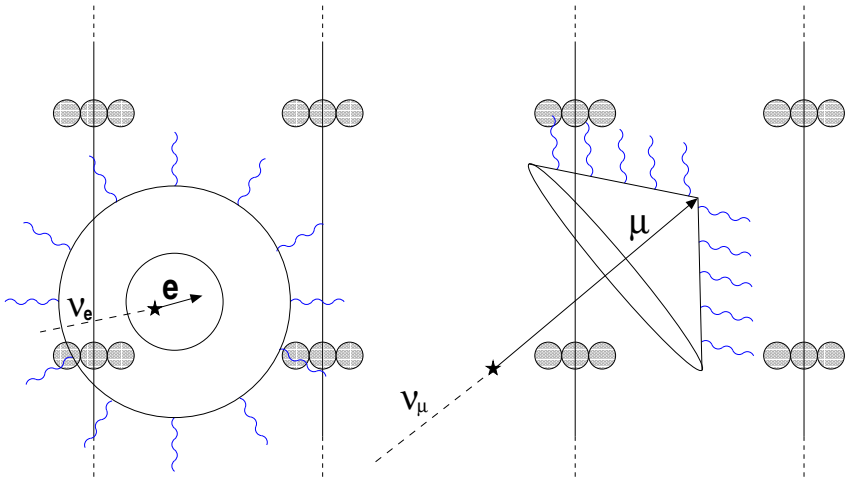

Figure 2.5. Čerenkov light pattern produced by muons (right) and by secondary showers initiated by electron neutrinos (left).

After the first pioneering phase, a second phase of prototype construction, anticipating the realization of cubic-kilometer detectors started with the realization of two detectors in both the emispheres: NT36 in the Lake Baikal and AMANDA[5] at the South Pole (figure 2.8).
The Baikal Collaboration [126] was the first which completed the realization of an underwater neutrino telescope, in the Lake Baikal, Siberia: its first stage telescope NT36 (made of 36 photomultiplier tubes) was completed in 1993, while the NT200 (made of 200 photomultiplier tubes) has been operating since 1998 and has been upgraded to the 10 Mton detector NT200+ in 2005. A schematic description of the most up to date detector is given in figure 2.7.
The AMANDA[61] Collaboration has been the first to use ice instead of water as natural radiator, for the realization of a neutrino telescope, located 1 mile deep-ice at the South Pole. In AMANDA, holes have been drilled in ice, and PMTs have been deployed inside. The detector has been operated for more than 5 years in its final configuration of 680 optical modules on 19 strings.
IceCube [60] will complement its predecessor AMANDA, not only increasing the instrumented volume, but also developing auxiliary detectors, like the IceTop air shower array experiment, and using radio and acoustic techniques as well.
Neutrino telescopes located at the South Pole do not cover the Southern sky, which is obscured by the large flux of cosmic ray muons, as can be seen in figure 2.9, showing the region of the sky which is visible to a neutrino telescope in both the Northern and Southern emispheres.
This aspect provides compelling arguments for the realization of cubic-kilometer scale detectors in the Northern emisphere. Extensive efforts have been devoted by three European Collaborations to the realization of a deep underwater cosmic neutrino detector in the Mediterranean sea.
The NESTOR Collaboration was the first to start developing technologies and infrastructures for the marine environment [13].

[5] Antarctic Muon And Neutrino Detector Array

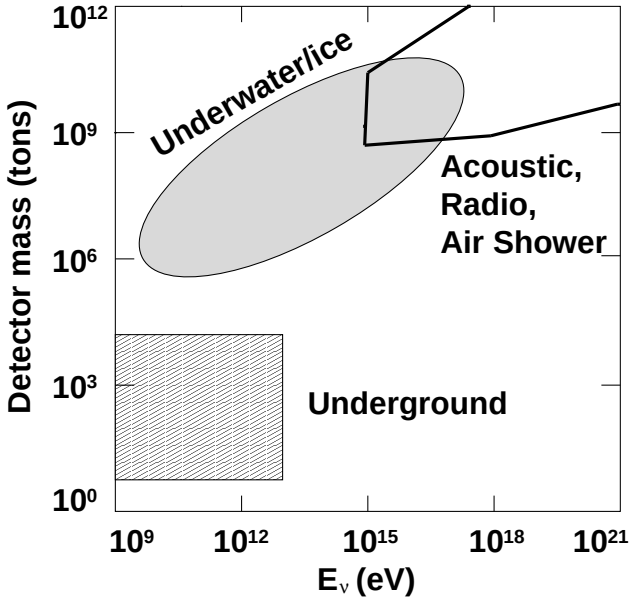

Figure 2.6. Domains of different high energy neutrino detection techniques [116].

The NEMO[6] Collaboration[55] has developed *ad-hoc* technological solutions for the design and realization of both a dedicated mechanics and electronics, in the view of a cubic-kilometer scale experiment. The NEMO *Phase-I* lead to the deployment of a prototype structure in a test-site at 2000 m depth, offshore Catania, Italy. The prototype had a dedicated mechanic setup, PMTs being located on a aluminium *tower*, together with electronics and data acquisition system [29].
The ANTARES[7] Collaboration [57] has designed and built an underwater neutrino telescope covering an area of about 0.1 km^2 on the sea bed, at 2475 m depth, 40 km off the coast of Toulon, France. The detector is an array of PMTs arranged on 12 lines, each comprising up to 25 triplets of PMTs (floors), regularly distributed on 350 m, the first floor being located at 100 m above the sea bed. The detector was completed in May 2008 and it has been working continuously in its 12-lines configuration for almost one year. Detailed description of the ANTARES detector will be given the next chapter.
The ANTARES, NEMO and NESTOR Collaborations have joined their efforts towards the realization of a cubic-kilometer scale underwater detector in the Northern emisphere, in the framework of the KM3NeT Consortium [85], joining advancements in research and development to complement IceCube observations and get a full-view of the sky.

[6] NEutrino Mediterranean Observatory
[7] Astronomy with a Neutrino Telescope and Abyss environmental RESearch

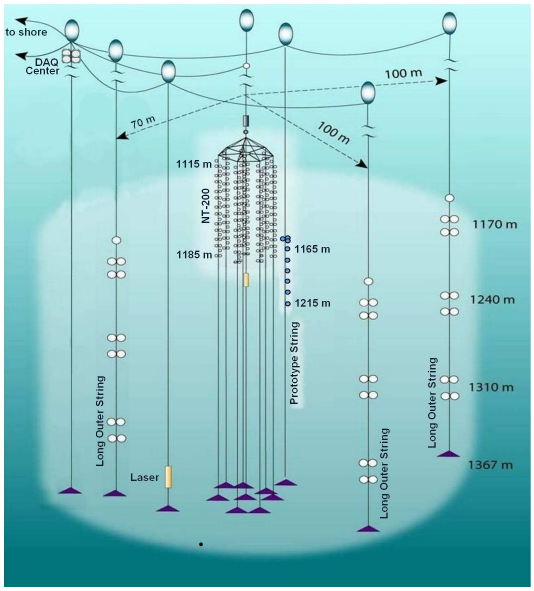

Figure 2.7. The Baikal neutrino telescope as in 2008: the compact NT200 is visible in the center, together with 3 long outer strings and the new technology km3-prototype string [126].

2.3.2 Radio detection technique

A steepening in the CRs spectrum at energies higher than 10^{19}eV was predicted in the 1960s, as a consequence of the interaction of ultra high energy protons with the Cosmic Microwave Background radiation, and observed by both HiRes and Auger experiments, as seen in section 1.2. As a consequence of these interactions, ultra high energy neutrinos from pion decay should be produced, and their clear detection would provide a crucial input to the field.
The expected fluxes are so low at these energies that a cubic-kilometer scale detector would not be enough to collect a sufficient number of events, requiring detectors of unprecedented size: the optical Čerenkov technique is not adequate for such an extension, because the deployment of mechanical structures with PMTs over a volume larger than a cubic-kilometer would imply not affordable costs.
Distances between photomultiplier tubes are fixed by the environmental properties, and in particular by the light transmission in the medium. Since typical values of absorption length are of the order of $50 \div 70$ m in deep sea water and 100 m in deep ice, a larger PMTs spacing would cause a loss of Čerenkov signal detection and a poor quality in the reconstruction of the neutrino arrival direction.
The propagation of radio and acoustic signals in ice, sand or salt, has the fundamental property of a larger attenuation length than for optical signals, of the order of several hundreds of meters. Radio or acoustic detectors could thus be sparser than optical ones, keeping high detection efficiency, covering a much larger area with nearly the same number of sensors, implying an important reduction of costs and resources.
The implementation of radio and acoustic solutions for high energy neutrino detection represents the next-to-next generation of telescopes. Several R&D projects

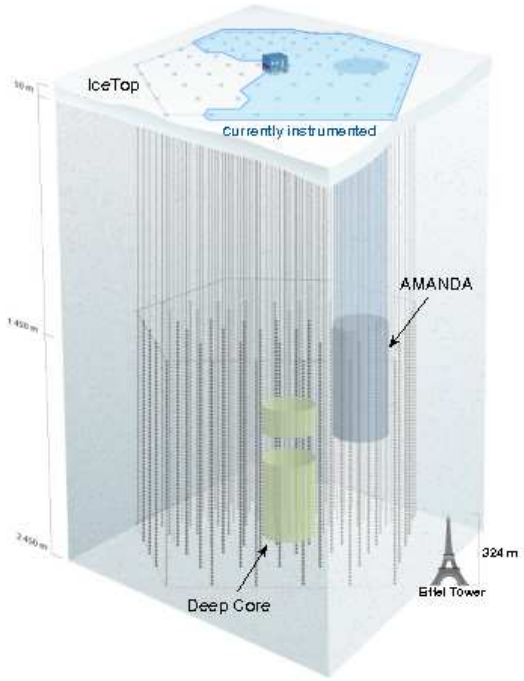

Figure 2.8. Artistic view of the IceCube detector. The IceTop apparatus is shaded blue, and the volumes occupied by the AMANDA and Deep Core subarrays are indicated. The Eiffel Tower is shown for scale [60].

and feasibility studies are currently under way and will be briefly described in the following.

The Čerenkov effect does not only produce radiation of optical and UV frequencies, but has a component in the radio band, as it apperas in formula 2.7.
Radio detection technique can be applied to ultra high energy neutrinos, since the emitted radiation can reveal electromagnetic showers produced in charged current neutrino interactions, as in equation 2.3. This technique is particularly suitable for the detection of ultra high energy particles ($E > 10^{16}$eV). Radio signal induced by the Čerenkov effect has been observed for cascade-like events in sand [111], salt and in ice. While radio signals due to cacades are likely to be detected, the corresponding signal induced by muons is too faint.
The RICE[8] [89] experiment aims at the detection of the radio signal from neutrino-induced cascades at energies of $(10^{15} \div 10^{18})$eV in the ice at the South Pole (figure 2.10).
A geometric volume of 0.008 Km^3 has been instrumented with dipole receivers at a depth of between 100 and 300 m below the surface. At these energies the background due to atmospheric neutrinos and muons can be neglected.
The ANITA[9] [41] ballon-borne experiment is sensitive to neutrino induced cascades of energies between 10^{18} and 10^{23}eV. The experiment aims at the detection, from

[8] Radio Ice Čerenkov Experiment
[9] ANtarctic Impulsive Transient Antenna Experiment

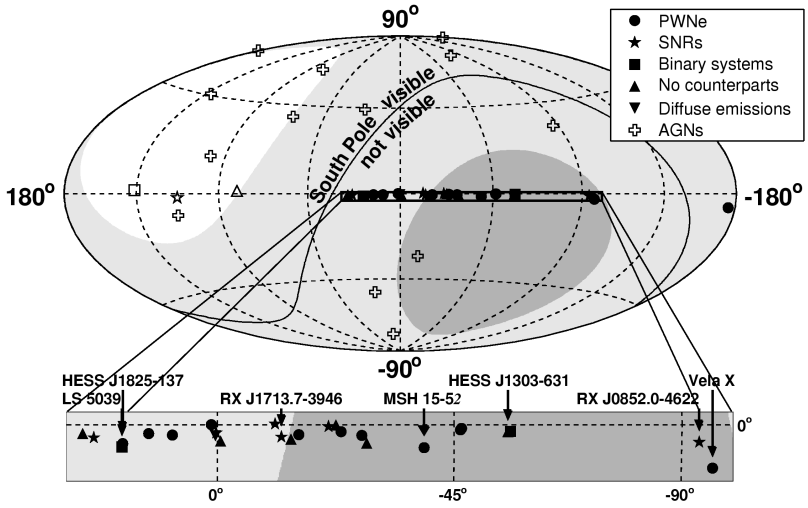

Figure 2.9. Sky map of TeV γ-ray sources in Galactic coordinates together with their visibility to neutrino telescopes [84]. Source types are represented by different symbols, the shaded regions represent $25-75\%$ (*light gray*) and $> 75\%$ (*dark gray*) visibility to a detector in the Mediterranean Sea for energies below ~ 100TeV. The solid curve shows the extent of the visibility of a South Pole detector (IceCube).

the atmosphere, of the radio emission arising from neutrino interactions with nucleons in the Antarctic ice sheet. First results come from test-flights of ANITA-lite. The first full flight was successfully performed in December 2006, the analysis of collected data allowed to set an upper limit to the flux of ultra high energy astrophysical neutrinos, as in figure 2.12. The FORTE[10] satellite observed Greenland ice for about 2 years, searching for Čerenkov coherent emission from electromagnetic showers.
A different method of detecting neutrino-induced radio emission is to serch for radio signals from the Moon regolith, that is the layer of sand an dust which covers the Moon surface, with radio telescopes. The Moon yelds a good target for neutrino interaction and therefore, an enhanced radio signal is expected from the direction of the moon.
The GLUE[11] [73] experiment performed observations with two radio antennas, searching for radio signal from the moon.
A detailed description of both theoretical and experimental aspects of radio detection of cosmic neutrinos can be found in [64].

2.3.3 Acoustic detection technique

Detectable acoustic signals are expected to be produced by neutrino-induced cascades propagating in a medium. The energy cascade deposition occurs instantaneously, so that an immediate heating of the medium is produced. This sudden increase in temperature produces a pressure wave, which has a typical bipolar shape

[10] Fast on-Orbit Recording of Transient Events
[11] Goldstone Lunar Ultra-high energy neutrino Experiment

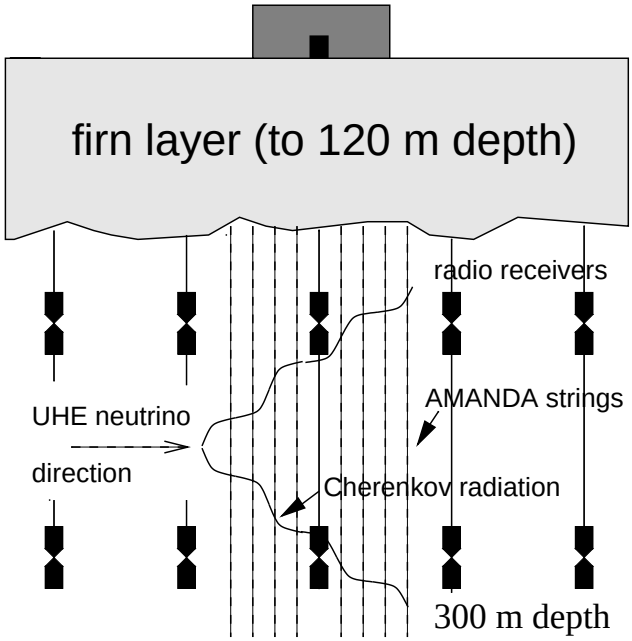

Figure 2.10. Schematic view of the RICE detector at the South Pole [116].

as a function of time (figure 2.11), detectable by means of hydrophones. While cascades are compact and deposit high energy densities, single muons release too low energy density to induce a detectable acoustic pulse.

The SAUND[12] [121] experiment pioneered the field, using for the first time arrays

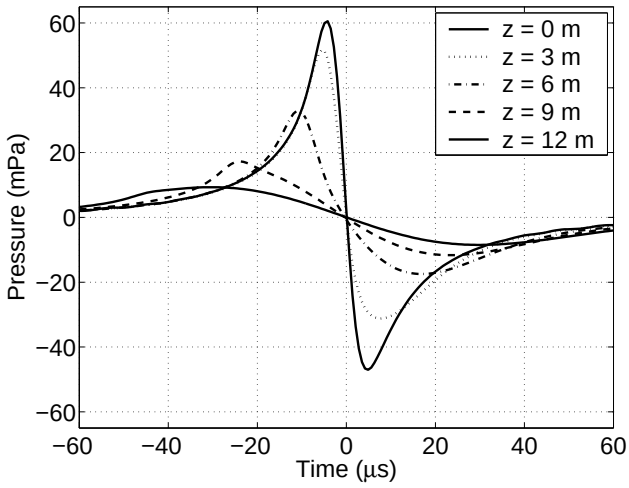

Figure 2.11. Simulated acoustic pulse due to a hadronic shower of energy 10^{20}eV [121].

of hydrophones for acoustic neutrino detection, exploiting an already existing military array in the Bahamas, at a depht of about 1600 m, spread over a surface of about 250 km^2.

[12]Study of Acoustic Ultra-high energy Neutrino Detection

Upper limits to UHE diffuse neutrino fluxes set by several experiments are shown in figure 2.12.

2.3.4 The Pierre Auger Observatory as a neutrino telescope

The Pierre Auger Cosmic Rays Observatory [46] has been designed and realized for the identification of CRs of energies higher than $\simeq 10^{18}$eV.
The detection principle relies on the observation of the extensive air showers which develop in the atmosphere, as a consequence of the interaction of primary CRs with the air molecules. These interactions produce secondary particles which are often unstable, their interactions and decays producing electromagnetic and hadronic showers which propagate from the top of the atmosphere down to the ground level. The size of the shower increases with energy, inducing an increase of the detection efficiency that partly compensates the energy flux dependence. The expected flux of primary CRs is of the order of one particle per km^2 per century, at the energies interesting for the experiment: for these reasons the experiment aims at the detection of extensive air showers with an hybrid array, covering an area of about 3.000 square kilometers, equipped with fluorescence detectors and PMTs.
Fluorescence detectors are used to identify the light emitted as a consequence of relaxation of nitrogen molecules in the atmosphere, which had been excited as the UHE primary CRs hit the atmosphere. The total amount of light depends on the number of particles in the shower and, in turn, on the primary energy, while the shape and direction of the light trace is used to determine the arrival direction of the primary particle. The detection of fluorescence light is affected by a low duty-cicle, since observations with this technique can only be performed in clear and moonless nights.
The surface array detector, composed of tanks filled with water and equipped with PMTs, has a much higher duty-cycle: the combination of the informations obtained with the two techniques is very powerful, and it also reduces the dependence on simulation codes which can be affected by large systematic errors at these extremely high energies.
The detector can measure the energy of the particles: since for E $> 10^{18}$eV charged particles are not deflected by magnetic fields in the way from the source to Earth, CRs arrival direction can be identified from the time and position of the hit detectors.
Charged CRs are not the only particles which can induce showers in the Earth's atmosphere, as we have seen in section 2.2: tau neutrinos interact via charged current producing tau leptons together with cascades. Tau neutrinos induced events can be identified in Auger, detecting the showers produced by horizontal tau leptons. Earth-skimming ν_τ may interact in the Earth's crust and produce a τ lepton in the final state of charged-current interactions. The τ lepton could emerge from the Earth and decay in flight in the atmosphere, often producing a nearly horizontal shower. Typical signature of τ induced showers is the electromagnetic component, which is persistent even at very large atmospheric depths.
No neutrino candidates have been found since the beginning of data taking, in 2004: a limit to the diffuse flux of UHE ν_τ has been set and is shown in figure 2.12, together with theoretical predictions and limits from other experiments.

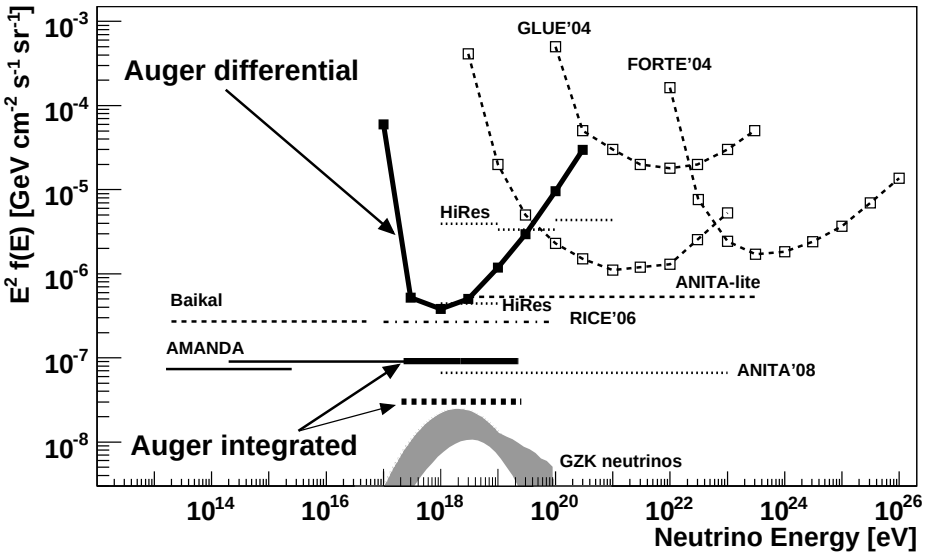

Figure 2.12. Diffuse neutrino flux upper limits, at 90% C.L., from several experiments, together with theoretical predictions. The Auger limits are given using the most pessimistic case of the systematics (solid lines). For the integrated format, the limit that would be obtained in the most optimistic scenario of systematics is also shown (dashed line). The shaded area corresponds to the allowed region of expected GZK neutrino fluxes computed under different assumptions [8].

Chapter 3

The ANTARES high energy neutrino telescope

3.1 Detector layout and site dependent properties

The ANTARES[1] detector is currently the largest deep sea neutrino telescope operating in the Northern hemisphere. The telescope covers an area of about 0.1 km^2 on the sea bed, at 2475 m depth, 40 km off the coast of Toulon, France.
An acoustic positioning system, a time calibration system and a set of devices for the monitoring of site environmental properties are integrated in the detector for complementary measurements. The apparatus also hosts AMADEUS [90], a test set-up devoted to feasibility studies of acoustic neutrino detection.
The ANTARES detector is conceived as a three-dimensional array of photomultiplier tubes, hosted in pressure resistant glass spheres, called *optical modules* (OMs). In its full configuration, the detector is composed of 12 detection lines, each comprising up to 25 triplets of PMTs (storeys), regularly distributed along 350 m, the first storey being located 100 m above the sea bed.
One instrumentation line is also present, with complementary devices installed.
Each line is connected to a junction box on the sea bed, to be electrically fed and to provide a continuous stream of data to shore. The junction box is connected to the shore station by a 40 km long electro-optical cable.
A pictorial description of the apparatus is given in figure 3.1.
The first detection line was installed and connected in early 2006; the second line was put in operation in September 2006; three more lines were connected by the end of 2007; 5 additional lines, together with the instrumentation line, were connected by the end of 2007 and the last two lines were connected in May 2008.
The site which has been selected for the deployment of the ANTARES detector is located off-shore Toulon, France (figure 3.3), at a latitude of 42°50′ N, and a longitude of 6°10′ E: this location ensures a large sky coverage, as shown in picture 2.9.
The key elements which constitute the ANTARES detector are the following:

- **Optical Modules**: the basic detection unit includes the PMT (Hamamatsu 10 inches-photomultiplier tube), hosted in a pressure-resistant glass sphere,

[1] Astronomy with a Neutrino Telescope and Abyss environmental RESearch

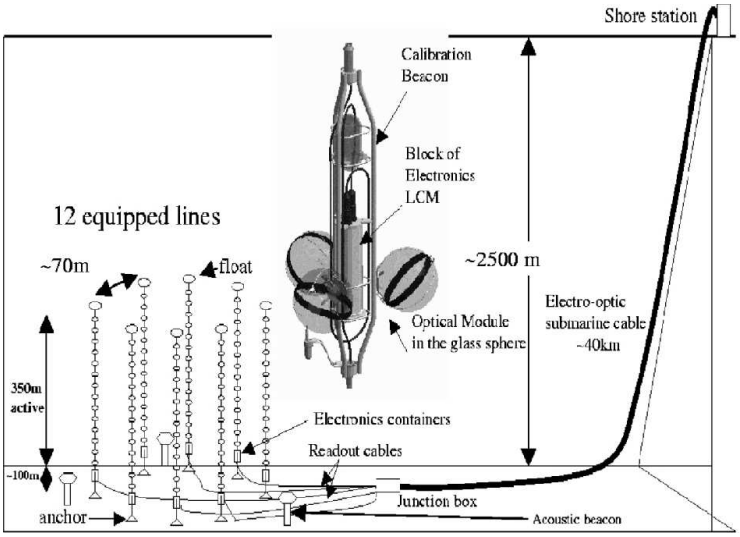

Figure 3.1. Schematic description of the ANTARES detector, showing the 12 detection lines, the Juction Box and the electro-optical cable. A storey is also represented in enlarged scale.

having a diameter of 43 cm and a thickness of 1.5 cm (figure 3.4).
The axis of the photocatode is looking downward at 45° from the vertical, to maximize the efficiency in the detection of upward going muon tracks and to avoid fouling and sedimentation effects. The optical coupling between the PMT photocathode and one of the hemispheres of the glass sphere is realized with a silicon gel (refractive index for the three media are: $n_{gel} = 1.40$, $n_{glass} = 1.48$, $n_{water} = 1.35$). The glass sphere also hosts the electronic system for photon pulses digitization. For time calibration purposes, an LED is located inside the sphere as well, so that it can illuminate the PMT photocathode. The inner surface of the back hemisphere of the glass sphere is covered with black paint, in order to absorb photons coming from the side of the OM opposite to the photocatode, and to reduce the risk of inner reflexions. Each PMT is also shielded by means of a μ-metal cage, to avoid the deviation of the trajectory of low energy electrons inside the photomultiplier by Earth's magnetic fields. The results of extensive R&D studies performed by the ANTARES Collaboration, concerning the OMs and the performances of PMTs are reviewed in [30].

- **Storeys and Local Control Modules**: the OMs are grouped in triplets of modules in a storey and mechanically fixed to the lines (figure 3.1). The accompanying electronics is contained in the so-called *Local Control Module* (LCM), a titanium cylinder housing the electronics boards for all the functionalities at the storey level.
  Five storeys make up a *sector*, which is a stand-alone unit concerning the power distribution and the data acquisition system (DAQ). One out of five storeys has a Master Local Control Module (MLCM). Inside a MLCM is located an Ethernet switch, a bidirectional concentrator and a Dense Wavelength Divi-

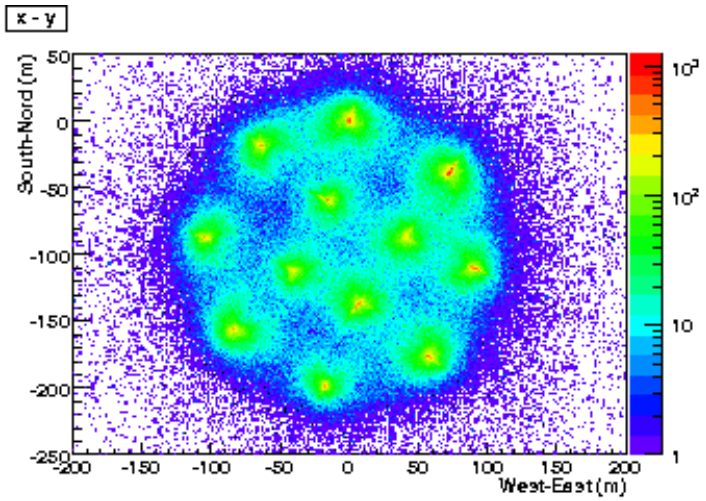

Figure 3.2. The ANTARES *footprint*: the figure shows the x and y coordinates of track fits at the time of the first triggered hit. Data from the first two weeks of running with the complete detector have been used: the detector layout, made of 12 detection lines is clearly visible.

sion Multiplexing board (DWDM) which multiplexes the signal information from the five storeys onto one optical fiber at a unique wavelength for that storey. The MLCM contains all the electronic boards for all the functionalities at the sector level.

- **Lines**: a full detection line, also called *string*, consists of five sectors (25 floors). The distance between adjacent storeys is 14.5 m, while the average spacing between lines is about 74 m. Each string is a flexible structure, held vertically by means of a buoy located in its upper end, and is anchored to the seabed by a dead weight located in the bottom string socket (BSS). The active part of each line starts at about 100 meters above the seabed in order to avoid the sea mud and dirt that can be spread out due to underwater currents, and to allow the development of the Čerenkov cone produced in the propagation of upward going muons through the detector. Apart from the LCMs, each string is instrumented with an electronics container in the base called String Control Module (SCM). In addition to the 12 detection lines, an additional *instrumentation line* is also available to perform detailed oceanographic and water properties measurements.

- **Juction Box**: each SCM is connected to the Junction Box (JB) which provides power and control signals and receives the data from the lines. The JB is connected to the shore station through the Main Electro-Optical Cable (MEOC). The internal elements of the JB are protected from water pressure and corrosion by a titanium structure. The JB is equipped with 16 connectors for the 12 lines, the instrumentation line and the spares.

- **Main Electro Optical Cable (MEOC)**: this element links the JB to the power hut, located on-shore. This power hut houses the power system and is

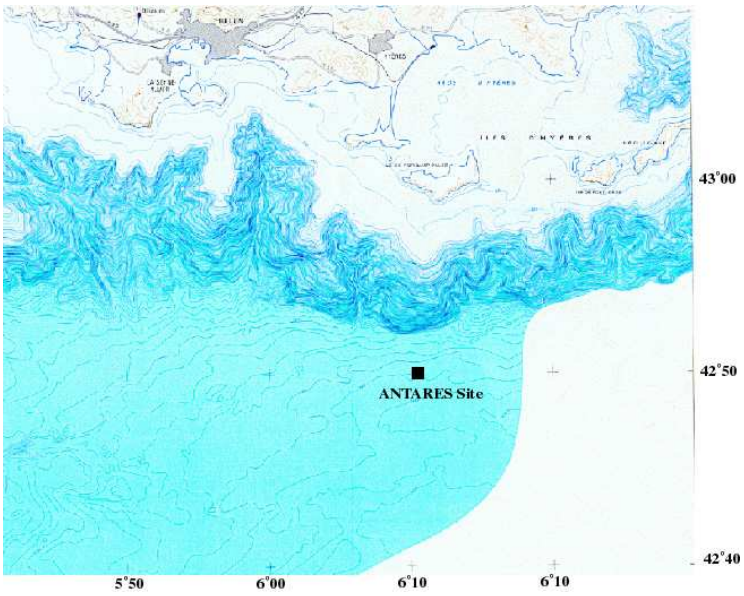

Figure 3.3. Location of the ANTARES site, France. The detector is at a depth of about 2500 m, at a latitude of 42°50′ N, and longitude 6°10′ E.

the first infrastructure on shore reached by the cables. The MEOC contains an internal steel tube and 48 optical fibers. The cable is a standard telecommunication cable and is protected and insulated by a set of external layers of copper and steel, to avoid possible failures and breakings.

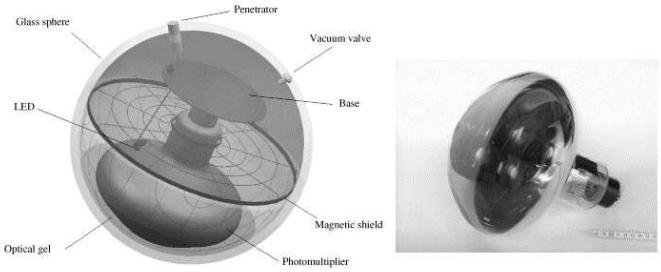

Figure 3.4. *Left:* Schematical representation of an optical module, the main component are indicated; *Right*: Picture of a photomultiplier tube [30].

3.1.1 Light transmission properties at the ANTARES site

Detailed studies of the light transmission in water are of fundamental interest in order to set constraints to the architecture of a deep-sea neutrino telescope: light absorption provides an upper limit to the distance between two sensors, which are used to search for time coincidences due to Čerenkov photons produced by the same muon track.
The speed of light in water is constrained by the refractive index of the medium itself. Absorption of light in water can reduce the efficiency of the detector, while the scattering of photons on water molecules or particulate can reduce the detector performances and in particular the angular resolution.
Water transparency can be parametrised as a function of two quantities, which are a function of the incident wavelength λ: absorption length $L_a(\lambda)$ and scattering length $L_b(\lambda)$.
These quantities indicate the path after which a photon beam of wavelength λ and intensity I_0 is reduced by a factor $1/e$, due to absorption and scattering phenomena respectively.
The *attenuation length* $L_c(\lambda)$ is used to characterize light transmission in water, being defined as $L_c(\lambda) = L_a(\lambda) + L_b(\lambda)$. Absorption and attenuation lengths for several deep underwater sites, selected for the realization of a neutrino telescope are shown in figures 3.5 and 3.6, as a function of the radiation wavelength.
Several sea campaigns were devoted to detailed studies of the environmental prop-

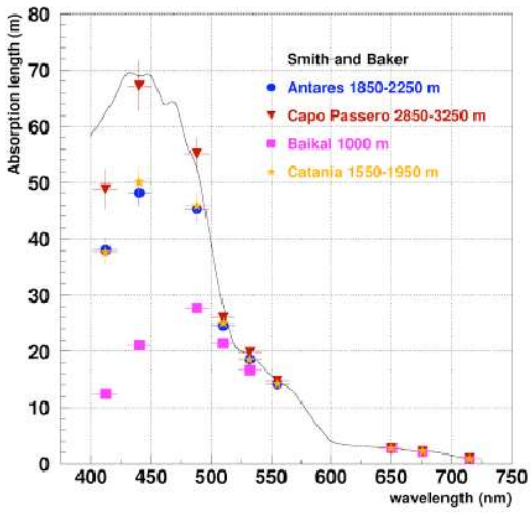

Figure 3.5. Absorption length as a function of the wavelength for several deep sea sites, compared to pure water (solid line) [110].

erties of the site and of the transmission of light in water: results of these sea campaigns are described in [17] and [31].

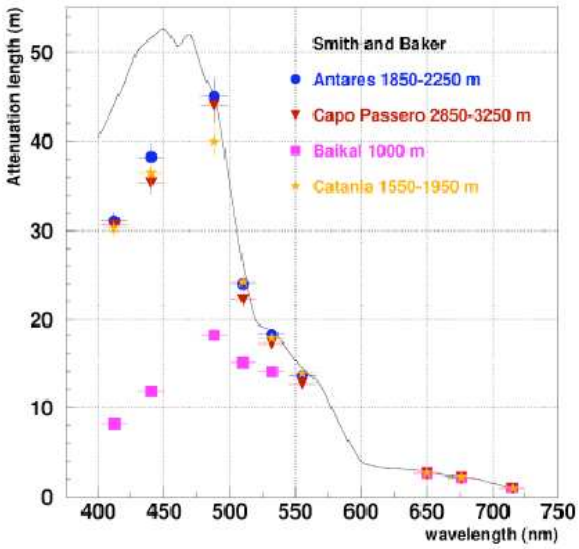

Figure 3.6. Attenuation length as a function of the wavelength for several deep sea sites, compared to pure water (solid line) [110].

3.2 Environmental background

The Čerenkov light induced as a consequence of the superluminal motion of the charged leptons is not the only kind of blue visible light which can be detected by a PMT located in deep sea water: biological activity in deep sea sites is known to produce light in an incoherent way.
Two natural phenomena are responsible for the production of light in deep sea water: Čerenkov light produced in the propagation of charged particles originating in the decay of radioactive elements in sea water, e.g. ^{40}K, and luminescence induced by biological organisms, the so called *bioluminescence*.
Several radioactive elements can be found in sea water, the most abundant is the ^{40}K, that has two main decay channels:

$$^{40}K \rightarrow {}^{40}Ca + e^- + \bar{\nu}_e \qquad B.R. = 89,3\% \tag{3.1}$$

$$^{40}K + e^- \rightarrow {}^{40}Ar + \nu_e + \gamma \qquad B.R. = 10,7\% \tag{3.2}$$

The electrons produced in the first process often have sufficiently high energy to induce the Čerenkov effect, while in the electron capture process, the photon in final state is produced with an energy $E_\gamma = 1.46$ MeV, which can easily lead to the production of electrons with energies over the threshold for Čerenkov light emission.
Light pulses due to ^{40}K decays have low amplitude (mostly 1 p.e.) and are uncorrelated on time scale of a few nanoseconds. However radioactive decays may produce many photons within 1 ns, giving raise to higher amplitudes on a single PMT or narrow coincidences on neighboring PMTs [51].
Bioluminescence is produced by bacteria and small marine organisms emitting blue visible light in deep sea environment. Signals from bioluminescence collected on

different OMs are correlated on the scale of seconds or milliseconds. The presence of these bacteria is moreover strongly dependent on the depth.
Two quantities can be used to characterize the light received over a given period of time: *baseline* rate, quantifying the continuous component of the background, and the *burstfraction*, i.e. the fraction of time with very high counting rates [63].
^{40}K decays and bioluminescence produce a continuous background, with single PMT rates usually between 60 KHz and 100 KHz. Peaks of biological activity can occasionally increase the counting rate up to several MHz. Figure 3.7 shows the typical background behavior during data taking. Background hits are mostly uncorrelated, so that they can be rejected by the trigger algorithm.
Marine environment is an optimal location for the development of biological or-

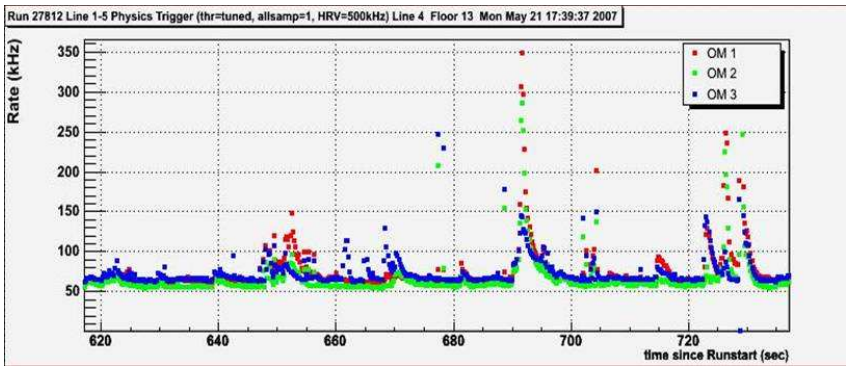

Figure 3.7. Optical background rate measured by three PMTs on the same storey of the ANTARES detector, in a time window of two minutes (May 2007).

ganisms which can grow up on *available* surfaces. The surface of optical modules, being underwater for several years, can be affected by the colonization of bacteria, a process which can lead to a reduction in the transparency of the glass spheres and thus to a reduction of the detection efficiency of the telescope. This process, called *biofouling*, has been investigated in several sea campaigns [31],[122] and will be described in the following section.

3.3 The biofouling effect at the ANTARES site

The transparency of pressure-resistant glass spheres hosting PMTs can be affected by the rise of bacteria colonies and sedimentation once these light detection modules have been underwater. The fouling process starts as soon as the apparatus is located underwater: a few minutes later, the surfaces start to be affected by bacteria colonies fouling, creating a very thin biofilm. The fouling process can also be affected by occasional sedimentation phenomena, which can be related to underwater currents.
A detailed study of glass spheres properties is needed since the biofouling effect can reduce the efficiency of the whole telescope: the photons can become unlikely to reach the photomultiplier, as a consequence of the transparency loss.
A slow reduction of glass spheres transparency is expected to occur as a function of time [31], [122]).

3.3.1 Experimental technique

A long data-taking period has been devoted to the evaluation of the biofouling effect at the ANTARES site: the apparatus has been underwater from June 2000 to October 2001.
The experimental device is composed of a square-shaped aluminum structure hosting four Benthos spheres, of the same kind of those used in ANTARES, containing light sources and detectors, a power-supply together with the data taking and storage device.
Figure 3.8 shows a sketch of the experimental apparatus: the blue spots represent the light sources (three blue Light Emitting Diodes), while the red dashed lines represent the light detectors, photodiodes.
The same apparatus had been previously used to characterize the biofouling effect at the Capo Passero site, candidate to host the NEMO deep underwater neutrino telescope (see section 2.3). Results of the study are discussed in [122].
In the following a description of the analysis technique will be given, together with the results concerning the transparency loss of the OMs as function of the latitude on the OMs itself, compared to those obtained for the Capo Passero site. The whole

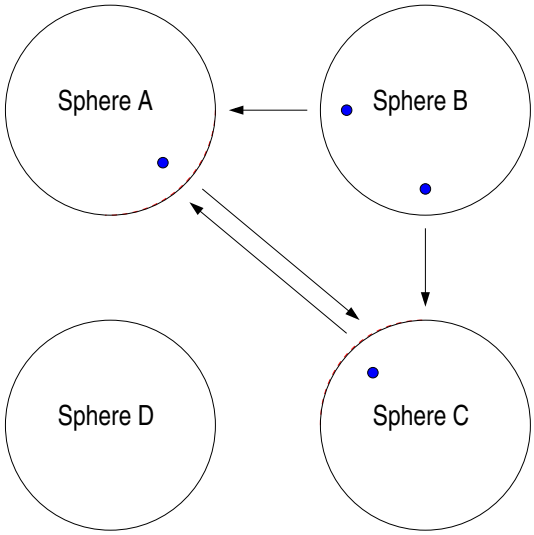

Figure 3.8. Experimental setup for the biofouling effect evaluation: the blue spots represent the light sources (three blue Light Emitting Diodes), while the red dashed lines represent the light detectors, photodiodes.

equipment can be summarized as follows:

- The sphere labelled as A contains the data acquisition system and the storage device, three blue LEDs, which are considered as a unique source, sixteen photodiodes (PINs), one tilt-meter and one compass which are used to monitor the device position variations respect to a fixed position.
- The sphere labelled as B contains the power supply for the whole system and six LEDs, grouped together in two different *light sources*.
- The sphere labelled as C contains three LEDs and sixteen photodiodes.

- The sphere labelled as D is empty and is mounted on the mechanical structure to balance it.

Photodiodes and LEDs have been homogeneously mounted on the spheres, at several latitudes and longitudes, to obtain a detailed study of the glass spheres transparency variation.
In this study we will label as the *sphere equator* the curve corresponding to a zenith angle $\theta = 0°$, while the sphere's North pole corresponds to $\theta = +90°$, as shown in

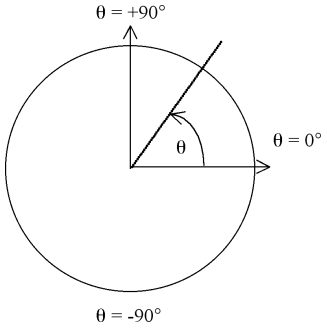

Figure 3.9. Latitude on the optical modules, as used in this analysis.

figure 3.9.
Every *light source* is made of three LEDs which can operate separately, so that two different light intensities can be produced: single LED light emission or coupled LED light emission. Each source is also equipped of two photodiodes so that we can monitor the emitted light and its possible unstable conditions.
The data-taking has been performed once every twelve hours. Pedestal data have been acquired for each photodiode before any data acquisition with LEDs. The acquisition foresees to switch each source on, setting the light emission at two levels of intensity. The chain goes on by switching each source on, using the two intensities, so that we had eight different acquisition configurations. As soon as one of the sources was switched on, the electric current collected by the photodiodes was converted in a voltage signal and finally digitized by an ADC (Analogic-Digital Converter).

3.3.2 Data analysis

The fouling can be evaluated by means of the following dimensionless quantity, as already done by the ANTARES Collaboration in [31]:

$$Transp(\theta, t) = \frac{\frac{Pin(\theta,t)}{Ref(\theta,t)}}{\frac{Pin(\theta,t=0)}{Ref(\theta,t=0)}} \tag{3.3}$$

This function, for a given latitude on the optical module θ and a given time t, compares the signal collected by a photodiode (indicated as $Pin(\theta, t)$) and the one collected by the corresponding reference photodiode.
Figure 3.10 shows the typical behavior of the function $Transp(\theta, t)$: we can see that

the function is characterized by a regular trend and by many fluctuations, both positive and negative, which are likely to be the effect of sedimentation processes.

We defined as *transparency variation speed*, the numerical derivative of the quan-

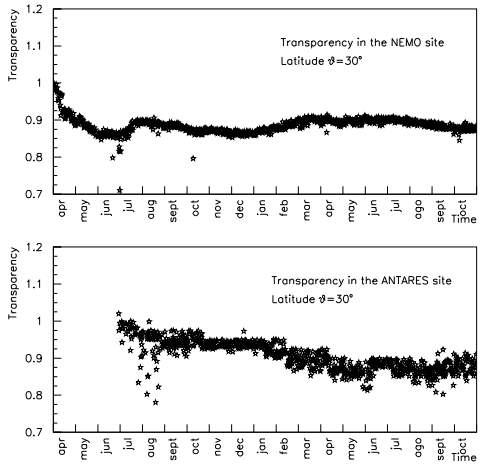

Figure 3.10. *General trend of transparency, estimated by the dimensionless quantity* $Transp(\theta, t)$*, as a function of time in the NEMO (top panel) and ANTARES site (bottom panel) for a given latitute* θ*.*

tity $Transp(\theta, t)$, that is the quantity:

$$\frac{\Delta Transp}{\Delta t} = \frac{Transp(t_i + t_{N+i}) - Transp(t_i)}{N} \tag{3.4}$$

we used N=50 to minimize fluctuations.

Figure 3.11a shows the transparency variation speed as a function of time, for a latitude $\theta = -30°$. We know that two different phenomena can contribute to the loss of transparency. The most regular contribution it thought to be caused by the the biofilm growing-up, while bigger transparency fluctuations are probably due to sediments.

Figure 3.11b shows the distribution of the transparency variation speed $\frac{\Delta Transp}{\Delta t}$. The same distribution has been obtained for all the *instrumented* latitudes.

We have experimentally checked that for a given latitude these distributions fit the sum of two Gaussian functions (G_1 and G_2). One of the gaussians usually has a smaller width, but it's higher: it represents the biofilm effect. The other gaussian is often broader and is likely to be produced by sedimentation processes. Figure 3.12 shows the $\frac{\Delta Transp}{\Delta t}$ distribution for a given latitude ($\theta = -15°$): the left histogram shows the parametrisation with one gaussian, while the right histogram shows the parametrisation with two gaussians. The second parametrisation fits better the data and takes into account broad tails corresponding to bigger fluctuations, both positive and negative.

We can parametrise the transparency variation speed using the mean value $\mu(G_i)$

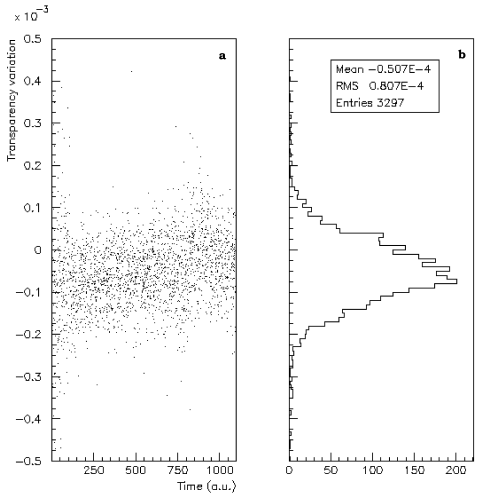

Figure 3.11. *Left panel(a):Transparency variation speed versus time (in arbitrary units) for* $\theta = -30^\circ$ *(NEMO site); Right panel (b):transparency variation distribution for* $\theta = -30^\circ$.

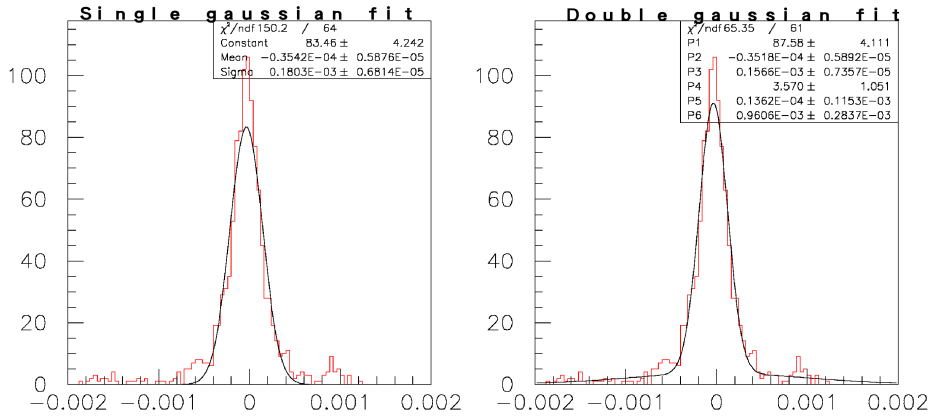

Figure 3.12. $\frac{\Delta Transp}{\Delta t}$ *distribution for* $\theta = -15^\circ$. *On the left we have the distribution fitted with a gaussian function, on the right we have the distribution fitted with two gaussians, as in formula 3.5.*

and the area $A(G_i)$ of these curves, obtained by the fit:

$$\frac{\Delta Transp}{\Delta t} = \frac{\mu(G_1)A(G_1) + \mu(G_2)A(G_2)}{A(G_1) + A(G_2)} \tag{3.5}$$

We are looking for a relation between transparency variation speed and the latitude on the optical modules.
The fouling effect measured by a given photodiode is the result of the fouling occurring on the two glass regions where the light source and the detector are located, so that the transparency variation measured by a given photodiode should be computed as the sum of two different terms:

$$\frac{\Delta Transp(\theta_S, \theta_D)}{\Delta t} = \frac{\Delta Transp(\theta_S)}{\Delta t} + \frac{\Delta Transp(\theta_D)}{\Delta t} \tag{3.6}$$

where the two angles θ_S and θ_D refers to the source and to the detector latitudes.
Given the sources and the detector latitudes and making the assumption that the effect is the same at equal latitudes, even if on different OMs, we can calculate the transparency variation speed for several latitudes.
Concerning the ANTARES data, for technical reasons we used as a starting point the value obtained by the ANTARES collaboration in [31]: a -2% transparency loss per year at the OM equator.
Figure 3.13 shows the transparency variation, expressed in % per year, as a function of latitude on OMs for the two sites: results from the two samples of data, taken in the two sites, are in good agreement.
Transparency variation is given in % per year, this means that the values obtained as previously explained are then multiplied by a constant factor to give the annual values. These values are evaluated considering the fouling process as constant with time.

Comparing these results with the ones obtained with the same technique in the Capo Passero site [122] at 3000 m depth, we can observe that both sites are affected by the fouling process quite in the same way. It is noteworthy that the glass spheres transparency variation becomes more and more negative as a function of the increasing latitude respect to the equator of the OMs: we have a -2% per year transparency loss at the equator in the Toulon site, as already estimated by the ANTARES Collaboration in [31], which is slightly higher than the value $(-0,76\%)$ obtained in the Capo Passero site.
Upward-looking surfaces transparency variation is quite important in both sites, and can even reach values close to -10% per year at latitudes bigger than $\theta = +45°$ respect to the equator: this worsening in the transparency conditions is related to sedimentation processes which more frequently take place on the upward-looking surfaces than on the others. To avoid this effect not the ANTARES nor the NEMO telescopes photocatodes are upwards oriented, but their minimum polar angle is close to the equator for the ANTARES telescope and around $\theta = +30°$ degrees for the NEMO telescope. Given this peculiar orientation of the detectors we can estimate that the biofouling will not produce a dramatic efficiency loss in the high-energy neutrino detection framework even after ten years of data taking underwater.

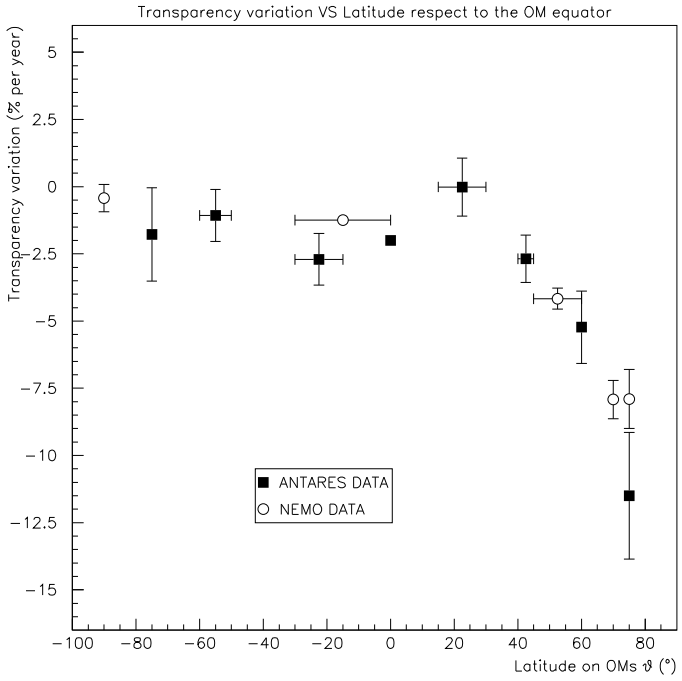

Figure 3.13. *Transparency variation, expressed in % per year, as a function of the latitude on the optical module: the full squares represent ANTARES data, while the empty circles represent the NEMO data, taken from [122].*

3.4 Calibration

The performances of the ANTARES detector, in particular its pointing accuracy, are closely related to the precision in the determination of the arrival time of the Čerenkov photons on the PMTs. Moreover, as the detector units are mounted on flexible strings and the detector is exposed to sea currents, real-time positioning is needed. Charge calibration is also performed to monitor possible PMT ageing effects that could reduce the detector performance. An overwiev of the calibration procedures will be given in the following.

3.4.1 Time Calibration

The ANTARES Collaboration has estimated [119] that for each PMT a precision at the level of 0.5 ns in the determination of the hit time is required to achieve an angular resolution of the order of 0.3° for muons above 10 TeV for the full detector. Detailed informations about the transmission of light signal in the water surrounding the detector can be obtained by means of different calibration devices which are integrated in the detector.

Clock system

A 20MHz reference clock signal, generated on shore, is converted to optical signal and distributed to each storey, in order to evaluate the individual time offsets, by measuring the return time of the signal. The offsets are stable within 0.1 ns. Furthermore the internal clock makes it possible to assign an absolute GPS time-stamp to the data. This procedure leads to the definition of the absolute time with a precision of 100 μs, which is adequate for the purposes of neutrino astronomy, in order to search for correlations with other external observations (SN, GRBs,...).

Internal OM LED

Each OM hosts a blue LED which can be flashed to obtain relative variations in the PMT transit time (from the photocathode to the read-out electronics).

LED and Laser Beacons

To perform a relative time calibration of different OMs and monitor light propagation in sea water, a set of LED optical beacons (LOB) and Laser beacons [11] is used. Each ANTARES line is equipped with four LOBs which contain 36 blue LEDs arranged in groups of six on vertical boards forming a hexagonal cylinder. The individual LEDs have been synchronized in the lab to better than 0.1 ns. In situ calibrations are performed regularly, usually once a week, by flashing dedicated configurations of all these light sources.
As an example, figure 3.14 shows the distribution of time differences between emission of light from the LOB on the second storey of line 1 and the arrival time on the three OMs located on the above storey. Due to the short distance between the two adjacent storeys (about 14 m) and the high intensity, effects of light scattering, transit time spread in the PMT and line geometry can be neglected. The width of the distribution reflects the time resolution of the read-out electronics.

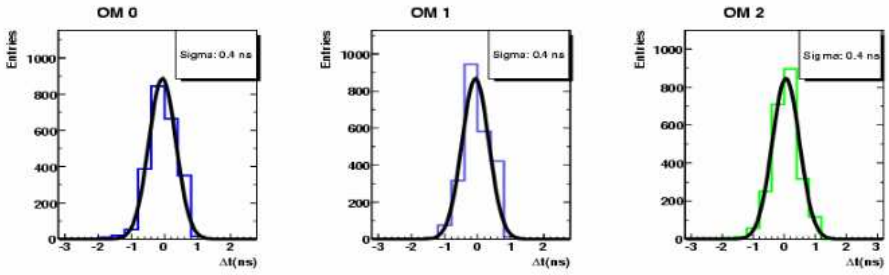

Figure 3.14. Distribution of time difference between emission and arrival of light from LOB on line 1 floor 2 illuminating the three OMs on floor 3 of the same line (mean values have been shifted to zero) [11].

3.4.2 Alignment

The absolute positioning of the 12 lines has been performed at the time of the deployment, using low frequency long baseline acoustic triangulation from the ship, connected to the GPS satellites.
The strings are flexible structures which can bend by deep sea currents, which have typical values of the order of some cm/s. Two positioning systems are used and integrated in the detector.
The acoustic positioning system [49] relies on the measurement of the travel times of acoustic pulses, in the range of 40-60 KHz, emitted by devices located at the BSS of each line. Along each line there are five hydrophones, in order to detect acoustic signals emitted. The transmitters are also able to receive signals. Figure 3.15 shows, as a result of the analysis of the signals received by hydrophones on one ANTARES detection line, the horizontal displacement from the *nominal* position, of each one of the five hydrophones. Four additional autonomous transponders are located around the detector to increase the accuracy of the global alignment.
In addition to the acoustic positioning system, each LCM is equipped with tiltmeters and compasses, to measure pitch, roll and heading of the whole storey.
The positioning system is designed to measure the position of each OM within 10 cm or less.

3.4.3 Charge Calibration

The charge calibration and threshold tuning of the photomultipliers and their associated front-end electronics enables to translate PMT signal amplitudes into number of photoelectrons, which is the basic information for both tracks and energy reconstruction [40].
Two Analogue Ring Sampler (ARS) chips, working in *token ring* mode, sample the signal collected by each PMT, recording its charge and time, as will be discussed in section 3.6.
The signal sampled by one ARS is then digitized by two integrated Analogic-Digital Converter (ADC). A 20 MHz reference clock is used for time stamping the signals, while a Time-to-Voltage-Converter (TVC) device is used for high resolution time measurements between clock pulses.

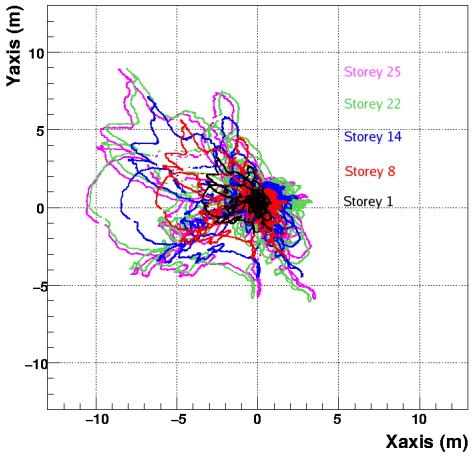

Figure 3.15. The horizontal movements from BSS, of all hydrophones on Line 11 for a 6 month period. The black curve represents data from hydrophone on floor 1, red curve represents floor 8, the blue curve is floor 14, the green curve is floor 22 and magenta is floor 25 [93].

The ARS chips were calibrated before their deployment, in order to measure the transfer functions of the Amplitude to Voltage Converter (AVC). In situ calibrations are performed regularly, to monitor the detector response and PMTs gain evolution. Low level trigger data, with a large fraction of hits due to ^{40}K decays and bioluminescence, mainly result in single photon hits at the photocatode level. They are collected to study the charge distribution and its *single photoelectron peak* (spe). The measurement of the spe peak, and of the pedestal, is used to estimate the charge over the full dynamical range of the ADC. The values in AVC channels of the pedestal and the spe peak are used to convert individual measurements into photoelectron units.

As an example of the use of *low level trigger data* to study the detector behavior,

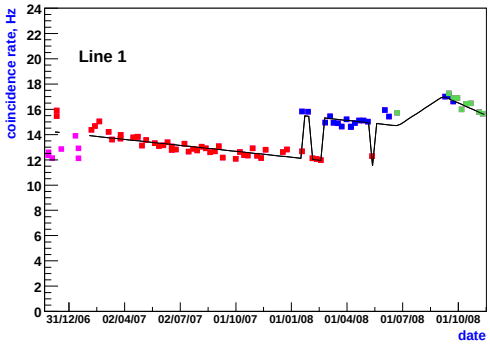

Figure 3.16. Time evolution of the counting rate due to ^{40}K decays, measured with the first line of the ANTARES detector. Colors account for different threshold setting periods [40].

figure 3.16 shows the counting rate of Line 1, due to ^{40}K, as a function of time:

a regular decrease is visible up to April 2008. This gain drop effect is thought to be due to ageing effect of the PMT photocatodes. Gain seemed to be partially recovered when PMTs had been off for some time, because of the MEOC failure in summer 2008.

3.5 Physical background

The ANTARES telescope has been designed and realized to detect cosmic neutrino induced muons. The search for cosmic neutrinos is then affected by a huge background: muons and neutrinos generated in the interactions of charged cosmic rays in the Earth atmosphere, showing the same experimental signature that characterize cosmic neutrinos, as in figure 3.17.
Primary cosmic rays interact in the atmosphere with air molecules and initiate air showers, producing charged mesons which are likely to decay and produce muons and neutrinos. Neutrinos produced by cosmic rays interactions can traverse the

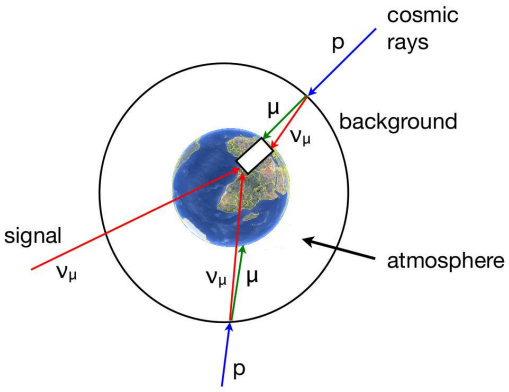

Figure 3.17. Schematic description of the different sources of muons that can be detected in a deep sea neutrino telescope: atmospheric muons as well as cosmic and atmospheric neutrino induced muons. These events have the same experimental signature in the detector.

Earth, interact via charged current in the vicinity of the detector and produce muons.
The detector is located deep underwater in order to reduce the exposure to the flux of atmospheric muons: despite the water column over the detector, the muon flux is greatly reduced but not completely negligible. Figure 3.18 shows the vertical intensity of atmospheric muons, as a function of the depth, expressed in km water equivalent, for the first ANTARES line, compared to the results obtained by other experiments.
The flux of muons produced by atmospheric muons and atmospheric neutrinos is shown in figure 3.19: it can be seen that atmospheric muons reaching the detector are only propagating as down-going through the medium surrounding the telescope, while atmospheric neutrinos have nearly isotropic arrival directions, so that they should be considered as an irreducible background. Around horizontal direction, corresponding to $cos\theta = 0$, the flux of atmospheric neutrinos is enhanced due to the increased path length in the upper atmosphere, which favors mesons decays,

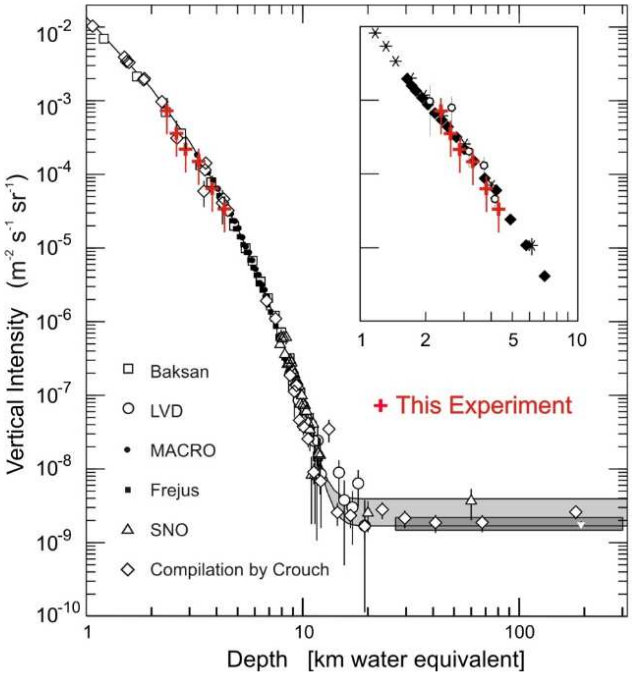

Figure 3.18. Vertical muon intensity versus depth. Crosses are the results obtained during 2006 with the first operational detection line of the ANTARES detector [12]. Data from other experiments are shown as a reference. The shaded area at large depth represents neutrino-induced muons of energy above 2 GeV.

and consequently neutrino production, with respect to their interactions. The discrimination of atmospheric neutrino background is possible only at the end of the whole analysis chain. In case a statistically relevant excess of signal is found to be clustered in the sky-map, the flux can be considered to be produced by a point-like source, since this peculiar experimental signature is in contrast with the isotropic flux of atmospheric neutrinos.
The detection of an astrophysical component of high energy neutrinos will be possible even without the identification of point-like sources. Astrophysical neutrino energy spectrum is less steep than that of atmospheric neutrinos, as seen in picture 1.1: above $1 \div 10$ TeV several models foresee that astrophysical neutrino flux (diffuse flux) will exceed the atmospheric one.

3.6 Data acquisition system, trigger and event selection

The data acquisition system (DAQ) [18], [48] of the ANTARES telescope has been specifically designed for the digitization of the PMT signals, the transport, the filtering and the storage of data (figure 3.20).
The ANTARES DAQ can be thought of as an elaborate and extended network consisting of hundreds of processors, located both on-shore and off-shore. While on-shore processors are standard PCs located in the shore-station, the off-shore processors are integrated in custom-made electronics.

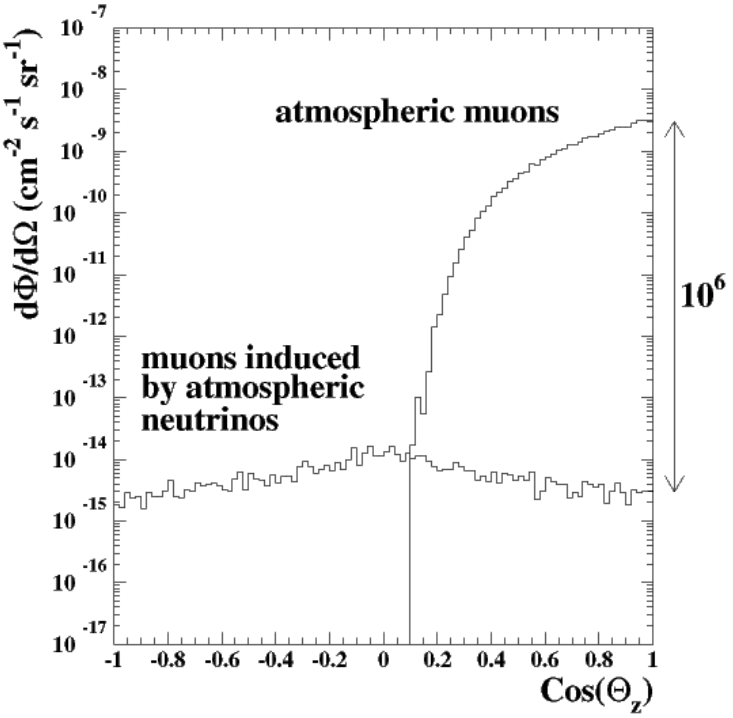

Figure 3.19. Flux of atmospheric muons and of atmospheric neutrino induced muons, as a function of the cosine of the zenith angle, indicating the arrival direction. $cos\theta = 1$ indicates that the muon is propagating downward through the detector, while $cos\theta$ = -1 indicates that the neutrino induced muon is seen as upward-going through the telescope.

A pulse generated by a PMT anode is sent to two **Analogue Ring Sample (ARS)** chips, working in token ring mode, to minimize the dead time. These chips sample the PMT signals at a tunable frequency, up to 1 GHz. Once the signal is received by one ARS, it is discriminated according to an amplitude threshold whose value is tunable and usually set to 0.3 spe. If the signal exceeds this threshold, this condition is usually referred to as $L0$, it is integrated in a time window of 35 ns.
ARS digitize the timing of each PMT signal, together with the total charge of the pulse. A **local clock** is used by the ARS chips to time-stamp each PMT signal above the $L0$ threshold.
The results of the digitization of six ARS located on one storey, together with the data coming from the compass card and from the acoustic modules are sent to the DAQ board of the corresponding Local Control Module (LCM) and are collected at a fixed time interval.
The readout system of the ARS chips is implemented in a high density **Field Programmable Gate Array (FPGA)** XilinX Virtex-E XCV1000E. The data from the ARS chips are buffered by the FPGA in the **64 MB SDRAM**.
Data from the five LCM of a sector are sent to a Master Local Control Module (MLCM), having a Gigabit ethernet switch that combines all the signals from different DAQ boards into one channel, and a Dense Wavelength Division Multiplexing board (DWDM) that converts the signal received into optical wavelengths .
Data collected from each MLCM are sent to the String Control Module (SCM) at

a frequency of 1 Gb/s: the SCM collects the signals from MLCMs and from the SCM itself and combines 6 signals in one fiber. The signals from each SCM are finally sent to the Junction Box and then to the shore station with a single 40 km long electro-optical cable: each sector and each string module has a unique pair of wavelengths that is used to transmit the data. On shore, a multiplexer and a demultiplexer are available for each detector string. The DWDM is also used for the transmission of the slow control data (compass, tilt-meters, sea current *etc.*) and the distribution of initialization and configuration data.
The on-shore part of the DAQ system is located in the shore station. It consists of a large Ethernet switch, the DWDM hardware, the master clock system together with a farm of standard PCs, devoted to data processing.

3.6.1 Data Taking and Data Processing

During data taking, all signals recorded by the PMTs and digitized by the ARS are sent to shore without any further data selection.
As a results of this *all-data-to-shore* architecture, all raw data are available on shore where the required processing methods can be applied to the data.
The DataFilter process receives the raw data from the off-shore DaqHarness processes, running on each off-shore processor.
All data that are produced by each ARS chip in a certain time window, set between 10 and 100 ms, are buffered in what is called a **frame**. The frames from all DaqHarness processes that belong to the same time window are sent to the same PC in the on-shore data processing system, identified by the IP address.
The collection of frames belonging to the same time window is called a **time slice**. As a result, a time slice contains all data that were recorded during the same time interval by all ARS chips in the detector. When a sufficient number of correlated single photo-electron (SPE) hits is found to be consistent with a specific physics signal, the data are considered a physics events, and written to disk. The duration of a time slice is long if compared to the duration of a physical event in the detector (approximately 1 μs), in order to minimize the number of events crossing the boundaries of a time slice.
The algorithms implemented in the data processing software are designed to find a physical signal by looking for space-time correlations in the data. From the time of the SPE hits, and the position of the PMTs, these algorithms calculate in real-time if hits could originate from light produced by muons traversing the detector, or other kind of interesting physical signatures.
The ANTARES site is characterized by high background rates, as seen in figure 3.7, of the order of 70 KHz in low bio-activity periods, caused by bioluminesce and ^{40}K decays. The data output is processed by the DataFilter software, that run on each processor in the shore station PC farm. The physics signals selected by the DataFilter are passed to the DataWriter, which formats the events and writes them to disk in ROOT format [108].

3.6.2 Trigger algorithms and event selection

The triggering procedure is performed via software: a wide variety of algorithms is used to filter data from environmental background. With the *all-data-to-shore*

architecture, different software triggers can be operated simultaneously. At present, several general purpose muon triggers and one minimum bias trigger are used for data taking. The minimum bias trigger is used to monitor the data quality.
A first level trigger is verified if one of these conditions are satisfied: two or more hits occurring on the same storey within a time window of 20 ns or hits with a charge bigger than a certain value, labelled as *high-threshold* (usually 3 or 10 spe). Hits satisfying these conditions are labelled as L1. The choice of the 20 ns window is such that time delays due to the difference in position of the PMTs and scattering effects are taken into account.
A *level 2* trigger searches for correlations between all hits already selected in the first level trigger.
The *standard* trigger algorithm makes use of the general causality relation:

$$|t_i - t_j| \leq |\vec{x_i} - \vec{x_j}| \times \frac{n}{c} \tag{3.7}$$

where t_i refers to the time and $\vec{x_i}$ to the position of the hits, n indicates the refractive index of sea water and c the speed of light. A hit selection procedure must be applied to reduce the rate of accidental coincidences, searching for 5 causally connected L1 hits.
The trigger algorithm which is called **T3** is based on the search for clusters of L1 hits on adjacent storeys or on next-to-next storeys located on the same line. Moreover also clusters of hits in adjacent storey located on adjacent lines are considered.
A trigger that tracks the Galactic Center position is also used to maximize the detection efficiency of neutrinos coming from the Galactic Center.
The dominant contribution to the triggered data stream is due to atmospheric muons traversing the detector, resulting in rates whose values depend on the particular choice of the trigger logic, between $2 \div 10$ Hz.
At the trigger level, no distinction is made between events due to atmospheric muons, atmospheric neutrinos or cosmic neutrinos.

3.7 Detector Performance

The quantities that better describe the performances of the telescope are the effective area and the angular resolution, and will be introduced in the following. Since these quantities are also related to the specific algorithm that is used to reconstruct muon tracks, the corresponding plots, as function of the neutrino energy, will be shown in section 5.5, where the reconstruction algorithms used within the ANTARES Collaboration will be widely discussed.

- **Effective Area:** It is defined as the size of a 100% efficient surface that detects the same number of through-going neutrinos (or muons) as the ANTARES detector, for a given neutrino flux. Neutrino effective area indicates a quantity that can be multiplied by a given differential neutrino flux and integrated over the neutrino energy (E_ν) and arrival direction (θ_ν, ϕ_ν), to obtain a rate of observed events. The neutrino effective area is computed from the number of selected events with respect to the generated neutrino flux incident at Earth,

and is given by:

$$A^{\nu}_{eff}(E_\nu, \theta_\nu, \phi_\nu) = \frac{N_{sel}(E_\nu, \theta_\nu, \phi_\nu)}{N_{gen}(E_\nu, \theta_\nu, \phi_\nu)} \cdot V_{gen} \cdot \rho N_A \cdot \sigma(E_\nu) \cdot P_{Earth}(E_\nu, \theta_\nu) \quad (3.8)$$

where N_{sel} indicates the number of neutrino events fulfilling the selection criteria after muon reconstruction, N_{gen} indicates the number of generated neutrino events over the generation volume V_{gen}. The term $\sigma(E_\nu)$ indicates the neutrino cross section, the term ρ indicates the Earth target nucleon density, while the N_A is the Avogadro's number. The probability of transmission through the Earth is indicated in the formula by $P_{Earth}(E_\nu, \theta_\nu)$.
The muon effective area is expressed again as a function of the neutrino energy and arrival direction, as:

$$A^{\mu}_{eff}(E_\nu, \theta_\nu, \phi_\nu) = \frac{N_{sel}(E_\nu, \theta_\nu, \phi_\nu)}{N_{gen}(E_\nu, \theta_\nu, \phi_\nu)} \frac{V_{gen}}{\langle R^{\mu}_{eff}(E_\nu \rangle} \quad (3.9)$$

where $\langle R^{\mu}_{eff}(E_\nu) \rangle$ is the average muon range defined as:

$$\langle R^{\mu}_{eff}(E_\nu) \rangle = \int \frac{dP_\mu}{dE_\mu} R_{eff}(E_\mu) dE_\mu \quad (3.10)$$

where $\frac{dP_\mu}{dE_\mu}$ indicates probability for a neutrino to produce a muon of energy dE_μ, and $R_{eff}(E_\mu)$ indicate the muon range, i.e. the distance traveled by a muon of energy E_μ before its energy drops below a given energy threshold.

- **Angular Resolution:** It is computed as the median of the distribution of the space angle between the true and the reconstructed direction of the simulated muon tracks.
  The detector allows for the reconstruction of the muon direction that is related to the neutrino direction by kinematics. The average angle $\langle \theta_{\nu\mu} \rangle$ decreases as a function of the increasing neutrino energy E_ν, as indicated by the relation:

$$\langle \theta_{\nu\mu} \rangle \sim \frac{0.7^\circ}{\sqrt{E_\nu [TeV]}} \quad (3.11)$$

  This effect limits the resolution in the reconstruction of the neutrino direction at low energies. At energies above 10 TeV the angle is due to experimental uncertainties.

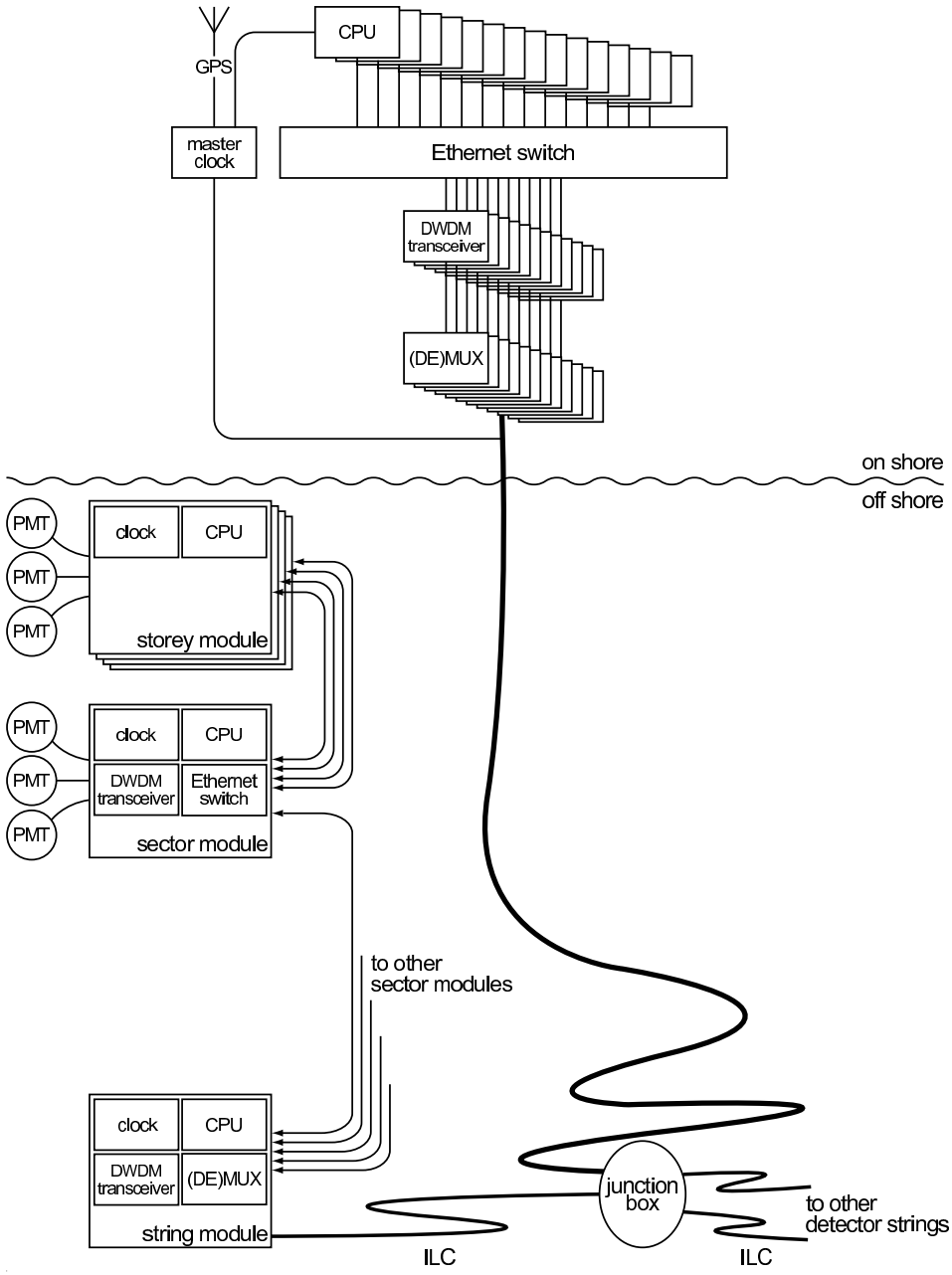

Figure 3.20. Schematic picture of the ANTARES data acquisition system, from [18]. The structure of only one detector string is shown. See the text for a detailed explanation.

Chapter 4

Physics goals with the ANTARES data

The major goal of the ANTARES experiment is the search for high energy neutrinos of astrophysical origin. This search is performed by looking for upward going neutrino-induced muon tracks out of the huge amount of the downgoing atmospheric muons. The optimal angular resolution needed to perform neutrino astronomy can be achieved with an accurate reconstruction algorithm, as described in the next chapter: Monte Carlo simulations show that the full detector will be able to achieve a pointing accuracy better than 0.3° above 10 TeV.
Additional event properties, e.g. the energy of the incident neutrino or the direction of the hadronic shower at the vertex, must be taken into account when pursuing different physics topics.
Besides the search for point-like steady sources, other physics topics are relevant for a deep sea neutrino observatory.
This chapter is intended as a short overview of the analysis topics that are pursued within the ANTARES Collaboration. Further information on each physics topic, as well as on the analysis itself, can be found at the suggested references.
A search for TeV $\div$ PeV neutrinos from unresolved sources with the ANTARES detector is described in section 4.2. This diffuse neutrino search aims at the identification of an extraterrestrial neutrino flux from sources with non-thermal behavior. The signal is expected to have a harder spectrum than that of the background from atmospheric muons and neutrinos.
The search for neutrinos from transient sources is performed in collaboration with other experiments and techniques, following a multimessenger approach: alerts received from γ-ray satellites are used as *external trigger* for neutrino searches in ANTARES; specific event configuration detected in ANTARES is used to trigger an optical follow-up with external *traditional* large field of view telescopes.
Indirect search for dark matter is in progress: predictions of neutrino fluxes originating from dark matter annihilation in the Sun have been obtained and a search for a neutrino excess in the direction of the Sun has been performed with 2007 data.
Atmospheric neutrinos can be used to investigate neutrino oscillations and possible Lorentz invariance violation. The search for exotic particles, e.g. magnetic monopoles and nuclearites, is ongoing within the Collaboration. The basic ideas of

the analysis presented in this thesis work are presented in section 4.7.
The most recent analysis have been performed on data taken in 2007, when the detector was only composed of 5 lines. From January 27th to December 4th, more than 19 million muon triggers had been accumulated during 245 active days. In order to exclude periods with high environmental background, only runs with a baseline smaller than 120 kHz and a burst fraction smaller than 40% were used, reducing the sample to 168 active days.

4.1 Point-like sources search

Several search algorithms have been developed to search for point-like neutrino sources. The method that is most widely used within the Collaboration is based on the Expectation-Maximization algorithm (EM), a sort of likelihood maximization [15]. In addition, a method looking for deviations from the expected distribution of angular distances on the neutrino sky-map (autocorrelation) has also been used.
The analysis is still ongoing within the Collaboration, searching for signals from a list of selected sources, which are likely to emit neutrinos within the ANTARES field of view. The list used in this analysis [120] is mainly based on flux predictions obtained by $\gamma-$rays observations.

4.2 Diffuse neutrinos

The search for a diffuse neutrino flux, i.e. unresolved (neither in time nor in space) neutrino sources, is based on the search for an excess of high energy (TeV $\div$ PeV) events above the irreducible background of atmospheric neutrinos. The observations of the diffuse fluxes of γ-rays and cosmic rays have been used to set theoretical upper bounds on the diffuse neutrino flux. The Waxman-Bahcall (WB) upper bound from cosmic ray observation is [124]:

$$E^2\,\Phi \leq (2 \times 10^{-8}\xi)\,GeV cm^{-2} s^{-1} sr^{-1} \tag{4.1}$$

where $\xi \simeq 1$ and depends on the model of the redshift energy loss of neutrinos.
The WB limit was extensively discussed in [98, 107], where a bound for a possible flux of extra-galactic neutrinos in the energy range 10^{14} eV $\leq E_\nu \leq 10^{20}$ eV was obtained. Two extreme kind of sources were considered: opaque and transparent to neutrons. The bound obtained for transparent sources is in agreement with the above formula in the range 10^{16} eV $\leq E_\nu \leq 10^{18}$ eV, but is higher outside. The limit for sources opaque to neutrons is $E^2\,\Phi \leq 2 \times 10^{-6} GeV cm^{-2} s^{-1} sr^{-1}$.
Monte Carlo simulation of the full detector performances was used to obtain the detector sensitivity, depending on the expected signal and background, and is shown in figure 4.1, with the present knowledge of the detector. ANTARES can constrain theoretical models on extra-galactic neutrino production and reach the level of few times the WB upper bound in 3 years of operation.

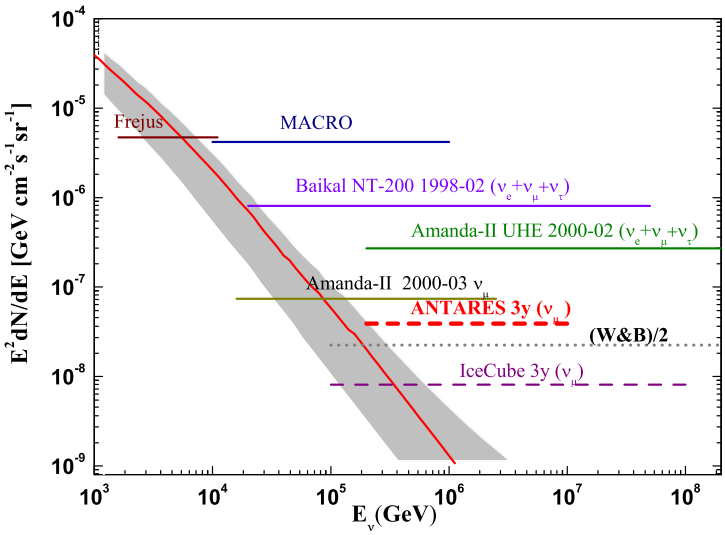

Figure 4.1. Sensitivities and upper limits for a E^{-2} diffuse high energy neutrino flux. Experimental upper limits are indicated as solid lines, the ANTARES and IceCube 90% C.L. sensitivities with dashed lines. The Frejus, MACRO, Amanda-II 2000-03 limits refers to ν_μ. The Baikal and Amanda-II UHE 2000-02 refers to all-flavors neutrinos. For reference, the Waxman and Bahcall limit,taking into account neutrino oscillations, for transparent sources is also shown.

4.3 Neutrinos from transient sources

Transient sources offer a unique opportunity to detect high energy neutrinos, the background of atmospheric muons and neutrinos being strongly reduced in the narrow observation time window.
Two strategies are implemented in ANTARES to search for neutrino events from transient sources: a *triggered search* method [93] and a *rolling search* method [62].
The *triggered search* method, schematically described in figure 4.2, is based on the alerts received by $\gamma-$rays satellites which are within the GCN[1] network. The ANTARES data acquisition system is able to receive a GRB alert. As a consequence, a dedicated data-taking, without any filtering, is performed for two minutes around the external alert. The small, but not yet well constrained, time difference between photons and neutrinos allows for an efficient detection by reducing the associated background. Due to a continuous buffering of data and to the very fast response of the GCN network, ANTARES is able to record data taken also before the time of the alert.
Analysis is on-going looking for correlation between alerts and candidate neutrino signals. Due to the very low background rates, the detection of a limited number of neutrinos in correlation with an alert would set a discovery.
The *Rolling search method* [88] has the main advantage to be suitable for the de-

[1]Gamma ray bursts Coordinate Network

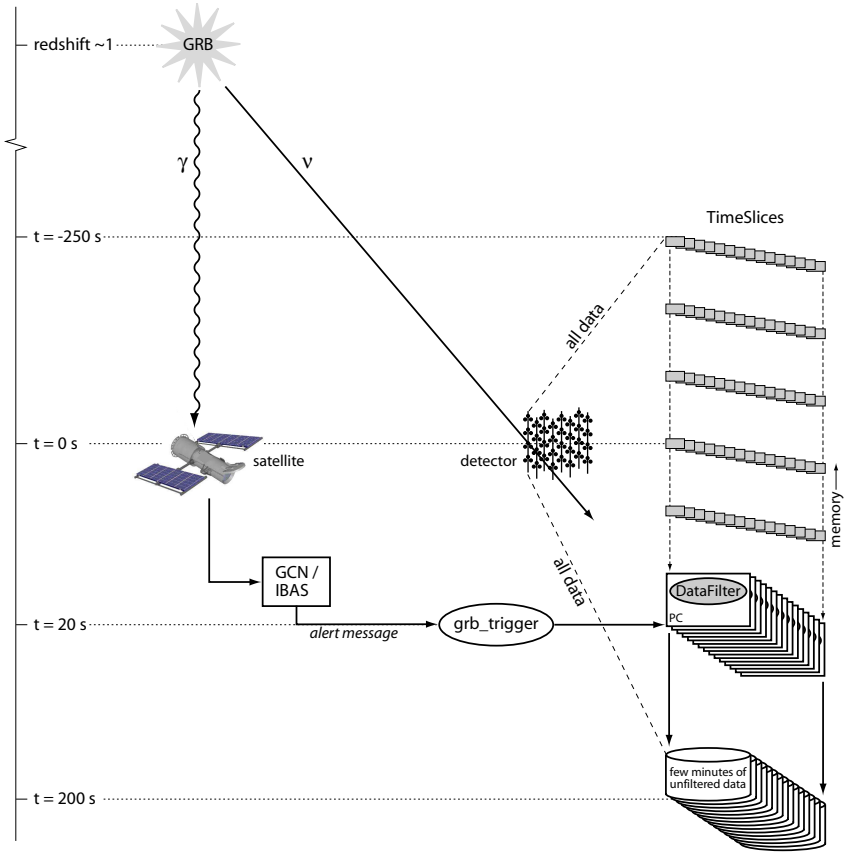

Figure 4.2. Schematic description of the satellite *triggered search* for neutrino emission from GRBs.

tection of neutrinos from any transient source, even for those which does not show photon counterpart. Since the beginning of 2008, ANTARES has implemented, together with traditional off-line reconstruction strategies, a fast *quasi* on-line event reconstruction software (between 5 and 10 ms per event) which shows an acceptable angular resolution, obtained without the dynamic reconstructed geometry of the detector. Using this algorithm, that is described in the following chapter, it is possible to search, in *real-time*, for clusters of neutrino events coming from the same region of the sky (about $3^\circ \times 3^\circ$) in a narrow time interval (15 minutes). This method does not imply assumptions neither on the nature of the source, nor on the mechanism that has produced neutrinos, implying that a detection is not necessarily associated to a known astrophysical source.
A complementary optical follow up program has been organized and started since February 2009, in collaboration with TAROT[2]. The telescope, with a large field of view ($1.86^\circ \times 1.86^\circ$) and a fast positioning time (less than 10s), is composed of two 25 cm optical robot telescopes located in Calern (France) and La Silla (Chile).
A confirmation, made by the optical telescope, of the existence of a transient source first detected by a neutrino telescope would be fundamental to understand the nature of the source and moreover to increase the precision in the determination of

[2]Télescope á Action Rapide pour les Objects Transitoires

the source direction.

4.4 Dark matter search

Indirect search for dark matter can be performed in ANTARES by looking for a neutrino excess from celestial bodies like the Sun or the galactic center. Neutrinos could be produced in the annihilation of weakly interacting massive particles, e.g. neutralinos, which become gravitationally trapped in celestial bodies.
A minimal super gravity approach (mSUGRA) has been followed to evaluate the expected flux of neutrinos from dark matter annihilation in the Sun: the model is characterized by four free parameters and a sign: $m_{1/2}$, m_0, A_0, $tan(\beta)$ and $sgn(\mu)$.
A dedicated analysis of 2007 ANTARES data has been performed [94] in order to search for a possible excess of the neutrino flux from the Sun. The analysis has been restricted to data taken whit the Sun below the horizon, the effective lifetime for this period being reduced to 68,4 days. A signal would appear as an excess of neutrino events from the Sun position. No significant excess has been found, so that an upper limit on the neutrino flux has been set, as a function of the neutralino mass, and it is shown in figure 4.3.

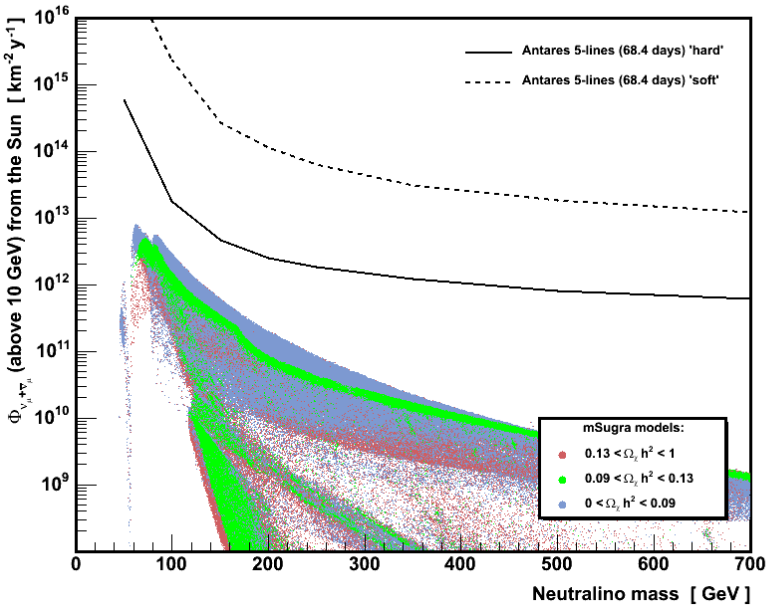

Figure 4.3. Upper limits to the neutrino flux from the Sun above $E_\nu = 10GeV$ for the sample of 2007 data, as function of the neutralino mass in the mSUGRA scenario. Pure annihilation into vector-bosons and into $b\bar{b}$ quarks, are referred to as *hard* and *soft* annihilation models respectively [94].

4.5 Neutrino Oscillations

The oscillation parameters which are relevant for atmospheric neutrinos are the mass splitting Δm^2_{23} and mixing angle θ_{23}.
As predicted in formula 1.8 atmospheric neutrinos with energies about 30 GeV have the maximum probability to oscillate after they have traveled for about 10^4 km, the size of the Earth. Therefore we do expect a strong reduction of vertical upgoing atmospheric muon neutrinos with less than 100 GeV energies. To detect such a signal, a reconstruction method with different characteristics with respect to the ones needed for other analysis tasks have been developed. It includes high event purity (good rejection of atmospheric muons), reliable determination of the muon zenith angle, muon energy estimation, event classification according to containment conditions. No azimuth angle determination is needed due to the symmetry of the problem.
Most of these conditions are already fulfilled by the *Online* reconstruction algorithm, described in chapter 5.
The oscillation parameters can be extrapolated by the fit of the oscillation hypothesis to the observed behavior of the data set (figure 4.4).

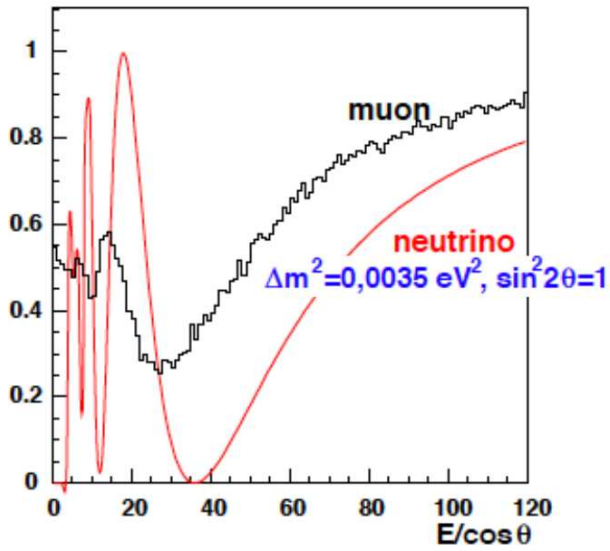

Figure 4.4. Oscillation probability as a function of the quantity $E/cos\theta$, for muon neutrinos and the reconstructed muons.

4.6 Search for exotic particles

Besides the detection of high energy neutrinos, the ANTARES telescope offers an opportunity to improve the sensitivity to exotic cosmological relics, in particular relativistic magnetic monopoles and slow nuclearites [103].

4.6.1 Magnetic monopoles

Magnetic monopoles were first introduced by Dirac, in 1931, to explain the quantization of the electric charge. Grand Unified Theories (GUT) predict the existence of stable supermassive monopoles with masses of $10^{17} GeV/c^2$, that originated in early Universe.
They could be present in the penetrating cosmic radiation traveling with low velocities, $10^{-4}c \div 10^{-2}c$, though in the presence of strong magnetic fields, they may reach higher velocities. Possible intermediate mass magnetic monopoles could achieve relativistic velocities, with masses lighter than 10^{15} GeV.
These particles carry magnetic charge, given by a multiple integer of the quantity $g_D = \frac{\hbar c}{2e}$, where $\hbar$ is the Planck constant, e is the elementary electric charge and c is the speed of light in vacuum.
Since fast monopoles have a large interaction with matter, they can generally loose a large amount of energy while traversing the Earth. Since they are accelerated in the galactic magnetic field, some particles could be able to traverse the Earth and propagate through the ANTARES detector as upward going particles.
A magnetic monopole propagating through the detector would emit a huge amount of light, with respect to atmospheric muons or muons induced by atmospheric neutrinos. The large amount of induced hits in the detector is used as a criteria to remove part of the atmospheric background, as shown in figure 4.5. This quantity has been used to optimize the sensitivity of the search.
The observation of magnetic monopoles requires the application of dedicated trigger algorithms, that are sensitive to particle velocities down to 0.5 c.
A dedicated Monte Carlo simulation has been developed within the Collaboration. First analysis and sensitivity studies have been performed using the standard cluster trigger and the standard *Full Likelihood* algorithm, described in chapter 5.
A preselection based on the number of triggers leads to a preliminary estimate of the 90% C.L. sensitivity for ANTARES, after one year of data taking, of the order of $\sim 10^{-17} cm^{-2} s^{-1} sr^{-1}$.

4.6.2 Nuclearites

Strange quark matter (SQM), made of u, d and s quarks in nearly equal parts, is expected to be the ground state of quantum chromodynamics.
Nuclearites are *nuggets* of SQM, that originated in the early Universe or in violent astrophysical processes, that could be present in the cosmic radiation.
Down-going nuclearites, with masses larger than 10^{10} GeV, could reach the ANTARES detector with velocities ~ 300 km/s. Nuclearites are thought to be electrically neutral, the small positive charge of the quark core being neutralized by the electrons forming a cloud in equilibrium inside the core. The relevant energy loss mechanism is represented by the elastic collisions with the atoms of the traversed media.
These particles could be detected by the black body light emitted by their overheated path in water. The typical duration of a nuclearites event in ANTARES would be of the order of milliseconds, the typical crossing time for such objects. Figure 4.6 shows the typical event duration for data, simulated atmospheric muons and simulated nuclearites.
The sensitivity of the ANTARES detector in 5-line configuration after 84 days of

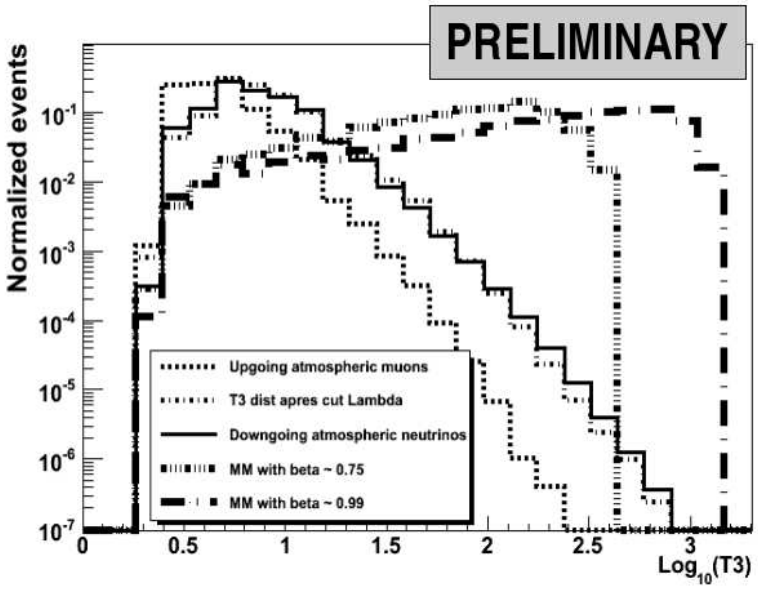

Figure 4.5. Normalized events as a function of the number of trigger clusters for down-going atmospheric muons, up-going and down-going atmospheric neutrinos, and up-going magnetic monopoles with $\beta \sim 0.75$ and $\beta \sim 0.99$ [103].

data taking to nuclearite events with masses heavier than 10^{17} GeV have been estimated to be of the order of $10^{-16} cm^{-2} s^{-1} sr^{-1}$.
Dedicated trigger logics for the detection of exotic particles are under development within the Collaboration.

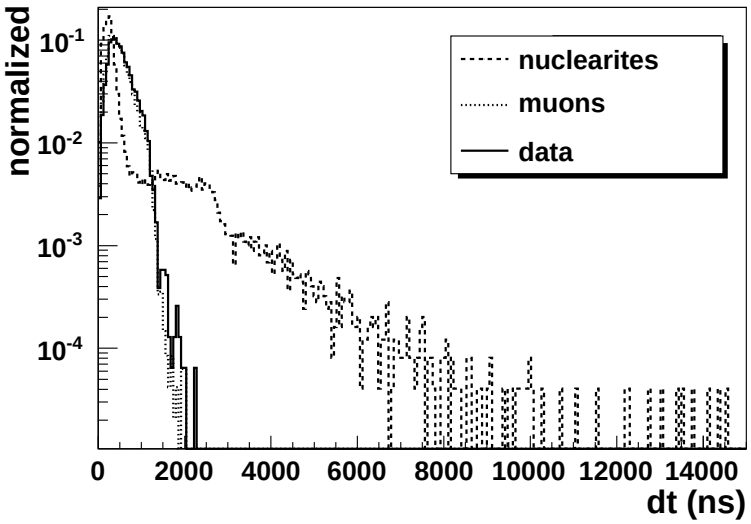

Figure 4.6. Normalized distributions as a function of the duration of snapshot. Comparison between data (continuous line), simulated muon (dotted line) and nuclearite (dashed line) events is shown [103].

4.7 Survey of a selected sky region

The analysis presented in this thesis does not have any *a priori* target, concerning the type of the source.
A neutrino telescope observes with a high duty cycle the whole sky that is below the horizon, each region of the sky with different exposures, as shown in figure 2.9. We study the distribution of the reconstructed neutrino events over several equally extended areas in the sky, searching for uniformity or excesses.
A region of the sky is selected, referred to as *ON region*. Several *OFF regions*, of equal area, exposure and detection rate, are also selected, so that we have an accurate estimate of the atmospheric background. We assume that, for construction, this background characterizes also the *ON region*. Comparing the number of events found in the ON and OFF regions we search for excesses of signal over the background. In case no significant excess of signal is found, an upper limit to the neutrino flux from the ON region can be set.
This analysis can be used to investigate any region of the sky: in the case of the present thesis work, we have focused our attention to a region that contains part of the super galactic plane, close to the Centaurus A nearby active galaxy, as will be discussed in chapter 6.

Chapter 5

Simulation and reconstruction of muon tracks in ANTARES

This chapter is devoted to an overview of the simulation tools and reconstruction algorithms that are used within the ANTARES Collaboration.
In the first part the software used for the simulation of the processes leading to a detectable signal in the detector and the detector response will be described. Monte Carlo (MC) simulations of neutrino and cosmic ray interactions, propagation of the secondary particles and random background will be discussed as well. The simulation of the data-acquisition system of the ANTARES detector will be also shortly reported. These simulations are necessary to understand the detector response and to validate analysis techniques and to evaluate the background contribution to the sample of reconstructed *neutrino* events. A wide description of the two main *strategies* that are used within the Collaboration to reconstruct the muon tracks propagating through the detector will be given in the second part of the chapter.

5.1 Monte Carlo simulation

Two physics processes can produce muon tracks and thus detectable Čerenkov light in the apparatus: muons and muon bundles from cosmic ray interactions in the atmosphere, as well as neutrino interactions in the vicinity of the detector. Here below the simulation of these processes, along with the simulation of the detector response, will be described in the following.

5.1.1 Neutrino generation

For the study of ν_μ induced events we simulated the atmospheric neutrino flux according to the Bartol model [14], and the neutrino interactions using an event kinematics simulation code developed within the ANTARES Collaboration [36]. The code generates muon neutrinos both within and on the surface of a *can*, defined as a cylinder around the detector, with size large enough that the Čerenkov light emitted outside its volume has a negligible probability to reach any PMT. In particular, the cylinder size extends beyond the instrumented volume by about 2.5 times the blue light absorption length, as in figure 5.1. Muon neutrinos can interact via charged

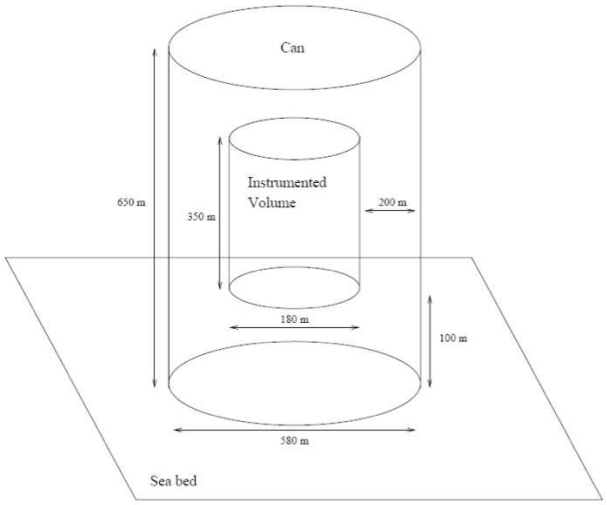

Figure 5.1. Schematic view of the ANTARES can. The can extends about two and an half absorption lengths, both in radius and in vertical length, over the instrumented volume.

current weak interaction (CC) inside and in the vicinity of the detector, producing detectable muons.
Interacting neutrinos are generated with a power law spectrum $E_\nu^{-\Gamma}$, where Γ is a generic spectral index, usually set to 1.4. In order to reproduce the desired spectrum (atmospheric neutrinos or astrophysical neutrinos) these events are weighted at the final analysis level step. Atmospheric neutrinos direction is generated with an isotropic distribution while, for point-like or extended sources simulations, the direction of the incident neutrinos is generated taking into account the location of the ANTARES detector and the effect produced by the Earth rotation.
Once the interacting neutrino is generated, with a neutrino energy E_ν, direction (θ_ν, ϕ_ν), interaction vertex (x, y, z) and an event weight W_{event}, the code simulates the neutrino CC interaction. Neutrino interactions are simulated with LEPTO[82] code, for the deep inelastic scattering, and with the RSQ code for the resonant and quasi-elastic scattering. The lowest simulated neutrino energy is 100 GeV, because of the poor detection efficiency at lower energies. This Monte Carlo generator integrates the differential cross sections and provides the kinematic properties of the outgoing muon. The hadronization of the nuclear fragments is done with PYTHIA 5.7 and JETSET 7.4[115]. The CTEQ3D parton distribution functions are used.
In the generation procedure a weight W_{event} is assigned to each event, in order to normalize the number of generated events to the desired neutrino flux. The event weight is calculated multiplying the expected neutrino spectrum, times the generation weight W_{gen}:

$$W_{event} = W_{gen} \cdot \left(\frac{dn_\nu}{d\epsilon_\nu dS dt}\right)^{expected} \tag{5.1}$$

W_{gen} is defined as the inverse of the simulated neutrino spectrum. In the case of a diffuse neutrino flux, it is given by:

$$W_{gen}^{-1} = \frac{E_\nu^{-\Gamma}}{I_E I_\theta} \cdot \frac{N_{total}}{t_{gen} V_{gen}} \cdot \frac{1}{\sigma_{CC}(E_\nu)\rho N_A P_{Earth}(E_\nu, \theta_\nu)} \tag{5.2}$$

where Γ is the generation spectral index, I_E is the integral of the generation spectrum shape E_ν^Γ over the whole simulated neutrino energy range, I_θ is the integral of the solid angle in which events are generated. N_{total} is the number of simulated events and t_{gen} is the event generation time. The neutrino interaction vertices are randomly generated within the volume V_{gen} that completely surrounds the detector sensitive volume. The term $(\sigma_{CC}(E_\nu)\rho N_A)^{-1}$ is the neutrino CC interaction length in a medium of density ρ, σ_{CC} is the CC neutrino interaction cross section and N_A is the Avogadro's number. The transmission probability through the Earth is also taken into account in the term $P_{Earth}(\epsilon_\nu, \theta_\nu)$, that is a function of the neutrino energy and direction.
In case neutrino emission from a point-like source is simulated, the term I_θ does not appear in the expression above.
The most frequent neutrino signals in the Antares detector are due to atmospheric neutrinos. This flux consists of a part due to decay of pions and kaons produced in cosmic ray interactions, together with a contribution due to the decay of charmed mesons. These prompt neutrinos dominate the atmospheric neutrino flux at energies above 10^5 GeV. Both conventional and prompt neutrino fluxes can be simulated.

5.1.2 Muon generation

ANTARES uses two different MC physics generators to simulate the flux of atmospheric muons crossing the detector volume. The first one is a full Monte Carlo based on Corsika[1] [77], a program for detailed simulation of extensive air showers initiated by high energy cosmic ray particles. The second one, MUPAGE, uses the results of a full MC simulation (HEMAS [112]) that, from the flux of primary cosmic rays defines the flux of muons (and muon bundles) at the sea surface and, by means of parametric formulas estimates the underwater muon flux at the detector depth [42]. The HEMAS results have been validated by results obtained by the MACRO Collaboration[28].
The full simulation has to be performed choosing a simple $E^{-\gamma}$ primary flux spectrum for all nuclei. It is then possible to re-weight events with any other user preferred flux model.
Using MUPAGE the primary CR composition is fixed[68] so that the events do not need to be weighted.
In the following the two generator programs are briefly described.

Full Simulation

The full muon MC simulation[77] is based on Corsika v.6.2. It starts with the simulation of the primary cosmic rays interactions with the atmospheric nuclei, and the production of secondary particles and their propagation in the atmosphere. The

[1] COsmic Ray SImulations for KAscade

primary cosmic rays are originated inside the zenith range $0° \div 85°$ and with an energy range per nucleon from 1 TeV to 100 PeV. The QGSJET package[47] is used as generator of the development of hadronic interactions.
Muon propagation through water is performed with the MUSIC [2] program[32].
MUSIC takes into account energy losses due to bremsstrahlung, pair production, inelastic scattering and ionization. It simulates also the angular and lateral deflections due to multiple scattering.
Several models can be used to describe the flux and the relative abundances of different elements, leading to an accurate reproduction of the spectra observed at Earth, up to high energies. Two models are mainly considered for the flux of primary CRs: the *poly-gonato*[80] and the NSU model[101, 53].
The first one, by J.E. Hoerandel, is a phenomenological model, based on experimental data taken with satellites and balloon experiments, so that the primary flux up to 10^{15} eV is measured directly outside the Earth atmosphere, before the primary particles interact with air molecules, producing extensive air showers (EAS).
An extrapolation up to energies of the order of 10^{18} eV is based on the EAS measurements.
The NSU model, proposed by Bugaev *et al*, is based on the results of experiments measuring EAS induced by primary CRs of energies between 10^{12} and 10^{17} eV.
A comparison between the *poly-gonato*, the NSU and the HEMAS (used in MUPAGE) primary flux models is shown in figure5.2.

Parametric Simulation

MUPAGE[56] generates atmospheric muon events, also in bundles, at the level of the can. It is based on a parametrization of the atmospheric muon flux [42] at the depth of the detector. The model used for the hadronic interaction is DPMJET[109]. As MUPAGE generates events according to their abundance, no weighting of the events is needed. Each set of events corresponds to a certain observation time.
The main advantage of the parametrized simulation is the computational speed, much faster than that of the full simulation: e.g. the generation of a data set with a lifetime equivalent to one month requires about 300 hours of CPU time on a 2xIntel Xeon Quad Core, 2.33 GHz with MUPAGE.

5.1.3 Photon generation

The propagation of muons and the associated production of Čerenkov light is simulated using the KM3[37, 35] software. In order to reduce the computing time, the amount of light generated by a muon of a given energy has been simulated with GEANT3, parametrized and stored in tables, also containing the information on the light emitted by secondary particles. These tables are used to get the hit probability along the muon path in water.
The KM3 software also simulates the OM response according to its characteristics obtained from experimental measurements [30, 16].
Once the photons reaching the photocatode and the corresponding number of photoelectrons have been simulated, the next step is the simulation of the environmental

[2] MUon SImulation Code

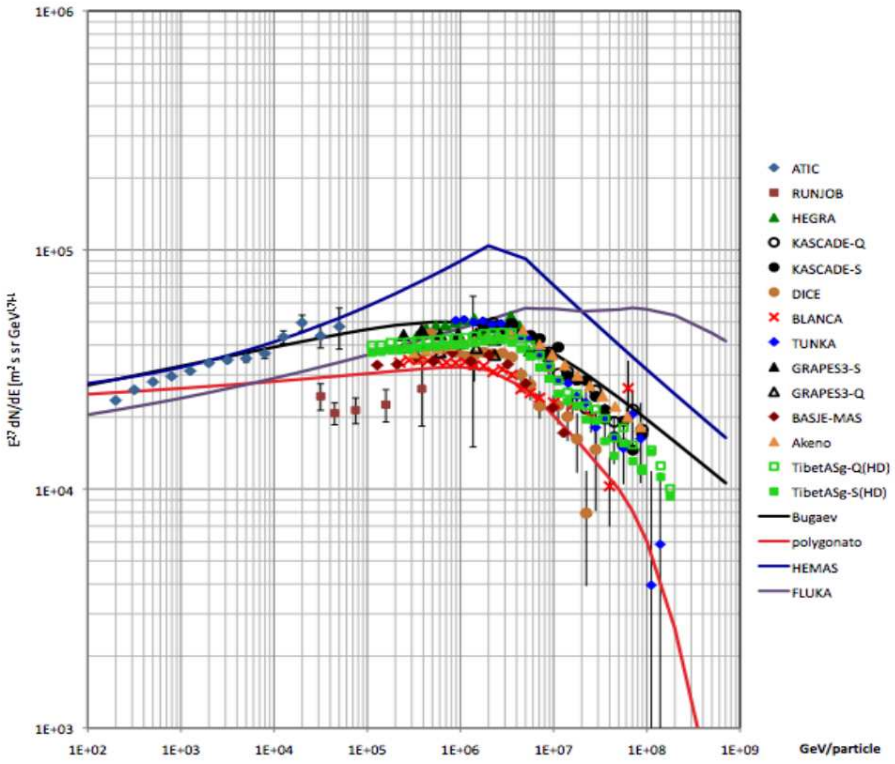

Figure 5.2. The all-particle spectrum deduced by direct and indirect measurements and the parameterizations used in MC simulations [58].

background and of the ANTARES DAQ system.

5.1.4 Background simulation

As discussed in chapter 3, the environmental background in the ANTARES experiment is due to decay of radioactive isotopes, that are present in sea water, and to bioluminescence. The radioactive decay can be simulated in a straightforward way as the decay rate can safely be assumed constant. The bioluminescence, however, results in rather erratic behavior of the PMT count rate. The single rates observed *in situ* can be applied to simulated data with a dedicated software, called *SummaryTimeSliceWriter*. The program takes the single rates of the PMTs located on an ANTARES line, as measured in a given detector run, and generates the count rates of all PMTs in the considered geometry. The output of the *SummaryTimeSliceWriter* program is then merged to the MC data with a dedicated code.

5.1.5 Trigger simulation

The *TriggerEfficiency* (TE) program can be used to process the MC data through the ANTARES software trigger: any of the trigger algorithms which are used in the DAQ system can be applied to the simulated data. TE simulates the ARS electronics, merges the background (from *SummaryTimeSliceWriter*) to the MC data

and finally processes the data through the ANTARES software trigger (simultaneous triggers can be chosen). In order to do that, the ascii output of KM3 must be previously converted in ROOT format by the *MonteCarloEventWriter* program.
The MC data are triggered in the same manner as the real ones.
The data with a charge greater than a certain threshold (typically 0.3 pe) are called level 0 (L0) hits. The first level trigger, referred to as L1 trigger, is built up of coincidence hits in the same storey within a 20 ns time window, and optionally selecting hits with a charge larger than a *high threshold* tunable from 2.5 pe to 10 pe. A trigger logic algorithm, which behaves like a second level trigger, is then applied to data and operates on L1 hits. The generated output of TE has the same characteristics of the real raw data, as is represented in the schematic diagram in figure 5.3.

5.1.6 Simulation used in this analysis

The analysis that will be presented in chapter 6 has been performed using data collected by ANTARES during 2007. The active lifetime for that period was 245 days, reduced to 168 days excluding from the data sample periods characterized by high environmental background. During the selected period, two different *high threshold* values (10 p.e. and 3 p.e.) have been used, so that two full MC simulations have been performed. Table 5.1 summarize the specific features of the two detection periods.

Table 5.1. Specific features of the two data taking periods in 2007.

Trigger	Active time (days)
3N, 10 p.e.	47.2
3N, 3 p.e.	120.5

5.2 Muon tracks reconstruction

Neutrino astronomy aims at the identification of astrophysical sources of high energy particles: this is possible, especially for ν_μ, since at energies higher than about 1 TeV, the neutrino arrival direction is within 1° from that of the charged lepton produced in the final state of a CC interaction with the traversed medium.
By kinematics the angle between the neutrino direction and the out-coming charged lepton track decreases as a function of the increasing neutrino energy, as in figure 5.4.
The identification of the charged lepton track, especially for muons, can be performed using the information about position, time and signal amplitude of the hit PMTs.
In this section I will describe the reconstruction of muon tracks; algorithms for the identification of electron and τ-induced showers have also been developed within the ANTARES Collaboration [76] but they will not be discussed here.
The reconstruction of a muon track can be generalized to the problem of estimating a set of unknown parameters $\mathbf{\{a\}}$, given a set of experimentally measured physical

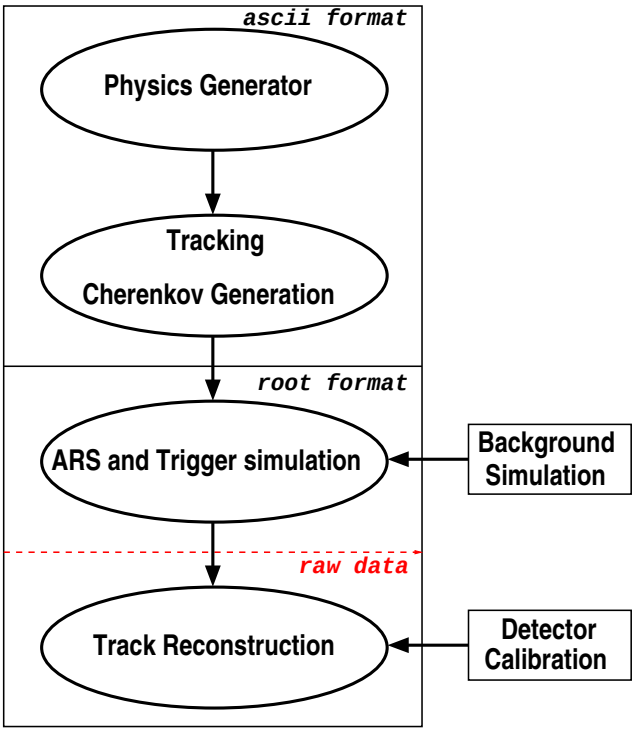

Figure 5.3. Scheme of the general MonteCarlo production chain. After the trigger program, the simulated data are in the same form as the real raw data.

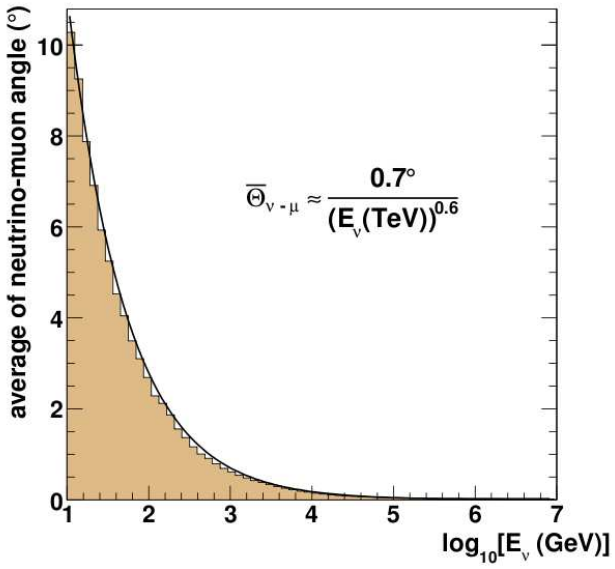

Figure 5.4. Median angular difference between the parent neutrino direction and the outcoming muon track. The solid line shows the functional form, while the histogram indicates the Monte Carlo predictions.

quantities $\{\mathbf{x}\}$, that for ANTARES are the time, the position and the hits amplitude.

The muon trajectory can be parametrized using the direction $\hat{d} = (d_x, d_y, d_z)$ and the position $\vec{p} = (p_x, p_y, p_z)$ of the muon at a fixed time t_0. The problem of the reconstruction of a track has 5 independent parameters: three values are needed to fix $\vec{p}$ at a given time, and two angles define the direction $\hat{d}$, that can be expressed

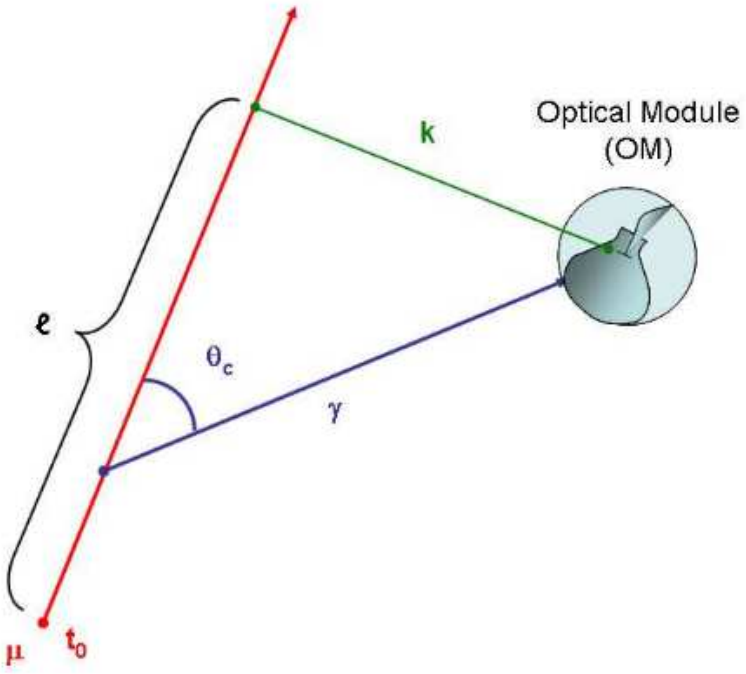

Figure 5.5. Schematic description of the relation between the muon trajectory and the OM. The line labelled as γ indicates the distance between the point of emission of the Čerenkov photon along the muon track and the OM containing the PMT.

in terms of the director cosines and can be given as a function of the azimuth ϕ and zenith angle θ, that is $\hat{d} = (sin\theta cos\phi, sin\theta sin\phi, cos\theta)$. The time t_{exp} at which a Čerenkov photon, produced at an arbitrary time t_0 along the track of a relativistic muon propagating in water, is expected to reach a PMT is given by:

$$t^{exp} = t_0 + \frac{1}{c}(l - \frac{k}{tan\theta_C}) + \frac{1}{v}(\frac{k}{sin\theta_C}) \tag{5.3}$$

where k is the minimum distance between the muon track and the OM, and l indicates the muon path in water, as in figure 5.5.
The Čerenkov angle is indicated by θ_C and v is the group velocity of light in water. The term $\frac{1}{c}(l - \frac{k}{tan\theta_C})$ in equation 5.3 accounts for the time it takes for the relativistic muon to reach the point at which the photon is emitted, while the term $\frac{1}{v}(\frac{k}{sin\theta_C})$ accounts for the light propagation from the muon track to the OM.
The difference between the expected and the measured arrival time of the Čerenkov photons on the PMTs gives the time residuals:

$$r_i = t^{exp} - t_i \tag{5.4}$$

In the ideal case the distribution of the time residuals for the hits due to the Čerenkov photons would be very narrow. Taking into account realistic experimental

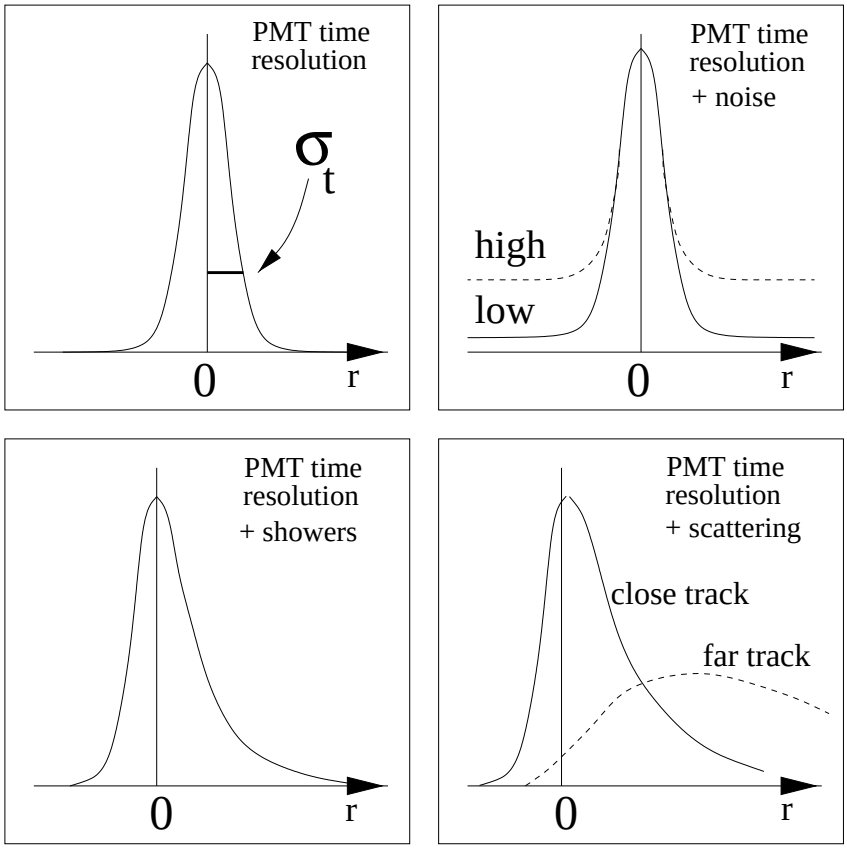

Figure 5.6. Schematic distribution of the time residuals, showing different experimental effects that lead to the observed asymmetrical shape. Top left: Broadening due to PMT time resolution; Top Right: combined effect of PMT time resolution and of environmental background; Bottom left: Combined effect of PMT time resolution and light emitted in showers; Bottom right: Combined effect of PMT time resolution and light scattering [27].

conditions, the distribution is broadened and distorted by several effects, schematically described in figure 5.6.
The time resolution of the PMTs causes a broadening of the distribution, as described in section 3.4. Photons that are scattered by water molecules or sediments or that are emitted by secondary particles, e.g. electromagnetic showers produced along the muon trajectory, arrive on the photocatode later than the Čerenkov photons, giving raise to positive time residuals. Finally, background hits, due to bioluminescence and ^{40}K, are not causally related with hits due to propagation of the track in the detector: they give raise to both early and delayed random hits, showing a flat distribution of the residuals. Several algorithms have been developed and are in use within the ANTARES Collaboration, in order to identify the arrival direction of neutrino-induced muons.
Two of them will be described in the following sections: they will be referred to as *Full likelihood* and *Online* algorithms.

5.3 Full Likelihood Algorithm

This method [78] is based on a likelihood fit that uses a detailed parametrization, derived from simulations, for the Probability Density Function (PDF) of the arrival times of the hits, taking into account both the environmental background and the emission of Čerenkov photons by secondary particles or showers.
It was found that this likelihood fit is only successful if the maximization procedure is performed after a preliminary evaluation of the track parameters.
To obtain this preliminary solutions, the reconstruction algorithm is made of several steps: the full likelihood fit is performed after a series of *prefit* algorithms, combined with the application of hit selection criteria.
We define as *likelihood value* of a reconstructed event the probability that the track, characterized by the set of $\vec{p}$ and $\hat{d}$ resulting from the fit, has been produced by a muon propagating trough the detector. In the *Full likelihood* algorithm, the likelihood is a function of the residuals r. Under the hypothesis that hits composing an event are independent, the likelihood for a given event can be written as:

$$L = P(event|track) = P(hits|\vec{p},\hat{d}) = \prod_{i=1}^{Nhits} P(r_i|a_i,b_i,A_i) \tag{5.5}$$

where r_i is the time residual, A_i is the hit amplitude (in pe), a_i indicates the cosine of the incidence angle of the photon on the OM, and b_i is the length of the photon path corresponding to the hit i, as in formula 5.3.

5.3.1 Linear prefit - step 0

Hits fulfilling criteria dictated by causality are then required to be in local coincidence or to have and amplitude larger than a certain threshold. Those hits are used to minimize a χ^2 expression, that produces an initial track on the basis of the hit times with an amplitude weight. This approach ignores the geometry of the Čerenkov cone and the optical properties of the medium, and assumes light traveling with a velocity $\vec{v}$ along a 1-dimensional path through the detector. The locations of each PMT, $\vec{x}_i$, which have been hit at a time t_i are considered as connected by a line:$\vec{x}_i \simeq \vec{x} - \vec{v}t_i$. The χ^2 expression to be minimized is the following:

$$\chi^2 = \sum_{i=1}^{Nhits} A_i(\vec{x}_i - \vec{x} - \vec{v}t_i)^2 \tag{5.6}$$

where A_i is the signal amplitude of the hit i, detected at time t_i at the position $\vec{x}_i$. The factor A_i accounts for the fact that hits closer to the track will have a higher amplitude.
This linear prefit is based on the assumption that, considering the relevant energy range for the experiment (E $\simeq$ 100 GeV $\div$ 10 PeV), muon tracks are infinitely long if compared to the distance between an OM and the track: the hit PMTs are considered to lie on the track itself.
The χ^2 is minimized by differentiation with respect to the free parameters $\vec{x}$ and $\vec{v}$: the 5 tracks parameters can be thus obtained with simple geometrical relations.

5.3.2 M-estimator - step 1

M-estimators constitute a broad class of statistical estimators, that are used to maximize a given function g, that in our case is a function of the residuals r. M-estimators are used for the so-called *robust estimation* [81], i.e. a method insensitive to large fluctuations in a small number of data points. By choosing an M-estimator that behaves in an appropriate way for large residuals, it can be expected that a reasonable track estimate can be obtained without the requirement of an accurate starting point. The result of the M-estimator is not heavily influenced by the choice of the starting value, this is the reason why this method has been used as a *natural* step following after the liner prefit. The use of an M-estimator for the determination of the track parameters gives results which are already very good, allowing the fit to converge to solutions that are very close to the simulated ones.
Before the use of the M-estimator, a new selection is applied to the hits that have *survived* the previous step. After the second hit selection, the minimization of the following function is performed [105]:

$$G = \sum_{i=1} k(-2\sqrt{1 + A_i r_i^2/2}) - (1-k) f_{ang}(a_i) \tag{5.7}$$

where A_i indicates the charge (in pe) of the hit i, a_i indicates the angle of incidence of the photon on the OM, f_{ang} is the angular response function of the OM. The value of the relative weight $k = 0.05$ has been optimized by means of a full detector Monte Carlo simulation.

5.3.3 Maximum likelihood fit - step 2

In the simplest case, the likelihood described in formula 5.5 can be considered as a function of the time residuals only. The dependence on the parameters a_i, b_i and A_i can be neglected, and the likelihood takes the form:

$$L = P(event|track) = \prod_{i=1}^{Nhits} P(t_i|t_i^{th}) \tag{5.8}$$

In this case the Probability Density Function (PDF), to observe a certain value of time residual is shown in figure 5.7 as a function of r. The parameters that maximize the simplified likelihood are kept as the best track parameters.
It was found that the efficiency of the algorithm is enhanced by repeating the last two steps several times. Starting from the track obtained in the prefit, indicated with $\hat{d}$ in the following, these further steps are performed:

- A Cartesian system is chosen, such that the $\hat{z}$ axis is upward oriented.
- The hits *center of gravity* is identified, defined as $C = \frac{\sum_i^{Nhits} \vec{x}_i a_i}{\sum_i a_i}$, where $\vec{x}_i$ indicate the coordinates of the hit PMTs and a_i the corresponding hit amplitudes.
- Two tracks are obtained by translating the pre-reconstructed track along the direction defined as $\hat{d} \times \hat{z}$.

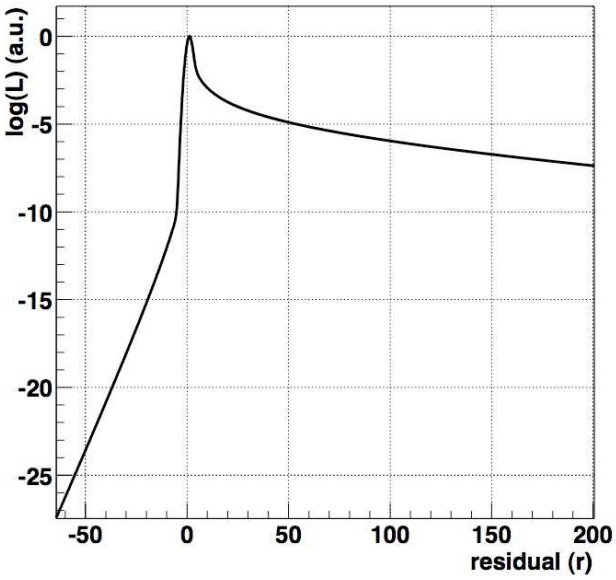

Figure 5.7. Simplified PDF as a function of r, the hit time residuals, from [78].

- Two tracks are obtained by a translation along the direction identified by the $\hat{z}$ axis.
- Four additional starting points for the maximization procedure are obtained by rotating the prefit track. The origin of the rotation is the point on the track that is closest to the center of gravity of the hits.

The *best track*, i.e. the one that maximizes the likelihood, is taken and the expected arrival times are compared to those expected from the improved PDF, as described in the next section. Moreover, results that are reconstructed within 1° from the best track are considered as *compatible* with the best one: the total number of these solutions is indicated with N_{comp}, and is used to evaluate the quality of the result obtained.

5.3.4 Maximum likelihood fit with improved PDF - step 3

The simplified version of the PDF does not take into account the background hits. This approximation can give raise to a worsening in the track reconstruction performance since background hits are not accurately treated. The last reconstruction step is preceded by a last hit filtering which eliminates hits with large time residuals. Hits are selected according to their time residuals and amplitude or in case they are found to be in local coincidences. The best results obtained from the previous maximum likelihood procedure is used as a starting point for the maximization of a likelihood with an improved version of the PDF.
The PDF used at this step has contributions from both signal and background hits:

$$P(r_i|a_i,b_i,A_i) = \frac{1}{N^T(a_i,b_i,A_i)}[P^{sig}(r_i|A_i)N^{sig}(a_i,b_i,A_i) + R^b(A_i)] \qquad (5.9)$$

where $N^{sig}(a_i, b_i, A_i)$ is the number of signal hits and $R^b(A_i)$ is the background rate for hits with amplitude A_i. The total number of hits of amplitude A_i is given by $N^T(a_i, b_i, A_i) = N^{sig}(a_i, b_i, A_i) + R^b(A_i)T$, where T indicates the event duration.

5.3.5 Performance

The performances of each step of the reconstruction algorithm have been evaluated using a sample of simulated atmospheric neutrino-induced muon events in the full detector. The quantity that is used to quantify the reconstruction error is the angle between the reconstructed track and the true muon direction, indicated with α. The distribution of $log_{10}(\alpha)$ for Monte Carlo atmospheric neutrinos is shown in figure 5.8, for each of the four reconstruction steps described in the previous sections.

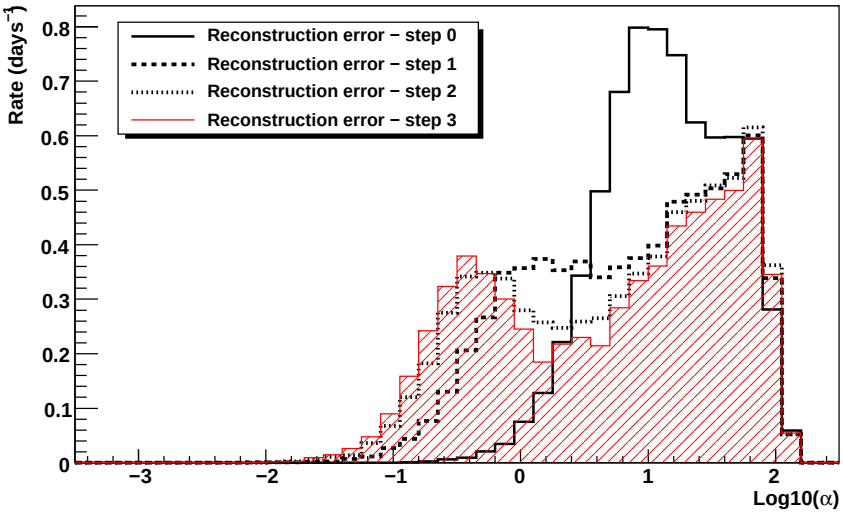

Figure 5.8. Reconstruction error, in degrees, of the *Full Likelihood* algorithm for selected simulated events (12 lines detector). The reconstruction error is shown for each of the four reconstruction steps described in the text. A full simulation of atmospheric neutrinos has been used. Only tracks reconstructed as up-going are shown.

5.3.6 Background rejection and selection criteria

The strategy we have described so far is such that a low number of events are rejected: the philosophy adopted is to reconstruct as many events as possible, even with large errors, and to reduce the number of badly reconstructed events by the application of selection criteria, that can be applied after the reconstruction procedure, depending on the peculiar target of the physical analysis.
In order to reject badly reconstructed muon tracks, the following quantity can be used:

$$\Lambda = \frac{log(L)}{N_{DOF}} + 0.1(N_{comp} - 1) \tag{5.10}$$

where the term $\frac{log(L)}{N_{DOF}}$ indicates the log-likelihood per degree of freedom and N_{comp} indicates the number of compatible solutions, as explained is section 5.3.3.

Figure 5.9 shows the distribution of Λ for simulated atmospheric neutrinos and muons, reconstructed with the *Full Likelihood* algorithm. Tracks reconstructed with a large (absolute) value of Λ are badly reconstructed. The reconstruction is usually worse for down-going atmospheric muons, since the detector is optimized for the detection of up-going particles: atmospheric muons can be efficiently rejected by means of an optimized cut in the parameter Λ.

Figure 5.10 shows the distribution of the reconstruction error for selected atmo-

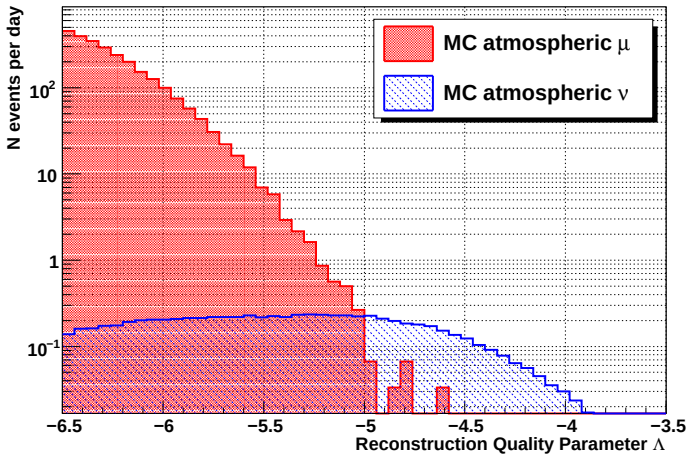

Figure 5.9. Distribution of the quantity Λ, used as a reconstruction quality parameter within the *Full Likelihood* algorithm. The plot shows selected Monte Carlo events of atmospheric neutrinos and atmospheric muons.

spheric neutrinos (Monte Carlo) events for the full ANTARES detector: the black curve indicates the outcome of the reconstruction algorithm, without quality cut. It can be seen that several events are reconstructed with a reconstruction error higher than 10°. The selection of the events by means of the quantity Λ has the effect of rejecting badly reconstructed events, at the price of a reduction in the total number of events, as can be seen in the blue, green and red curves, indicating the reconstruction error for different choices of the Λ cut value. The rejection of badly reconstructed events is accurate for high values of Λ.

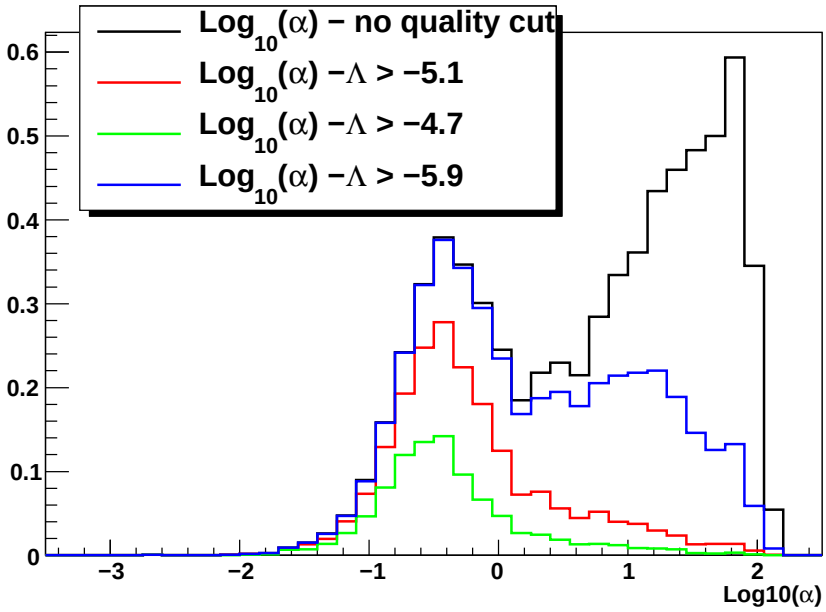

Figure 5.10. Reconstruction error for the *Full Likelihood* algorithm for selected simulated events. The effect of the cut in the variable Λ, used to reject badly reconstructed events, is visible in the red, blue and green curves, corresponding to different choices of Λ. A full simulation of atmospheric neutrinos has been used. Only tracks reconstructed as up-going are shown.

5.4 Online Algorithm

This approach, usually referred to as *BBFit*, has been initially developed as a fast reconstruction algorithm for the online monitoring of the triggered events [52].
An example of the online event display of the ANTARES detector is shown in figure 5.11. Besides its initial purpose, the algorithm has been found to show good performance in the reconstruction of muon tracks, as well as very good agreement between data and Monte Carlo events, as can be seen in figure 5.12, showing the distribution of the muon arrival directions, for data taken in 2008, together with Monte Carlo predictions.
Differently from the previous algorithm, the philosophy of this reconstruction strategy is to select a very high purity sample of signal hits. Hits surviving the purity selection are then used to perform a χ^2-like fit of the muon trajectory. In particular, only hits due to direct Čerenkov photons are selected, delayed hits due to scattering and biological activity are ignored in the fit.
The algorithm merges hits occurring on the same floor and uses the center of the triplets in the fit: this choice can produce a degradation in the angular resolution, but makes the algorithm independent on informations usually obtained from positioning devices that are integrated in the experiment itself.
The main concept used in this algorithm is the fact that both a detector line and a muon track can be considered as straight lines in space. For tracks that are not exactly vertical, the point of closest approach with respect to the detector line can

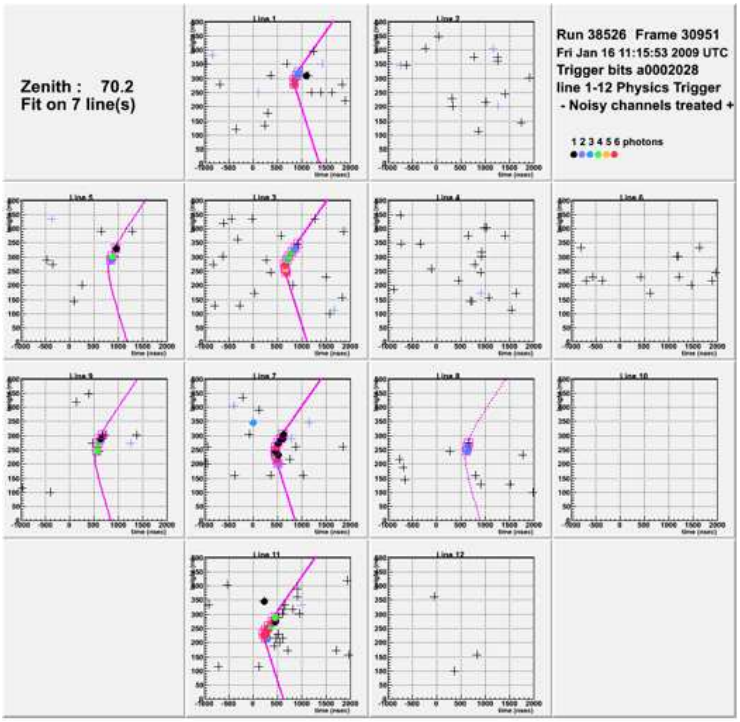

Figure 5.11. Online event display of the ANTARES detector. Each box shows depth versus time for each detector line: the event shown has been reconstructed using seven lines with the *Online Algorithm*.

be identified. Most of the Čerenkov light is expected to be detected in the vicinity of this point: this fact is used in the hit selection and in the fitting algorithm.

5.4.1 Hit Selection

The first step in the hit selection is the search for floors that collect coincidences within a time window of 20 ns.
The geometry of the three OMs located on each floor is ignored in the algorithm: hits closer than 20 ns are merged, and the time of the earlier hit is taken. Moreover the resulting hit amplitude has to exceed a given amplitude threshold.
Doublets of such floors are identified, allowing for no more than one empty floor in between, and requiring that the time difference of the hits is smaller than 80 ns per floor of separation. Only detector lines with at least one doublet are used in the fit, to avoid the attribution of isolated noise hits to a track.
Clusters of hits are then formed by iteratively complementing the doublets with adjacent hits that are close in time (within 80 ns per floor) and distance (no more than one empty floor) to the already identified cluster.
Only events with at least 5 (multiple) hits are considered for the fitting procedure.

5.4.2 Fit

The selected hits are used to minimize the following function, that is based on the χ^2 of time residuals r with an additional term, taking into account solutions characterized by hits with large amplitudes passing very close to the OM:

$$Q = \sum_{i=1}^{Nhits} \left(\frac{r_i^2}{\sigma^2} + \frac{a_i d_i}{\langle a \rangle d_0}\right) \tag{5.11}$$

where r_i is the time residual for the hit i, as defined in formula 5.4, a_i is the amplitude of the hit, d_i is the distance between the hit PMTs and the track.
The constant factor σ is set to 10 ns for signal amplitudes higher than 2.5 pe, and to 20 ns otherwise.
The second term has been parametrised so that it gives a penalty to the combination of high amplitude and large distances. The product is normalized to the average amplitude $\langle a \rangle$, to take into account high energy tracks or showers that would produce a much higher amount of light at the same distance. For events with hits detected on several detector lines, the track parameters are identified using the function Q. If the track is exactly vertical, the reconstruction of the track is a function of only

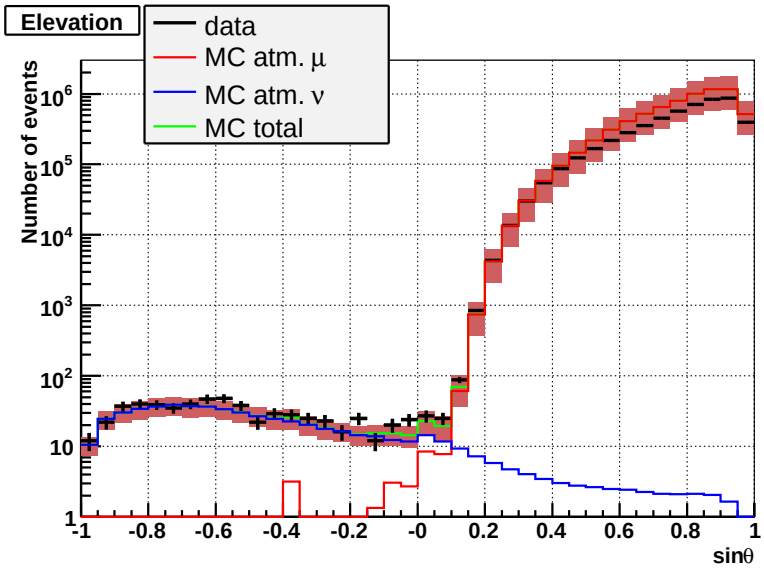

Figure 5.12. Distribution of the reconstructed muon arrival directions, sine of elevation, together with the Monte Carlo predictions. Events reconstructed with the multi-line fit in the Online reconstruction algorithm are shown, for data taken in 2008, with the 9-12 lines ANTARES detector.

four parameters, due to the symmetry around the vertical axis. An additional fit is performed using a *bright point* hypothesis, corresponding to a single flash of light at a given time. This model can be applied to the identification of noise sparks and of the light emitted by LED and laser beacons to perform *in-situ* time calibrations of the detector, as described in section 3.4.
Moreover, this model applies to light from hadronic and electromagnetic showers, that is often seen as a *point-like* light source in the detector. A comparison of the

quality of the two fits is used to reject events in which down-going muons create a bright electromagnetic shower that may mimic an up-going track.
It is worth noticing that the simplified structure of this algorithm, makes it an order of magnitude faster than the *Full Likelihood* algorithm.

5.4.3 Performance

Figure 5.13 indicates the reconstruction angle for the *Online* algorithm, by means of the quantity $log_{10}(\alpha)$, as defined in section 5.3.5. Only multiline events are shown, for both atmospheric muons and neutrinos. The true muon direction can be reproduced within 1° of precision, slightly better for atmospheric neutrinos than for atmospheric muons. Both curves are averaged over the full angular range and over the energy.

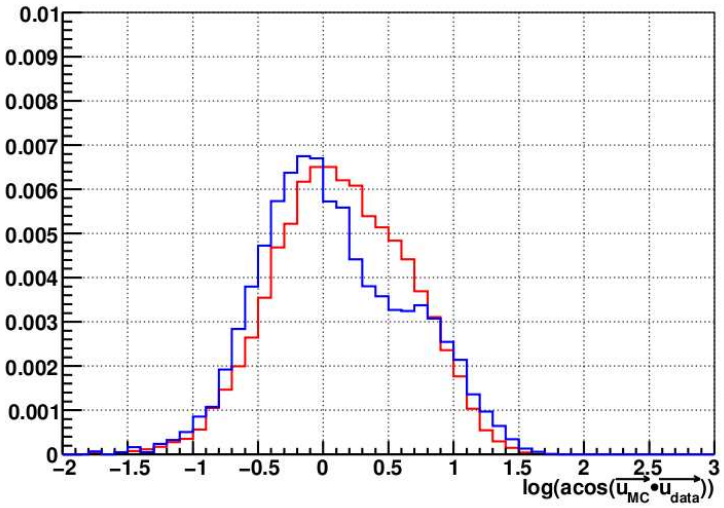

Figure 5.13. Reconstruction error of the *Online* algorithm for selected simulated events [50]. A full Monte Carlo of atmospheric neutrinos (in blue) and atmospheric muons (in red) has been used. Only tracks reconstructed using hits on more than 2 lines are shown.

5.4.4 Background rejection and selection criteria

The track fit quality is evaluated by means of the quantity Q/NDF. Figure 5.14 shows the distribution of Q/NDF for selected events: only tracks reconstructed as up-going in more than two detector lines are shown. The peak region ($0.5 < Q/NDF < 2$) corresponds to well reconstructed events, while the tail region corresponds to badly reconstructed events. Moreover a cut in the variable Q/NDF can efficiently reduce the background due to atmospheric muons.

5.5 Detector performance with the two algorithms

As discussed in section 3.7, the main quantities that are used to evaluate the detector performance are the effective area and the angular resolution. These quantities have

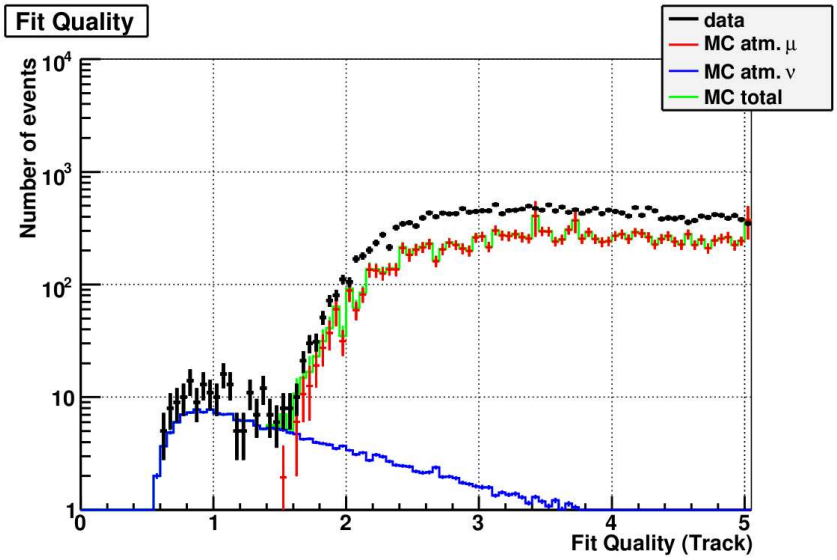

Figure 5.14. Distribution of the variable Q/NDF, used to evaluate the track fit quality of the *Online* algorithm [50]. The plot shows selected up-going events from both data and Monte Carlo simulations of the ANTARES detector. Only tracks reconstructed using hits on more than 2 lines are shown.

been evaluated, for the discussed reconstruction algorithms, from a full simulation reproducing the detector performance: the corresponding results are shown in the following.

As previously reported, the *Online* reconstruction algorithm has been developed as a fast *quasi*-online method, the information provided by the detector positioning system not being used. This algorithm is largely used in those physics analysis that do not require a precise pointing accuracy, e.g. the determination of neutrino oscillation parameters, as described in chapter 4.

The *Online* strategy provides reliable reconstruction of the muon track parameters, as shown in figures 5.12 and 5.13, but does not allow for a good pointing accuracy, as shown in the righ plot in figure 5.16.

The neutrino effective area for the *Online* algorithm, shown in the right plot in figure 5.15, is larger than the one obtained by the *Full Likelihood* algorithm (left plot in figure 5.15), especially for energies lower than some TeV.

On the other hand, the *Full Likelihood* algorithm has been specifically tuned to identify point-like neutrino sources. The expected angular resolution, shown in the left plot of figure 5.16, is better than 0.3° at energies higher than 10 TeV, adequate for the purpose of neutrino astronomy.

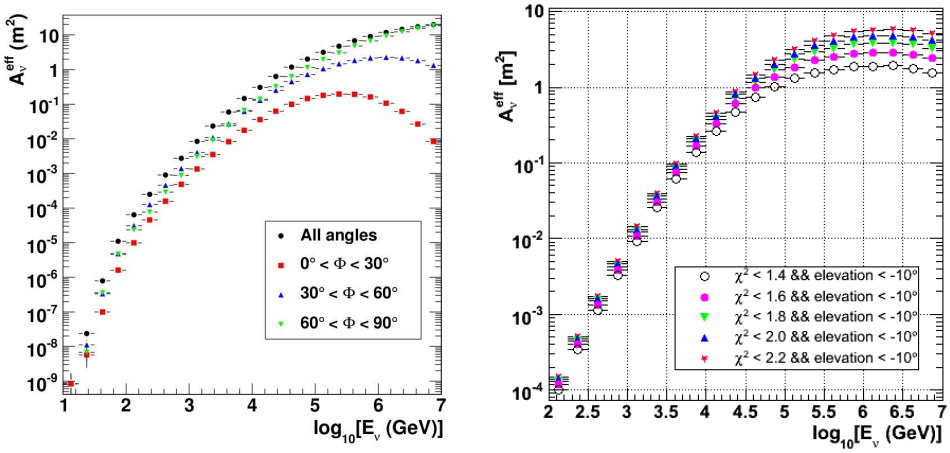

Figure 5.15. *Left*: the ANTARES neutrino effective area, obtained with the *Full Likelihood* algorithm, as a function of the neutrino energy. Different nadir (ϕ) angles show the Earth opacity at high energies. *Right*:the ANTARES neutrino effective area, obtained with the*Online* algorithm, as a function of the neutrino energy, for different cuts in the fit quality. Only events reconstructed as up-going are considered.

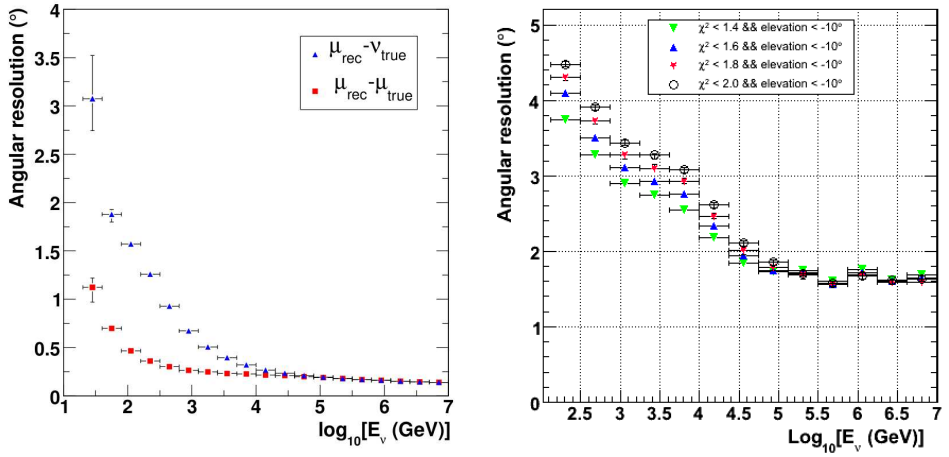

Figure 5.16. *Left*: the ANTARES angular resolution, obtained with the *Full Likelihood* algorithm, for muons (median of the distribution of the space angle between the true and the reconstructed direction of the simulated muon tracks) and for neutrinos (median of the distribution of the angle in space between of the neutrino arrival direction and the simulated muon track). It is noteworthy that the expected angular resolution is better than 0.3° at energies higher than 10 TeV. *Right*: angular resolution for the full ANTARES detector, obtained with the *Online* algorithm, as a function of neutrino energy for different cuts in the fit quality. Only events reconstructed as up-going are considered.

Chapter 6

Neutrinos from the super galactic plane

Recent observations by the Pierre Auger Observatory [5] indicate a possible correlation between the highest energy cosmic rays and the distribution of nearby AGN. Neutrino emission from these sources is predicted in several theoretical models: the target of the present analysis is the study of the distribution of the neutrino signal in a sky region that covers part of the supergalactic plane (SGP), where most of the extreme energy events recently detected lie.
The first section shows the most recent experimental results on the origin of the most energetic cosmic rays, along with an overview of possible theoretical interpretations. The second section contains a short description of the predicted neutrino fluxes from the same sources that are likely to accelerate cosmic rays. In the third section the results of the present work will be described. Data from the ANTARES detector, taken during 2007 when the detector was only composed by five lines, have been analyzed.

6.1 The origin of the most energetic cosmic rays

The origin of the most energetic cosmic rays (E $> 2\times 10^{19}$ eV) is still not understood. Stochastic shock acceleration theory [70] suggests that they should originate in sources which are also VHE γ-rays emitters. While the existence of very high energy γ-ray sources have been proven, no point sources of ultra high energy cosmic rays (UHECRs) or neutrinos have been detected so far. The main reasons why cosmic rays sources have not yet been identified is the fact that these particles, being mainly charged nuclei or protons, are deflected by magnetic fields and their acceleration sites cannot be identified by means of the observations on the Earth. A charged particle of charge Ze and energy E, propagating in a region where a magnetic field B is present, moves along a curved trajectory whose gyroradius R is given by:

$$R = \frac{E}{ZeB} \tag{6.1}$$

Charged particles produced inside our Galaxy remain confined if their gyroradius is smaller than the linear dimensions of the Galaxy (up to E $\simeq 10^{15} \div 10^{16}$ eV),

otherwise magnetic confinement becomes impossible. For this reason it has been suggested that UHECRs might be produced in extra-galactic sources.
Most likely accelerators of these extremely energetic particles are radio galaxies [45, 106], clusters of radio galaxies [125] or, in a more exotic scenario, topological defects [114]. GRBs are also very likely to produce charged particles of extreme energy as well as neutrinos, but given their transient nature, these sources will not be considered in the present analysis.
The arrival directions of cosmic rays observed at Earth, with energies up to hundreds of PeVs, show isotropic distribution, their path from the source to Earth being bent by magnetic fields. At sufficiently high energies the magnetic deviation of the path of charged particles becomes sufficiently small, so that the arrival direction of the detected events could be very close to the position of the source where they have been accelerated, opening the possibility to perform high energy cosmic ray astronomy. The detection horizon that is observable with charged particles, protons and nuclei, is limited to about 200 Mpc from Earth, due to the *GZK effect*, described in section 1.2. These interactions lead to a significant attenuation in the primary CRs flux, if coming from distant sources.
If the nearby sources are not uniformly distributed in the sky, then we expect that the arrival directions of the most energetic cosmic rays should be anisotropic, given the assumption that extra-galactic magnetic fields are not very strong.
The detection of UHECRs can be performed only indirectly by observing the result of their interactions with the Earth's atmosphere. The direct detection, i.e. with satellites, is unfeasible due to the extremely low expected fluxes, of the order of some particle per square kilometer per century. Indirect detection is performed by identifying the extensive air showers (EAS) that develop in the atmosphere, as a consequence of primary CRs interactions with air molecules. EAS can be detected using large area surface arrays of PMTs, which detect secondary charged particles, mainly electrons, photons, pions and muons, arriving at the ground level, or using sensors to identify the faint fluorescence light emission stimulated in the atmosphere as the EAS pass by: the so-called *fly's eye* technique [54].
UHECRs astronomy has several goals: the identification of the sources and of the production mechanisms of these particles, the study of the composition of primary nuclei, and of the extra-galactic magnetic fields.
A long list of experiments has pioneered the field of UHECRs detection, starting from two experiments that were realized in the 1960s: the American project Volcano Ranch[95] and the Russian project Yakutsk[87].
A compelling attempt to measure the average angular distance of the detected UHECRs events with respect to the large scale features of our galaxy and nearby extra-galactic sources is described in [118]. The analysis was performed using the complete data set of the Haverah Park [33] experiment, together with a limited statistics from other UHECRs experiments, running at that time. A total of 143 events above 2×10^{19} eV, and with a zenith angle $\theta < 45°$ was analyzed.
The arrival direction distribution was found to be fully consistent with uniformity at energies above 2×10^{19} eV. No significant correlation was found with large structures of the Milky Way, e.g. the galactic plane. Moreover, a visible but not extremely significant (about 2.8 σ in terms of Gaussian probabilities) concentration of events around the direction of the supergalactic plane was found, for events with energies

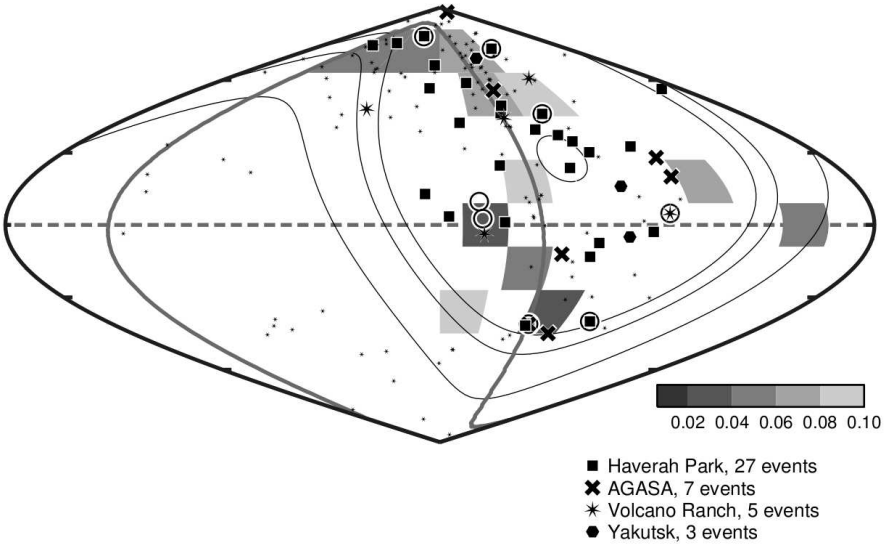

Figure 6.1. Arrival directions of events of energy higher than 4 $\times 10^{19}$ eV four the data sets described in the legend.The events are plotted in galactic coordinates, with galactic longitude from 0 to 360, from right to left. The eight events with energy above 10^{20} eV are shown with circles. The shading shows the statistical probability of the detected density of events. The thin lines show the detector exposures. Small asterisks show th position of 118 galaxies within z =0.005 that are detected in radio from the NASA-IPAC catalogue. Thick lines show the galactic (dashed) and the supergalactic planes. Picture taken from [118].

above $4\times$ 10^{19} eV, as shown in figure 6.1.
The supergalactic plane, shown as a thick solid line in figure 6.1, indicates a structure in the local Universe formed by the distribution of nearby radio galaxies and galaxy clusters (such as the Virgo cluster and the Pisces-Perseus supercluster).
The possibility to perform high energy cosmic ray astronomy has recently become more realistic with the commissioning of a hybrid detector, located in South Argentina, spread over an area of about 3000 km^2, the Pierre Auger Cosmic Rays Observatory [46].
UHECRs are detected indirectly, by means of both fluorescence detectors and PMTs, hosted in tanks filled with water. The unprecedented size of the detector is such that a large sample of data has been already collected, after a few years of data taking.
The Auger Collaboration has published [5] remarkable results about the arrival direction of their highest energy events. Data collected between 2004 and 2007 shows evidence for anisotropy in the distribution of the highest energy (E $> 5.7\times10^{19}$ eV) events. Moreover, the arrival directions of the 27 highest energy events and the positions of the closest AGN ($z_{max} = 0.017$) within the detector field of view, were found to be correlated. One of the most complete AGN catalogues, the Véron-Cetty and Véron catalogue [123], was used to search for correlation between the Auger events and the position of the astrophysical sources. It has been found that 20 out of 27 events have been detected within a cone of 3.2° aperture around at least one of the AGN positions. The expected number of correlated events assuming an

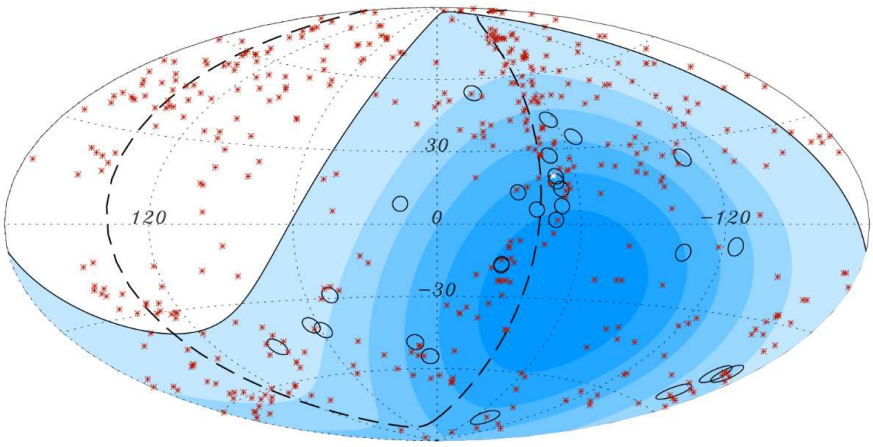

Figure 6.2. Skymap in galactic coordinates, in Aitoff projection, showing in black circles the arrival directions of the 27 Pierre Auger Observatory (PAO) events [5], with reconstructed energies above 57 EeV. The position of the 442 nearby AGN from the 12th edition of the Véron-Cetty and Véron [123] catalogue, with maximum redshift z=0.017 are shown in red asterisks. The solid line indicate the field of view of the PAO, while the dashed curve indicate the super galactic plane. Each colored band has equal integrated exposure. The nearby active galaxy Centaurus A is marked in white.

isotropic events distribution is estimated around 6, and the cumulative binomial probability of achieving this result as due to isotropic distribution is $P \sim 5 \times 10^{-9}$. Figure 6.2 shows the skymap, in galactic coordinates, with circles of radius 3.2° around each of the reconstructed arrival directions of the 27 events with energy E > 57 EeV detected by the Pierre Auger Observatory. Red asterisks correspond to the position of the 442 AGN with redshift smaller than 0.017 in the Véron-Cetty and Véron catalogue. Several considerations can be done on the basis of these results.
The most straightforward interpretation is that the AGN themselves might be the sources of the UHECRs, and that the angular deviation of 3.2° around the source position is simply due to the propagation of the charged particles from their sources. This would imply that, at least partially, the source of UHECRs have been identified together with the properties of the extra-galactic magnetic fields.
It is worth noticing that the angular resolution of the Auger Observatory is better than 1°, therefore the 3.2° degree cone is not due to instrumental effects. This deviation is accumulated during the entire trajectory of the particle and it has several contributions, coming from the region surrounding the source, the extra-galactic propagation and finally the deviations in the Milky Way.
This interpretation of the Auger data has lead to a lively discussion and still shows a number of controversial problems. One of the most debated aspects is that the catalogue used is not an unbiased statistical sample, since it is neither homogeneous nor statistically complete: moreover, the nature of the catalog, limits the ability of the correlation method to identify the actual sources of cosmic rays.
Another controversial aspect is the fact that the data taken with HiRes, an UHECRs fluorescence detector that has recently concluded the data-taking, has not confirmed the same result: no significant correlations between the HiRes-stereo data [2] and

the AGN location was found, the probability that data are consistent with isotropy being 97%. It is not clear, however, whether the systematic effects in the determination of the energy of primary particles could play some role.
The Auger data can also be interpreted [117],[72] assuming that the anisotropy observed is due to a single source, the nearby active galaxy Centaurus A (Cen A in the following), generating about one third of the 27 events, with a larger angular spread of the order of $\delta\theta \simeq 10^{\circ}$. Recent discovery of γ-ray emission from Cen A, has been reported by the Fermi-LAT Collaboration [3] as well as by the H.E.S.S. Collaboration [24], slightly supporting this latter hypothesis, even though more accurate measurements are needed to confirm the presence of hadronic mechanisms in this source.
Two important consideration arise from Auger results: space distribution of UHECR at highest energies is not uniform, while the conclusive answer to the question of what are actual sources of UHECR requires further study and wider data sample.
The Auger Collaboration has recently published updated results on the correlation problem, using data taken between 1 January, 2004 and 31 March, 2009 [7].
The total number of events above 57 EeV has now raised to 58, not yet increasing the evidence for anisotropy suggested by the analysis reported before. It has been shown that the degree of correlation with the objects of the AGN catalogue appears to be weaker than suggested by the earliest data. Moreover, the updated data sample shows an excess of events close to the direction of Cen A, not yet reaching a significant level.

6.2 Neutrino fluxes predictions

The observed anisotropy in the arrival direction of UHECRs events detected by Auger, as well as the hypothesis on the nature of their sources, gave raise to predictions of both γ-rays and neutrino fluxes from the same sources. We shortly describe the predictions made assuming that the most probable sources for the acceleration of protons to energies beyond 10^{20} eV are radio galaxies, as seen in section 1.4.2.
The acceleration of charged particles in these sources is expected to occur in relativistic jets emanating from a super massive black hole, that provides the central engine for the acceleration mechanism. These jets are considered where primary cosmic rays could be accelerated up to extremely high energies, interacting with matter and radiation and producing γ-rays and neutrinos. A particular class of candidate sources for UHECRs acceleration and, thus, for the production of HE neutrinos are radio galaxies with extended radio jets, namely Faranoff-Riley I galaxies (FR-I), with typical low luminosity radio lobes and knots showing non thermal emission due to electron acceleration in shock waves.
The most prominent FR-I galaxies are Cen A, M 87 and Perseus A, as well as flat spectrum radio sources BL Lac. J.K. Becker and P.L. Biermann [44] proposed the production of neutrinos from FR-I galaxies and computed the predicted diffuse neutrino flux from this kind of sources, located along the super galactic plane.
Assuming that the 20 Auger events above 57 EeV correlated with the distribution of nearby AGN from the catalogue actually come from those sources, several models allow to estimate the neutrino fluxes. Each source is considered to produce CRs

and neutrinos with an E^{-2} power law spectra, according to standard stochastic acceleration mechanisms [70]. Due to propagation effects, the observed differential flux of CRs is steeper than it was at the source: a power law with spectral index of 2.7 is assumed for the observed flux.
The estimation of the neutrino flux is made correlating the total neutrino energy flux, to the total proton energy flux observed at Earth by the Auger experiment.
Sources up to a maximum redshift are considered in the computation, the upper limit of $z = 0.03$ considered as the edge of the super galactic plane. The minimum redshift considered is given by the Cen A galaxy, with $z = 0.0008$ corresponding to a distance of 3.5 Mpc.
The corresponding neutrino flux for an E^{-2} spectrum is given by:

$$\frac{dN}{dE} = 1.4 \times 10^{-10} \cdot E^{-2} GeV s^{-1} sr^{-1} cm^{-2} \tag{6.2}$$

Using the correlation between the UHECRs and the distribution of AGN as a measure for the CR flux from the supergalactic plane, the resulting neutrino signal is about an order of magnitude below the current AMANDA upper limit to the diffuse neutrino flux [10].
This flux could be observed within the first years of observation by next generation cubic kilometer scale detectors, such as IceCube and KM3NeT.
F. Halzen and A. O'Murchadha [75] computed the neutrino flux from Cen A as well as the diffuse flux from all FR-I galaxies, assuming hadronic origin of the γ-ray observed by HESS and Fermi-LAT Collaborations.
Starting from the observed Auger CRs flux, the neutrino flux from Cen A is computed assuming a power law $\frac{dN}{dE} = E^{\alpha}$ with spectral index $\alpha = -2$. The number of Auger events correlating with Cen A depends on the unknown intergalactic magnetic fields. Two events correlate within 3 degrees, but up to ten events could be associated to this source allowing for a larger deflection. The neutrino flux expected from hadronic (pp) interactions in Cen A is:

$$\frac{dN}{dE} \leq 5 \times 10^{-10} \cdot E^{-2} GeV s^{-1} sr^{-1} cm^{-2} \tag{6.3}$$

Using this flux expression, about one event per year is expected for a generic neutrino telescope with an effective muon area of about 1 km^2.
Halzen and O'Murchadha also computed the diffuse neutrino flux from all sources within the *GZK* horizon, assuming that all FR-I galaxies have a luminosity equal to that of Cen A and M 87. Given the FR-I density and a numerical evaluation of the horizon, the diffuse neutrino flux can be computed, resulting in a value that is approximately 10% of the Waxman and Bahcall flux. The detection of the predicted flux should be feasible with the next generation cubic-kilometer scale neutrino telescopes.

6.3 Survey of a region of the super galactic plane

The Auger results indicate correlation between the highest energy CRs and the distribution of nearby AGN. The target of the present analysis is the search for uniformity, or excesses, of neutrino signals in a region that surrounds part of the supergalactic plane (SGP), where most of the extreme energy events detected by the Pierre Auger Observatory lie.
In the present analysis, a region of $30° \times 30°$ covering a particular region of the sky (declination $-60° \leq \delta \leq -30°$, right ascension $195° \leq \alpha \leq 225°$, corresponding to $-165° \leq \alpha \leq -135°$,) has been chosen to search for diffuse neutrino emission.
The region we have selected contains the bulk of the Auger events (6 out of 27 , with energy above 57 EeV) that lie near the SGP, in the vicinity of the Cen A galaxy. Several astrophysical sources, e.g. Cen A, are also contained in the region.
The number of events found in the candidate region, from now on indicated as *ON region*, will be compared to the number of events found in 11 regions of equal area, with the same declination ($-60° \leq \delta \leq -30°$) and exposure to up-going neutrinos, so that we have an accurate estimate of the atmospheric background. We assume that, for construction, this background characterizes also the ON region. Comparing the number of events found in the ON and OFF regions it will be possible to search for excesses of signal over the background. If no significant excess of signal will be found, an upper limit to the diffuse neutrino flux coming from the selected region will be set.

6.3.1 Data and Monte Carlo sample

The data used in this analysis correspond to the period from February 2nd to December 8th, 2007. For part of this period, data acquisition was interrupted due to sea operations for the deployment of new lines. In addition, some filtering has been applied in order to exclude periods in which the bioluminescence-induced optical background was high. The resulting effective live-time is 168 days.
The analysis takes into account 935 *Silver Runs*[1], whose trigger settings and specific features are listed in table 5.1.
The *Full Likelihood* reconstruction algorithm, due to its good pointing accuracy, has been used.
A full simulation of the atmospheric background has been performed, using the simulation tools described in chapter 5: the atmospheric neutrino background has been simulated with the GENHEN code, using the Bartol flux model[14], while atmospheric muons, also in bundles, have been simulated with the MUPAGE[56] simulation tool.

6.3.2 Optimization of the selection criteria

In order to reduce the large amount of misreconstructed down-going muons and to select the best reconstructed events in our data sample, some quality cuts have to be applied to reconstructed events. In the case of the present analysis, since we have used the *Full Likelihood* algorithm to reconstruct the ANTARES events,

[1] baseline rate lower than 120 KHz and burst-fraction below 20%

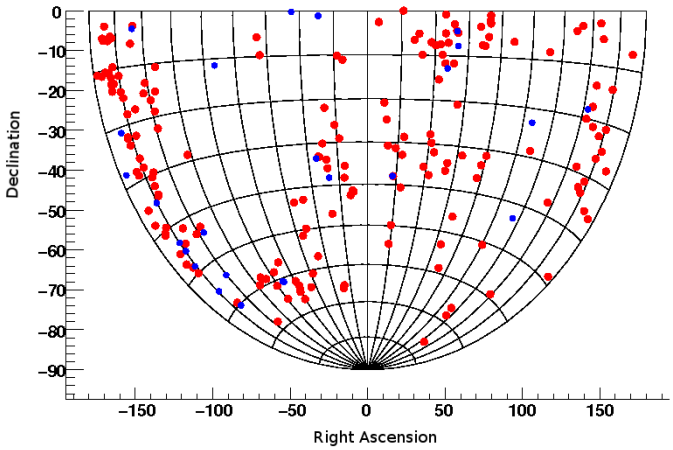

Figure 6.3. Skymap in equatorial coordinates, showing the 25 Auger events [5] reconstructed with energies higher than 57 EeV and declination not higher than 0° (blue dots), together with the nearby AGN (maximum redshift $z = 0.017$) from the Véron-Cetty and Véron catalogue (red dots) [123] with declination not higher than 0°. The ON region selected in the present analysis falls within the declination band $-60° \leq \delta \leq -30°$, with right ascension $195° \leq \alpha \leq 225°$, equivalent to $-165° \leq \alpha \leq -135°$. The remaining part of the declination band is used to estimate the background.

we have optimized the cut in the quality reconstruction parameter Λ, defined in section 5.3.6.

While in *routine measurements* the significance of the observed events, e.g. signal to noise ratio, can be optimized, in *difficult cases*, like for small or unobserved signal, background larger than signal, or measurements near a physical boundary, a more careful procedure should be followed. Assuming *a priori* that no signal will be observed, we optimize our selection criteria to be able to reach the optimal limit setting potential of the experiment. The evaluation of the optimal cuts is based on signal and background from Monte Carlo simulations.

Under the assumption that no signal will be observed, an upper limit to the neutrino flux that we would like to constrain can be set. Assuming that our experimental result, i.e. detecting a given number of signal and background events, can be described by Poisson statistics, an upper limit at the 90% confidence level (C.L.) to the Poisson expected value μ can be set. The computation of this quantity, called μ_{90}, is performed by using the Unified Approach developed by Feldman and Cousins [65]. This upper limit depends on the number of background events n_b and on the number of actually observed events n_{obs}. The corresponding upper limit to the flux $\Phi_{90}(E, \theta)$ can be obtained, with the same C.L., by scaling the source flux by the ratio of the upper limit to the signal expectation n_s, obtained by convolving the flux with the detector response, and assuming a specific model for the neutrino source flux. In the case of the present analysis an E^{-2} power law spectrum for the source has been assumed. Since we are aiming at placing an upper limit before performing the experiment, the classical concept of an ensemble of experiments allows us to calculate an *average upper limit*, which can take the place of the usual upper limit for this *a priori* estimate.

This average upper limit, that would be observed after hypothetical repetition of the experiment with expected background n_b and no true signal, can be obtained from simulations. By calling $\overline{\mu_{90}}$ the average upper limit on the expected value of the parameter μ, the upper limit on the flux (sensitivity) is then given by:

$$\overline{\Phi(E,\theta)_{90}} = \Phi(E,\theta)\frac{\overline{\mu_{90}}(n_{obs}, n_b)}{n_s} \tag{6.4}$$

Over an ensemble of identical experiments, the strongest constraint on the expected signal flux corresponds to the set of cuts that minimize the quantity:

$$\frac{\overline{\mu_{90}}(n_{obs}, n_b)}{n_s} \tag{6.5}$$

that is called the *Model Rejection Factor* [79] (MRF in the following). Figure 6.4 shows the MRF, as a function of the Λ parameter, computed for an E^{-2} neutrino flux with an arbitrary normalization to the neutrino flux of the source. Corresponding values are listed in table 6.1.
The number of events for signal and background are computed using the following cuts: $\Lambda > \Lambda_{TH}$, $\text{nlines}_{prefit} > 1$, i.e. the number of detection lines in which the reconstructed muon track was found to give signal, at the prefit level, and elevation not higher than -10°, i.e. only up-going tracks are considered. The cut is nlines_{prefit}

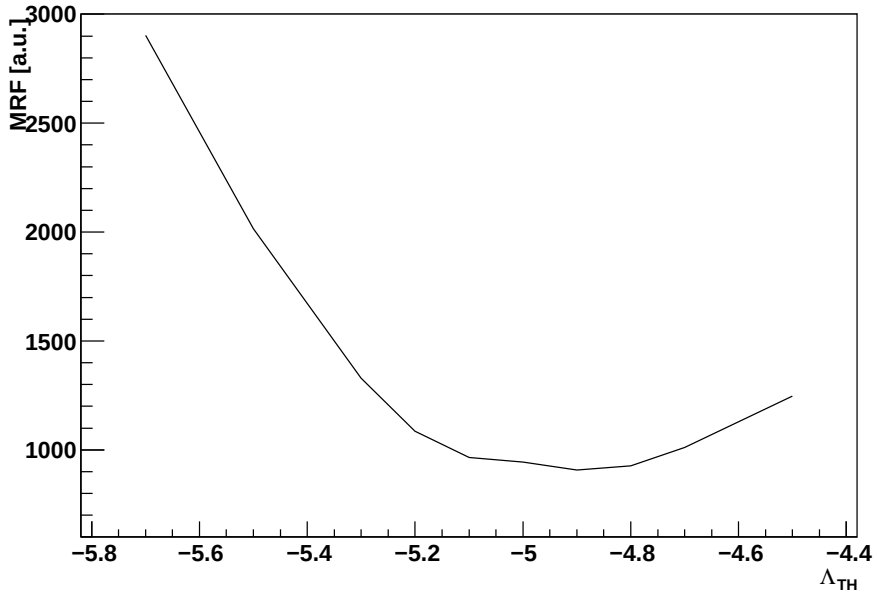

Figure 6.4. The MRF, defined in formula 6.11, as a function of the Λ parameter. The number of events for signal and background are computed from simulated events, using the following cuts: $\text{nlines}_{prefit} > 1$, elevation $< -10°$ and $\Lambda > \Lambda_{TH}$. The minimum value is found for $\Lambda >$ -4.9.

has been applied in order to enhance the reconstruction quality, as well as the cut in elevation, to suppress the muon background and to avoid horizontally reconstructed tracks.

The MRF has a minimum in the regions between $\Lambda >$ -5 and $\Lambda >$ -4.7, the absolute minimum being at $\Lambda >$ -4.9: this value will be used in our analysis as best reconstruction quality cut, along with $\text{nlines}_{prefit} > 1$, elevation $< -10°$. Using

Table 6.1. Expected signal and background events, from a full simulation reproducing 168 days lifetime of the 5 lines detector, used to compute the MRF, together with the MRF values as a function of Λ. $N_B(\nu)$ indicates the number of atmospheric neutrino events (background) over the ON and OFF regions, $N_B(\mu)$ indicates the number of atmospheric muon events (background) over the ON and OFF regions, $\overline{\mu_{90}}$ indicates the average upper limit, $N_S(\nu)$ indicates the number of expected signal events in the ON region, obtained using an E^{-2} power law spectra for the astrophysical neutrino flux, MRF indicates the *Model Rejection Factor* for the corresponding values of signal and background event.

	$N_B(\nu)$	$N_B(\mu)$	$\overline{\mu_{90}}$	$N_S(\nu)$	MRF
$\Lambda > -4.5$	22.1	0	3.8	0.003049	1246
$\Lambda > -4.7$	34.1	4.4	4.5	0.004452	1010
$\Lambda > -4.8$	40.6	5.8	4.8	0.005184	927
$\Lambda > -4.9$	47.2	19.7	5.4	0.005913	907
$\Lambda > -5.0$	53.8	41.3	6.2	0.006577	943
$\Lambda > -5.1$	60.7	72.0	7.0	0.007260	964
$\Lambda > -5.2$	67.6	141.8	8.5	0.007825	1086
$\Lambda > -5.3$	74.0	323.7	11.2	0.008422	1330
$\Lambda > -5.5$	85.6	1118.4	19.0	0.009425	2016
$\Lambda > -5.7$	95.2	3277.4	30.0	0.01033	2904

the optimized cuts, 176 events have been found over the whole skymap, 50 of those lying within within the ON or the OFF regions.
Considering the optimized cuts, leading to an average upper limit $\overline{\mu_{90}} = 5.4$ for a simulated active lifetime of 168 days, the corresponding upper limit to the diffuse neutrino flux (sensitivity) in the ON region has been set:

$$E^2 \, \overline{\Phi_{90}} < 5.5 \times 10^{-6} \, GeV cm^{-2} s^{-1} \tag{6.6}$$

for reference, the corresponding upper limit to the diffuse neutrino flux per unit solid angle has been computed, in order to compare it to the one obtained by Waxman and Bahcall [124], quoted in formula 4.1.
Under the assumption of uniform neutrino emission within the ON region, as well as along the SGP, the obtained sensitivity is:

$$E^2 \overline{\Phi_{90}} < 2.9 \times 10^{-5} GeV cm^{-2} s^{-1} sr^{-1} \tag{6.7}$$

that is several orders of magnitude above the Waxman and Bahcall upper limit.
The upper limit found is also above the theoretical prediction made by Becker and Biermann [44], on the diffuse neutrino flux from the radio galaxies along the SGP, reported in formula 6.2.

6.3.3 Comparison between Data and Monte Carlo

In this section the results of the comparison between data and the simulated atmospheric background are shown. These distributions include the whole data sample

corresponding to 168 days, i.e. comprising those events whose arrival directions are not within the declination band selected for the survey. Applied cuts will be specified for each plot.

Elevation and azimuth angles are used to identify the muons arrival directions

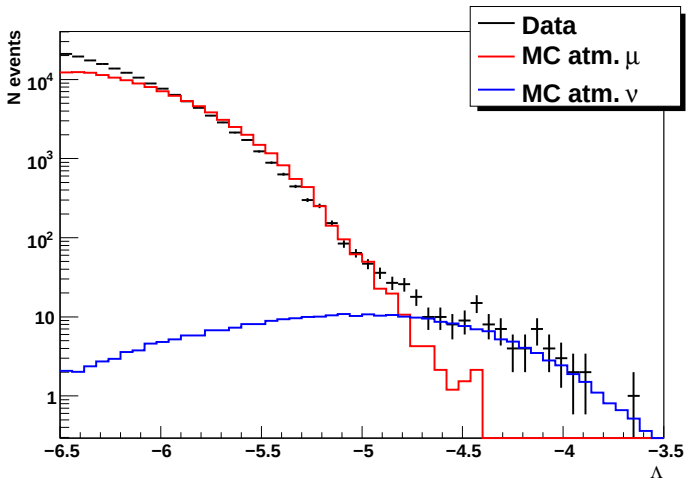

Figure 6.5. Distribution of the Λ parameter, used to evaluate the quality of the reconstruction performed with the *Full likelihood* algorithm. Data are indicated with black crosses (only statistical errors are shown), while MC is indicated with solid lines (red for atmospheric muons and blue for atmospheric neutrinos). The cuts applied are $\text{nlines}_{prefit} > 1$ and elevation $\theta < -10°$.

in the detector frame of reference. The ANTARES detector has been designed to identify the arrival direction of neutrino-induced muons that propagate up-going through the detector, so that a given astrophysical source is visible, in the detector frame of reference, only if it is located below the horizon.

The azimuth (ϕ) angle is the compass bearing, relative to the North, of a point on the horizon directly beneath an observed object. The elevation angle (θ) is determined by first finding the azimuth angle, and then measuring the angle between that point and the object, in the reference frame of the detector.

Elevation angles for objects above the horizon range from 0° (on the horizon) up to 90° (at the zenith). Negative values of elevation are those relevant for the search of a cosmic signal, corresponding to sources below the horizon and thus to up-going tracks.

The reconstruction quality parameter Λ is shown in figure 6.5, for data and MC. The following cut are applied to the reconstructed events (both data and MC): $\text{nlines}_{prefit} > 1$ and elevation $< -10°$.

It can be seen that there is a fair agreement between data and MC, especially for values of Λ higher than -6, where the number of misreconstructed atmospheric muons starts to be reduced. The chosen cut, Λ > -4.9, is efficient in the rejection of atmospheric muons, even though a fraction of events still affects the data sample.

The distributions of elevation and azimuth for both data and MC are shown in figures 6.6 and 6.7. The plots on the left in both figures have been produced with no cut in the Λ variable, while the optimized cut is applied to the plots on the

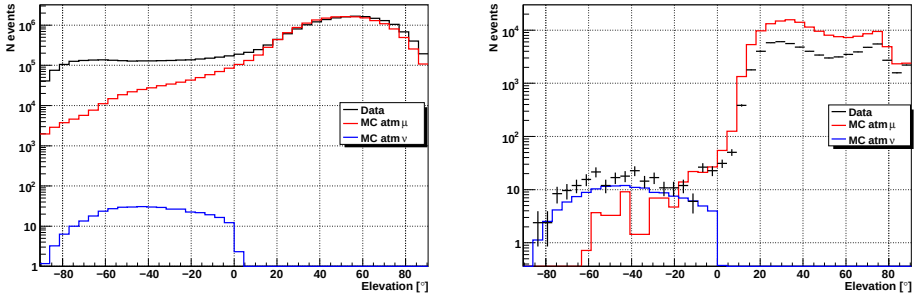

Figure 6.6. Distributions of elevation, for both data (in black) and simulated atmospheric background from muons (red curve) and neutrinos (blue curve). *Left*: the cut used is $\text{nlines}_{prefit} > 1$. *Right*: the cut used is $\text{nlines}_{prefit} > 1$ and $\Lambda > -4.9$.

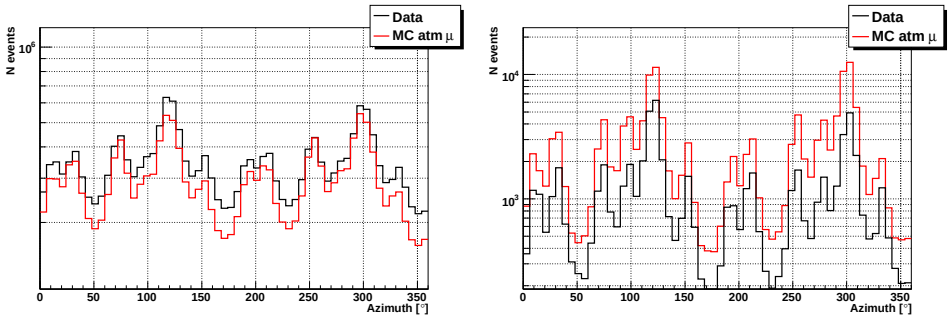

Figure 6.7. Distribution of azimuth, for both data and MC atmospheric background. *Left*: the cut used is $\text{nlines}_{prefit} > 1$. *Right*: the cut used is $\text{nlines}_{prefit} > 1$ and $\Lambda > -4.9$.

right.
It can be seen that, especially for negative values of elevation, the cut in Λ enhances the agreement.
The distribution of the azimuth angle could be expected to be uniform, because of the Earth's rotation: the peaks that can be seen in both plots in figure 6.7 appear as a consequence of the discreteness of the detector. The present analysis is performed with a detector made of only five detection lines, so that some excluded as well as preferred directions for the reconstructed arrival directions do exist, producing the dips and the peaks that have been observed.
While the distributions of the azimuth angle reflect the detector geometry, the distributions of elevation shows the different origin of the detected events: down-going atmospheric muons and up-going atmospheric neutrinos. The distributions of reconstructed events are clearly dominated by down-going events, corresponding to positive values of the elevation: these events are due to atmospheric muons.
The detection is optimized to identify up-going tracks, the ANTARES PMTs photocatodes being at 45° down-ward looking, so that the huge flux of atmospheric muons produce a wide fraction of misreconstructed events, due to both detector design peculiar aspects and the specific features of the reconstruction algorithm used: it has been seen in section 5.3 that the *Full likelihood* algorithm has been tailored for the search for neutrino point-like search, providing a more efficient reconstruction

of up-going events with respect to down-going events. The application of the quality reconstruction cut is such that the agreement between data and MC in greatly enhanced, both in shape and in number of reconstructed events, nevertheless the agreement is not yet satisfactory for those events reconstructed as down-going.
Once the reconstruction of the track parameters has been performed, the local coordinates can be converted in celestial coordinates: in the present analysis the equatorial coordinate system has been used, as schematically defined in figure 6.8. The

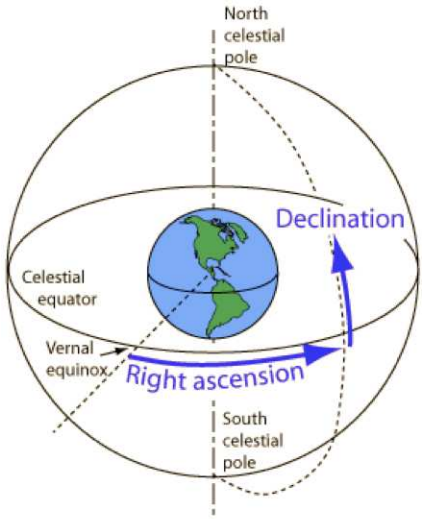

Figure 6.8. Schematic description of the equatorial coordinates.

distributions of right ascension α and declination δ for both data an atmospheric background MC are shown in figure 6.9, where the optimized cuts are applied. The

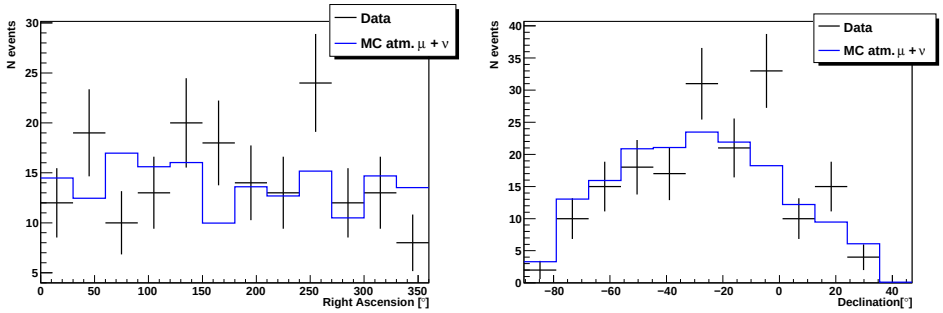

Figure 6.9. Distributions of equatorial coordinates, for both data and MC background, for the cuts used in this analysis. Black crosses indicate data events with statistical errors, while the blue curve shows the MC atmospheric background from muons and neutrinos.*Left:* Distribution of right ascension.*Right:* Distribution of declination.

distribution of right ascension is expected to be flat, as confirmed by data points in the left plot in figure 6.9. The distribution of declination is not uniform as expected, due to the fact that the detector design has been optimized for the search for up-going tracks. Moreover, the applied cut in elevation ($\theta < $ -10°) limits the observable

horizon to declinations $\delta < 40$ °, as can be seen in the right plot in figure 6.9.
As a conclusion for this section, it can be observed that we have reached a fair agreement between data and Monte Carlo expectations concerning atmospheric neutrinos, while concerning atmospheric muons the agreement is not yet complete. We can infer that, even though discrepancies are still present, the present simulation reproduces in an adequate way the experimental conditions.

6.3.4 Discovery Potential

Starting from a given number of background events we can evaluate the number of events that should be observed in the ON region (signal plus background) to lead to a discovery. We assume that there is evidence for a discovery when we find a 5σ excess of signal over the background, implying that the probability that the result obtained is due to an upward fluctuation of the background is very small, i.e. smaller than 2.85×10^{-7}. The latter value is the integral of the one-sided tail beyond 5σ of a normalized Gaussian, as in the following formula:

$$\sum_{n_{obs}=n_0}^{+\infty} P(n_{obs}| < n_b >) \leq 2.85 \times 10^{-7} \tag{6.8}$$

where $P(n_{obs}| < n_b >)$ is the Poisson probability, with mean value $< n_b >$, evaluated from the MC background of atmospheric muons and neutrinos. We can compute the Discovery Potential [26], i. e. the minimum number of events n_0 (signal and background) that we have to detect in order to reach a 5σ discovery. The n_0 as a function of Λ is shown in figure 6.10. Considering the cut that minimizes the MRF, i.e. $\Lambda >$ -4.9, we need 22 events in the ON region to reach the required significance. We have also computed the signal strength, n_s, such that with a 70%,

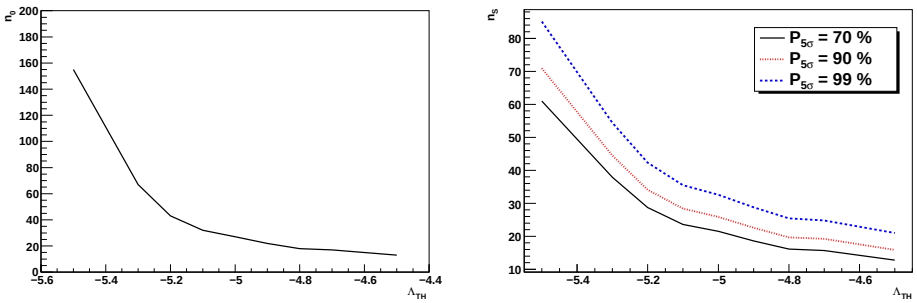

Figure 6.10. *Left*: Discovery Potential, i.e. the minimum number of events n_0 (signal and background) that we have to detect in order to reach a 5σ discovery, as a function of the Λ parameter. *Right*: Signal strength, n_s, such that with a 70%, 90 or 99% probability, we can observe a total number of events (signal and background) which is sufficient to claim a 5σ discovery.

90 or 99% probability, we can observe a total number of events in the ON and OFF regions (signal plus background) which is sufficient to claim a 5σ discovery. The signal strength as function of Λ is shown in the right plot in figure 6.10. Using the optimized value of the cut, $\Lambda >$ -4.9, we have computed the detection probability as a function of the signal events n_s: the result is shown in figure 6.11.

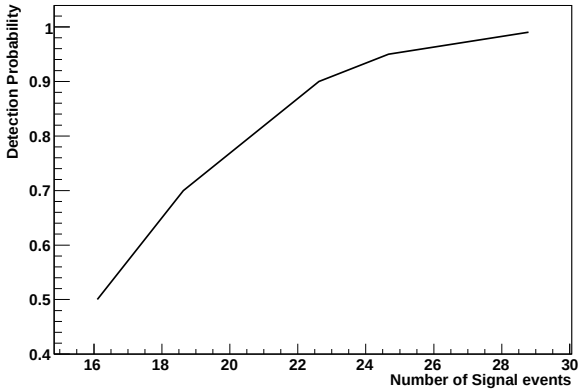

Figure 6.11. Detection probability as a function of the signal events n_s: the optimized cut in Λ has been used.

Table 6.2. Discovery potential for several values of the Λ parameter, for the cut used in this analysis.

	n_0	P	$n_S(70\%)$	$n_S(90\%)$	$n_S(99\%)$
$\Lambda > -4.5$	13	8.13E-08	12.8	15.9	21.0
$\Lambda > -4.7$	17	5.63E-08	15.7	19.2	24.8
$\Lambda > -4.8$	18	1.54E-07	16.1	19.7	25.4
$\Lambda > -4.9$	22	1.14E-07	18.6	22.6	28.8
$\Lambda > -5.0$	27	8.53E-08	21.5	25.9	32.6
$\Lambda > -5.1$	32	2.24E-07	23.6	28.4	35.5
$\Lambda > -5.2$	43	1.79E-07	28.7	34.1	42.3
$\Lambda > -5.3$	67	1.56E-07	37.9	44.5	54.4
$\Lambda > -5.5$	155	2.52E-07	61.0	70.9	85.1

6.3.5 Results of the survey

Aim of the present analysis is the study of the distribution of the neutrino signal in the ON and OFF regions, motivated by the observed anisotropy in the arrival directions of UHECRs, that could provide fundamental clues for the identification of sites where hadronic acceleration mechanisms, and thus HE neutrino production, take place.
The following plots show the results of the analysis. The plot in figure 6.12 shows the number of events that have been found in each region (both OFF and ON), i.e. in each right ascension bin, falling within the selected declination band. The corresponding values are listed in table 6.3. We perform an hypothesis test[66] to check whether or not the two events found in the ON region are compatible with background fluctuations. The hypothesis H_0 that we want to test is that our data follow a Poisson distribution with mean value $<N_{off}>$, given by the average number of events found in the OFF regions. The number of events that are measured in the ON region is referred to as N_{on}. We choose a significance level $\alpha = 0.05$, as threshold value to accept or reject the hypothesis H_0. The *p-value* is defined as the

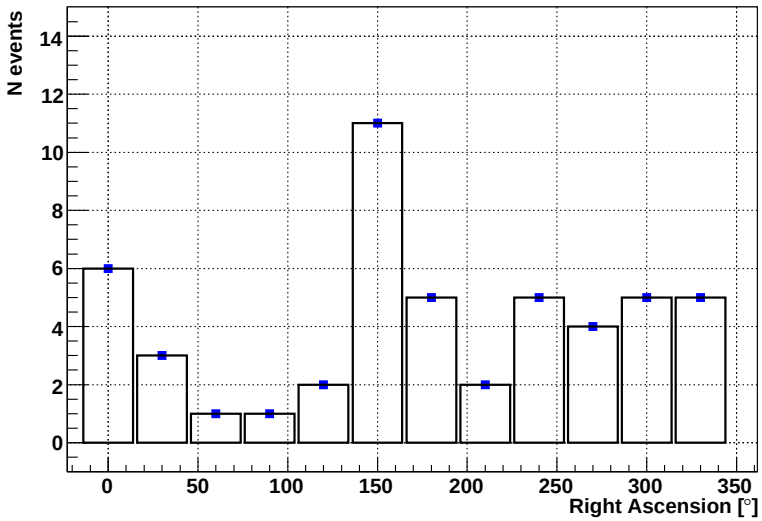

Figure 6.12. Number of events found in each one of the 12 regions in which the declination band ($-60° \leq \delta \leq -30°$) has been divided, including the ON region. Errors are only statistical.

probability to observe at least as many events as we have observed in the ON region, given the *only-background* hypothesis, that is $p = P(N \geq N_{on}|H_0, < N_{off} >)$.
If $p > \alpha$ the hypothesis is accepted, while if p is smaller than α, then the hypothesis is rejected.
We have found N_{on}=2 and an average number of background events $< N_{off} >$=4.4, so that the *p-value* is equal to 0.93: the *only-background* hypothesis is accepted.
Since no excess of signal has been found, we have computed the upper limit μ_{90} on the number of event found in the ON region, following the Unified Approach [65].
An upper limit μ_{90}=2.1 (90% C.L.) has been obtained for the number of signal events in the ON region.
The upper limit to the E^{-2} neutrino flux from the ON region, has been computed as described in section 6.3.2, obtaining:

$$E^2\,\Phi_{90} < 2.1 \times 10^{-6}\,GeV cm^{-2} s^{-1} \tag{6.9}$$

Under the assumption of uniform neutrino emission within the ON region, as well as along the SGP, the obtained upper limit to the diffuse neutrino flux is:

$$E^2\,\Phi_{90} < 1.1 \times 10^{-5}\,GeV cm^{-2} s^{-1} sr^{-1} \tag{6.10}$$

We can compare this limit to the corresponding limit obtained by the AMANDA Collaboration, as in figure 6.14. We see that the present limit, given the reduced size of the detector and the short lifetime of the data sample, is not yet competitive no even compatible with the result published by the AMANDA Collaboration, obtained after 4 years of data taking. Nevertheless the one obtained in the present analysis is the first upper limit on the diffuse neutrino flux set using data collected with the ANTARES detector.

Table 6.3. Number of events found in each region falling within the selected declination band $-60° \leq \delta \leq -30°$. These results have been obtained from the analysis of the ANTARES 2007 *Silver Runs*, corresponding to an active lifetime of 168 days.

Sky Region ($-60° \leq \delta \leq -30°$)	N events
$(0° \leq \alpha < 15°) + (345° \leq \alpha < 360°)$	6
$15° \leq \alpha < 45°$	3
$45° \leq \alpha < 75°$	1
$75° \leq \alpha < 105°$	1
$105° \leq \alpha < 135°$	2
$135° \leq \alpha < 165°$	11
$165° \leq \alpha < 195°$	5
$195° \leq \alpha \leq 225°$	2
$225° < \alpha < 255°$	5
$255° \leq \alpha < 285°$	4
$285° \leq \alpha < 315°$	5
$315° \leq \alpha < 345°$	5

In this analysis no attempt has been made to evaluate the energy of the reconstructed tracks. The atmospheric neutrino flux is thought to be steeper than the astrophysical one, so that at energies higher than some TeV the neutrino flux at the detector should be dominated by the astrophysical events. The use of an energy estimator could improve the sensitivity of the search by reducing the number of atmospheric neutrino events in the ON and OFF regions. The events classification in energy can be pursued by using the correlation between the hits amplitude and the muon energy from simulation. At present energy estimators are not implemented in the standard ANTARES software, even though careful studies are under way.

6.3.6 Serendipitous search

Looking at table 6.3 we see that several bins show not negligible fluctuations given an average number of about 4 events per region, while these fluctuations are not expected from simulations, as shown in figure 6.13.
As a second step in this analysis we have investigated these fluctuations, searching for a significant excess of signal in each of the eleven OFF regions that have been used to estimate the background. This procedure is called *serendipitous search*.
We have compared the number of events found in each region to the value n=4.2, that is the average number of events found in the 12 regions in which we have divided the declination band. This average value is well within MC expectations, as can be seen in figure 6.13.
The *serendipitous search* method is sketched in figure 6.15, and the corresponding results are reported in table 6.4.
The lowest *p-value* (corresponding to 2.8σ in terms of gaussian probabilities) is obtained for the region with right ascension $135° \leq \alpha < 165°$. We have to take into account the fact that we have made several *attemps* to perform our measurement, by dividing the declination band in twelve regions of equal area and declination. We have thus to multiply the obtained *p-value*, usually referred to as *pre-trial*, for

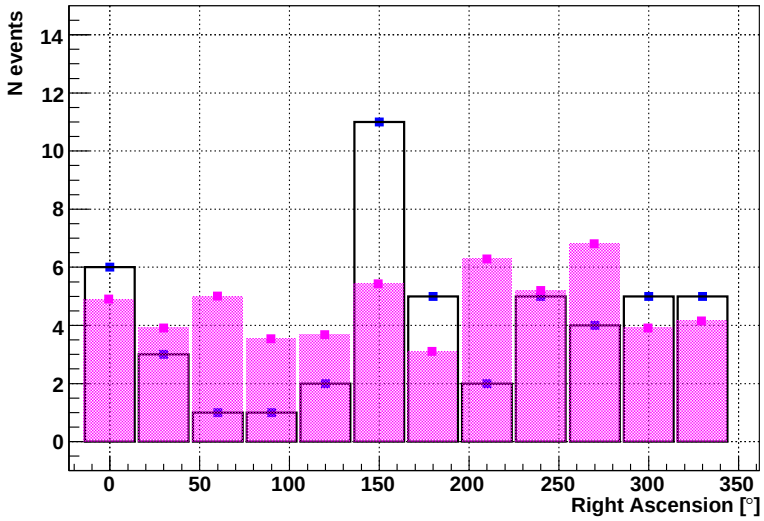

Figure 6.13. Number of data (in blue) and MC atmospheric background (in magenta) events found in each of the ON and OFF regions. Errors for data events are only statistical. These results refer to an active lifetime of 168 days of data-taking with 5 ANTARES lines.

the number of independent trials that we performed, that is 12. The *post-trial p-value* is then 5%, confirming our initial hypothesis, that is our data sample is only composed of background events.

6.4 Sensitivity studies for the full detector

The analysis method has been described in the previous sections and applied to data collected by the ANTARES experiment during 2007, when the detector was only composed by 5 lines. In this section I will describe the optimization of the selection criteria and the study of the sensitivity of the search, for a simulated data sample corresponding to one year lifetime of the full ANTARES detector. The discovery potential of the search method will be also discussed.
The following study has been performed using the same simulation programs that have been used for the 5 lines data analysis.

6.4.1 Optimization of the selection criteria

We have used the *Full Likelihood* algorithm to reconstruct muon events, so that we aim at optimizing the cut in the quality reconstruction parameter Λ, defined in section 5.3.6, to reduce the large amount of misreconstructed down-going muons and to select the best reconstructed events in our data sample.
Assuming a priori that no signal will be observed, our goal is to reach the optimal limit setting potential of the experiment.
The evaluation of the optimal cuts is based on simulated signal and background events for 1 year lifetime of the full ANTARES detector. Under the assumption that no signal will be observed, an upper limit to the neutrino flux that we would

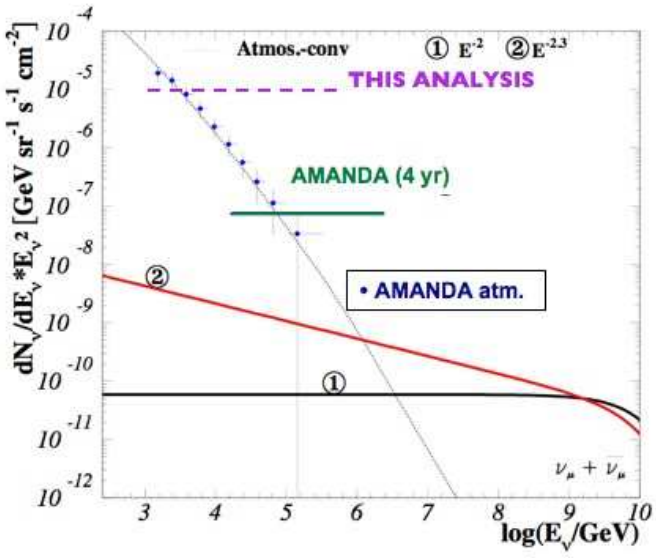

Figure 6.14. Upper limit to the diffuse neutrino flux obtained from 2007 data of the ANTARES detector (168 days lifetime), compared to the results obtained by AMANDA Collaboration [10]. The atmospheric neutrino flux obtained by the AMANDA Collaboration is also shown. The black and red solid lines refer to theoretical predictions from [44].

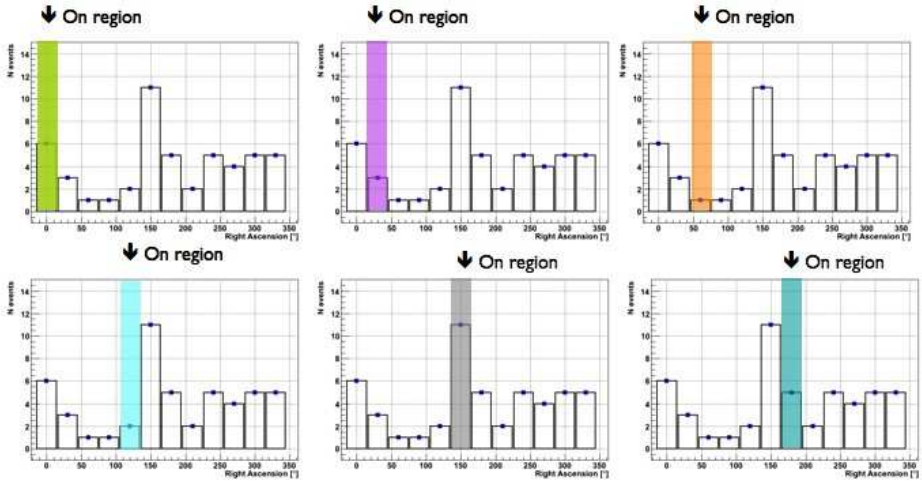

Figure 6.15. Basic idea of the *serendipitous search*: the number of events found in each of the 12 regions is compared to the average number of events found, to search for a significant excess of signal over the average event number.

like to constrain can be set, using the procedure described in section 6.3.2.
The strongest constraint on the expected signal flux corresponds to the set of cuts that minimize the *Model Rejection Factor* [79](MRF in the following) defined as:

$$\frac{\overline{\mu_{90}}(n_{obs}, n_b)}{n_s} \tag{6.11}$$

Table 6.4. Results of the *serendipitous search* within the selected declination band $-60° \leq \delta \leq -30°$. These are the results of the analysis of the ANTARES 2007 *Silver Runs*, corresponding to an active lifetime of 168 days. Only *pre-trial p-values* are quoted.

Sky Region ($-60° \leq \delta \leq -30°$)	N events	n	$p-value$
$(0° \leq \alpha < 15°) + (345° \leq \alpha < 360°)$	6	4.2	0.247
$15° \leq \alpha < 45°$	3	4.2	0.790
$45° \leq \alpha < 75°$	1	4.2	0.985
$75° \leq \alpha < 105°$	1	4.2	0.985
$105° \leq \alpha < 135°$	2	4.2	0.922
$135° \leq \alpha < 165°$	11	4.2	0.004
$165° \leq \alpha < 195°$	5	4.2	0.410
$195° \leq \alpha \leq 225°$	2	4.2	0.922
$225° < \alpha < 255°$	5	4.2	0.410
$255° \leq \alpha < 285°$	4	4.2	0.604
$285° \leq \alpha < 315°$	5	4.2	0.410
$315° \leq \alpha < 345°$	5	4.2	0.410

where $\overline{\mu_{90}}$ is the average upper limit and n_s is the number of signal events for an E^{-2} power-law spectra for the astrophysical neutrino flux, with an arbitrary normalization. Figure 6.16 shows the MRF, as a function of the Λ parameter, while corresponding values are listed in table 6.5.
The number of signal and background events have been obtained using the following cuts: $\Lambda > \Lambda_{TH}$, $\text{nlines}_{prefit} > 1$ and elevation not higher than -10°. The MRF has a minimum at $\Lambda >$ -5: this value will be used in our analysis as best reconstruction quality cut, along with $\text{nlines}_{prefit} > 1$ and elevation $< -10°$. Considering the optimized cuts, leading to an average upper limit $\overline{\mu_{90}} = 9.10$ for one year simulated lifetime, the corresponding upper limit to the neutrino flux (sensitivity) in the ON region has been set:

$$E^2 \, \overline{\Phi_{90}} < 1.5 \times 10^{-6} \, GeV cm^{-2} s^{-1} \tag{6.12}$$

The corresponding sensitivity to the diffuse neutrino flux per unit solid angle has been computed under the assumption of uniform neutrino emission within the ON region, as well as along the SGP, obtaining:

$$E^2 \overline{\Phi_{90}} < 7.7 \times 10^{-6} GeV cm^{-2} s^{-1} sr^{-1} \tag{6.13}$$

that is about a factor of three better than the sensitivity values in 6.7 and 6.6, obtained from the 5 lines MC. These values are compatible with the expected enhancement due to both the enlarged detector value and the larger lifetime considered.

6.4.2 Discovery Potential

We can use the full simulation of the ANTARES detector to study the Discovery Potential [26], as discussed in section 6.3.4. This quantity is computed assuming that the experimental results of our experiment are described by a Poisson process, with mean value $< n_b >$, evaluated from the simulation of background of atmospheric

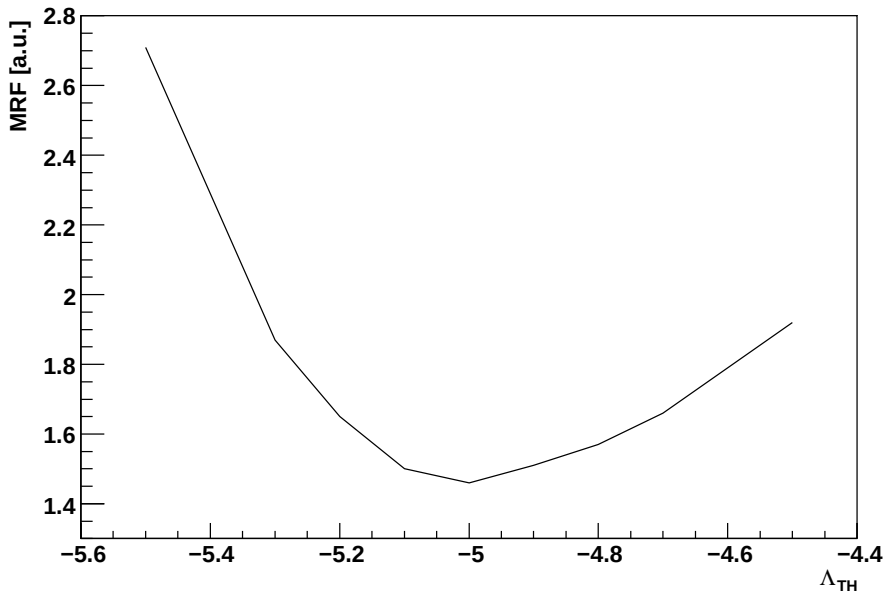

Figure 6.16. The MRF as a function of the Λ parameter, obtained from 1 year data taking simulation of the full ANTARES detector. The number of signal and background events have been obtained from simulated events, using the following cuts: $\text{nlines}_{prefit} > 1$, elevation < -10° and $\Lambda > \Lambda_{TH}$. The minimum value is found for $\Lambda >$ -5.

muons and neutrinos, as in formula 6.8.
The n_0 as a function of Λ is shown in the plot on the left in figure 6.17. Considering the cut that minimizes the MRF, $\Lambda >$ -5, we need 48 events in the ON region to reach the required significance after 1 year data taking.
We have also computed the signal strength, n_s, such that with a 70%, 90 or 99% probability, we can observe a total number of events in the ON and OFF regions (signal plus background) which is sufficient to claim a 5σ discovery. The signal strength as function of Λ is shown in the right plot in figure 6.17. Using the optimized value of the cut, $\Lambda >$ -5, we have computed the detection probability as a function of the signal events n_s: the result is shown in figure 6.18.

Table 6.5. Expected signal and background events, from MC reproducing 1 year lifetime of the full detector, used to compute the MRF, together with the MRF value for different values of Λ. $N_B(\nu)$ indicates the number of atmospheric neutrinos (background) over the ON and OFF regions, $N_B(\mu)$ indicates the number of atmospheric muons (background) over the ON and OFF regions, $\overline{\mu_{90}}$ indicates the average upper limit, $N_S(\nu)$ indicates the number of expected signal events in the ON region, obtained using an E^{-2} power law spectra for the astrophysical neutrino flux, MRF indicates the *Model Rejection Factor* for the corresponding values of signal and background event.

	$N_B(\nu)$	$N_B(\mu)$	$\overline{\mu_{90}}$	$N_S(\nu)$	MRF
$\Lambda > -4.5$	80.03	0.	5.74	2.99	1.92
$\Lambda > -4.7$	139.16	0.	7.18	4.32	1.66
$\Lambda > -4.8$	173.98	0.	7.85	4.98	1.57
$\Lambda > -4.9$	210.14	0.	8.54	5.64	1.51
$\Lambda > -5.0$	250.45	0.	9.10	6.22	1.46
$\Lambda > -5.1$	292.57	24.30	10.20	6.80	1.50
$\Lambda > -5.2$	334.70	133.63	12.10	7.33	1.65
$\Lambda > -5.3$	377.06	328.01	14.60	7.82	1.87
$\Lambda > -5.5$	459.47	1555.03	23.50	8.67	2.71

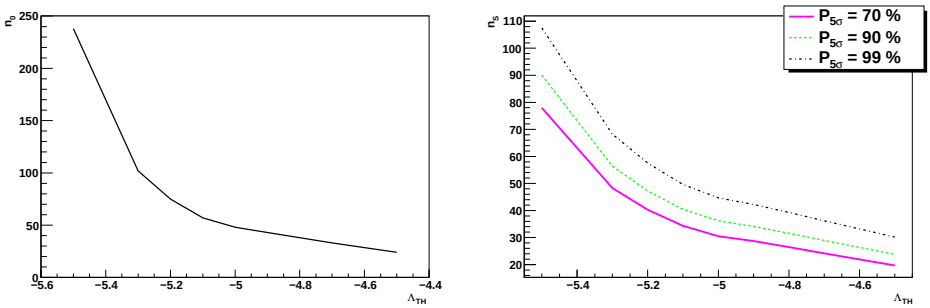

Figure 6.17. *Left*: Discovery Potential obtained from 1 year data-taking simulation of the full ANTARES detector as a function of the Λ parameter. *Right*: Signal strength, n_s, such that with a 70%, 90 or 99% probability, we can observe a total number of events (signal and background) which is sufficient to claim a 5σ discovery, for the full ANTARES detector after 1 year data-taking, as a function of Λ.

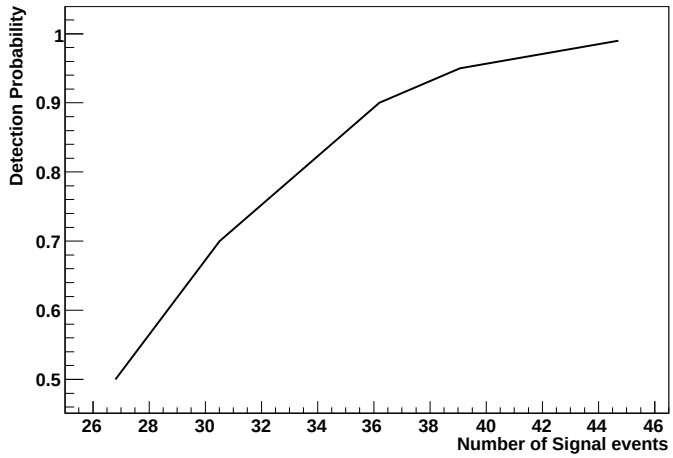

Figure 6.18. Detection probability expected for the full ANTARES detector detector after one year data taking, as a function of the signal events n_s. The optimized cut in Λ has been used.

Table 6.6. Discovery potential, corresponding probability, as in formula6.8, and signal strength n_S for several values of the Λ parameter, for the cut used in this analysis. Discovery potential n_0 and n_s are defined in section 6.4.2

	n_0	P	$n_S(70\%)$	$n_S(90\%)$	$n_S(99\%)$
$\Lambda > -4.5$	24	1.67E-7	19.64	23.79	30.18
$\Lambda > -4.7$	33	2.13E-7	24.16	28.95	36.22
$\Lambda > -4.8$	38	2.06E-7	26.48	31.59	39.30
$\Lambda > -4.9$	43	1.96E-7	28.68	34.08	42.20
$\Lambda > -5.0$	48	2.60E-7	30.51	36.20	44.71
$\Lambda > -5.1$	57	1.64E-7	34.31	40.47	49.62
$\Lambda > -5.2$	75	2.07E-7	40.27	47.27	57.59
$\Lambda > -5.3$	102	2.00E-7	48.30	56.39	68.21
$\Lambda > -5.5$	238	2.01E-7	77.98	90.10	107.49

Chapter 7

Summary and conclusions

Ever since the original idea of a neutrino telescope based on the detection of the secondary particles produced in neutrino interactions was discussed, several attempts have been made towards the realization of an apparatus whose main goal is the detection of astrophysical neutrinos. Due to the low fluxes expected and to the fact that neutrinos are only weakly interacting particles, cubic-kilometer scale detectors are required.
The detection principle relies on the observation, using a 3-dimensional array of photomultiplier tubes, of the charged leptons produced in charged current neutrino interactions with the medium surrounding the detector. Ultrarelativistic charged leptons, in particular muons, can be identified by means of the visible Čerenkov radiation that they induce passing through the medium.
An high-energy muon neutrino coming through the Earth from the Southern Hemisphere can be identified by the secondary muon moving upward through the detector. Given the known positions of the photomultiplier tubes and the measured arrival times of the Čerenkov photons, the track of the muon can be reconstructed.
The signal produced by astrophysical neutrino-induced particles can be distinguished from the background, coming from atmospheric muons (mainly down-going) and atmospheric neutrinos (almost isotropic), produced in cosmic rays interactions with nuclei on top of the atmosphere.
The analysis described in this PhD thesis has been developed within the ANTARES Collaboration, which completed in 2008 the realization of what is currently the largest high energy neutrino telescope in the Northern hemisphere.
The detector is composed of twelve vertical lines, placed at a depth of about 2500 meters, 40 km off the coasts of Toulon, France.
The analysis has been performed using the data collected by the ANTARES experiment during 2007, when the detector was only composed by 5 lines. The detector lifetime for the data sample used corresponds to 168 days, excluding periods that are characterized by high environmental background and considering no data-taking periods due to temporary shut down of the detector.
For the study of ν_μ induced events we simulated both signal and background interactions using an event kinematics simulation code developed within the ANTARES Collaboration. The simulation of the flux of atmospheric muons crossing the detector volume has been performed using a muon generator that makes use of parametric formulas to estimate the underwater muon flux at the detector depth.

The aim of the analysis is the study of the distribution of neutrino arrival directions over an extended region of sky that surrounds part of the supergalactic plane. This region has recently emerged as very important concerning the identification of candidate sites for the acceleration of cosmic rays and consequently for the production of high energy neutrinos.
The region that we have selected, referred to as *ON region*, has been chosen also on the basis of the recent results from the Pierre Auger Observatory, which reported a significant correlation between the arrival directions of ultra high energy events and the positions of nearby AGN.
The *ON region* is located in the declination band $-60^\circ \leq \delta \leq -30^\circ$ with right ascension $195^\circ \leq \alpha \leq 225^\circ$.
We have used the *Full Likelihood* algorithm to reconstruct muon events, so that we have optimized the cut in the quality reconstruction parameter Λ, to reduce the large amount of misreconstructed down-going muons and to select the best reconstructed events in our data sample. The optimization of selection criteria, that have been later applied to the data sample, has been accomplished from simulated events (background and signal), assuming an E^{-2} power-law spectra for the astrophysical neutrino flux, and by looking for the value of the Λ parameter that minimizes the *Model Rejection Factor*.
Eleven regions, referred to as *OFF regions*, of equal area and declination, have been chosen to estimate the background. These regions fall within the same declination band in which the *ON region* lies, $-60^\circ \leq \delta \leq -30^\circ$. The background that has been estimated from the *OFF regions* has been assumed to affect the *ON region* in the same way.
No statistically relevant excess of signal was found in the data sample: two events were found in the *ON region* and have been compared to the background expectations (given an average number of 4.4 events in the *OFF regions*), by performing an hypothesis test that resulted in confirming that our data sample was only made of background events.
Given that no excess has been found, an upper limit to the number of neutrino signal events, and thus to the flux of astrophysical neutrinos from the *ON region* has been set. The limit thus obtained, under the hypothesis of a E^{-2} power-law spectra for the astrophysical neutrino flux is $E^2\,\Phi_{90} < 2.1 \times 10^{-6}\,GeV cm^{-2} s^{-1}$. Assuming a uniform distribution of sources in the ON region as well as along the supergalactic plane, it has been possible to set an upper limit to the diffuse neutrino flux: $E^2\,\Phi_{90} < 1.1 \times 10^{-5}\,GeV cm^{-2} s^{-1} sr^{-1}$. This limit is several orders of magnitude higher than the theoretical predictions [44], and it is two orders of magnitude higher than the limit set by the AMANDA Collaboration [10] to the diffuse neutrino flux. It is noteworthy that this upper limit, even if not yet competitive with those from other experiments, is the first limit on the diffuse neutrino flux measured with the ANTARES detector, but with a limited data sample, collected in a reduced detector configuration.
Besides the search for a possible signal excess in the ON region, a *serendipitous search* has also been accomplished in order to investigate the presence of a significant excess of signal in each of the eleven OFF regions. Using this method no excess of signal has been found as well. The lowest *p-value* has been obtained for the region with right ascension $135^\circ \leq \alpha < 165^\circ$. Taking into account the trial

factors, the final *p-value* is 5%, well compatible with the hypothesis that our data sample is only made of background events.
The sensitivity of the proposed method for the full detector, in operation since May 2008, have also been evaluated. A dedicated one year lifetime Monte Carlo sample of both signal and background events has been produced and has been used to set optimal selection criteria that will be soon applied to data. Using the optimized selection criteria the sensitivity of the search method has been computed: $E^2\,\Phi_{90} < 1.5 \times 10^{-6}\,GeV cm^{-2} s^{-1}$ ($E^2\,\Phi_{90} < 7.7 \times 10^{-6}\,GeV cm^{-2} s^{-1} sr^{-1}$ for the diffuse flux), that is about a factor of three better than the sensitivity obtained from the simulation of 2007 data. This enhancement comes from both the larger detector volume and the longer lifetime considered, with respect to 2007 data.
The present analysis has been performed without using the information on the event energy. The ANTARES experiment has been designed to detect neutrinos with energies higher than about 100 GeV: due to the fact that the atmospheric neutrino energy is thought to be steeper than the astrophysical one, the astrophysical spectrum is expected to overcome the atmospheric one at energies higher than some TeV, so that improvements are expected from the events classification in energy, that is also expected to lead to a reduction in the number of background events in both the ON and OFF regions.

Bibliography

[1] R. U. Abbasi *et al* . Observation of the GZK cutoff by the HiRes experiment. *Phys. Rev. Lett.*, 100:101101, 2008, astro-ph/0703099.

[2] R. U. Abbasi *et al* . Search for Correlations between HiRes Stereo Events and Active Galactic Nuclei. *Astropart. Phys.*, 30:175–179, 2008, arXiv:0804.0382.

[3] A. A. Abdo *et al* . Bright AGN Source List from the First Three Months of the Fermi Large Area Telescope All-Sky Survey. *Astrophys. J.*, 700:597–622, 2009, arXiv:0902.1559.

[4] S. Abe *et al* . Precision Measurement of Neutrino Oscillation Parameters with KamLAND. *Phys. Rev. Lett.*, 100:221803, 2008, 0801.4589.

[5] J. Abraham *et al* . Correlation of the highest-energy cosmic rays with the positions of nearby active galactic nuclei. *Astropart. Phys.*, 29:188–204, 2008, arXiv:0712.2843.

[6] J. Abraham *et al* . Observation of the suppression of the flux of cosmic rays above 4×10^{19}eV. *Phys. Rev. Lett.*, 101:061101, 2008, astro-ph/0806.4302.

[7] J. Abraham *et al* . Astrophysical Sources of Cosmic Rays and Related Measurements with the Pierre Auger Observatory. 2009, arXiv:0906.2347.

[8] J. Abraham *et al* . Limit on the diffuse flux of ultra-high energy tau neutrinos with the surface detector of the Pierre Auger Observatory. *Phys. Rev.*, D79:102001, 2009, arXiv:0903.3385.

[9] A. Achterberg *et al* . On the selection of AGN neutrino source candidates for a source stacking analysis with neutrino telescopes. *Astropart. Phys.*, 26:282–300, 2006, astro-ph/0609534.

[10] A. Achterberg *et al* . Multi-year search for a diffuse flux of muon neutrinos with AMANDA-II. *Phys. Rev.*, D76:042008, 2007, arXiv:0705.1315.

[11] M. Ageron *et al* . The ANTARES Optical Beacon System. *Nucl. Instrum. Meth. A*, 578:498–509, 2007, astro-ph/0703355.

[12] M. Ageron *et al* . Performance of the First ANTARES Detector Line. *Astropart. Phys.*, 31:277–283, 2009, arXiv:0812.2095.

[13] G. Aggouras *et al* . Recent results from NESTOR. *Nucl. Instrum. Meth.*, A 567:452–456, 2006.

[14] V. Agrawal, T. K. Gaisser, P. Lipari, and T. Stanev. Atmospheric neutrino flux above 1 GeV. *Phys. Rev. D*, 53(3):1314–1323, 1996.

[15] J. A. Aguilar and J. J. Hernandez-Rey. The expectation maximisation algorithm applied to the search for point sources of astroparticles. *Astropart. Phys.*, 29:117–124, 2008.

[16] J. A. Aguilar *et al* . Study of large hemispherical photomultiplier tubes for the antares neutrino telescope. *Nucl.Instrum.Meth.A*, 555:132, 2005.

[17] J. A. Aguilar *et al* . Transmission of light in deep sea water at the site of the Antares neutrino telescope. *Astropart. Phys.*, 23:131–155, 2005, astro-ph/0412126.

[18] J. A. Aguilar *et al* . The data acquisition system for the ANTARES neutrino telescope. *Nucl. Instrum. Meth.*, A570:107–116, 2007, astro-ph/0610029.

[19] Q. R. Ahamad *et al* . Direct evidence for neutrino flavor transformation from neutral-current interactions in the Sudbury Neutrino Observatory. *Phys. Rev. Lett.*, 89:011301, 2002, nucl-ex/0204008.

[20] Q. R. Ahamad *et al* . Measurement of day and night neutrino energy spectra at SNO and constraints on neutrino mixing parameters. *Phys. Rev. Lett.*, 89:011302, 2002, nucl-ex/0204009.

[21] F. Aharonian *et al* . High-energy particle acceleration in the shell of a supernova remnant. *Nature.*, 432:75–77, 2004.

[22] F. Aharonian *et al* . Microquasar LS 5039: a TeV gamma-ray emitter and a potential TeV neutrino source. *J. Phys. Conf. Ser.*, 39:408–415, 2006.

[23] F. Aharonian *et al* . Primary particle acceleration above $100 - TeV$ in the shell-type supernova remnant $RXJ1713.7-3946$ with deep HESS observations. *Astron. Astrophys.*, 464:235–243, 2007.

[24] F. Aharonian *et al* . Discovery of very high energy gamma-ray emission from Centaurus A with H.E.S.S. . *Astrophys. J. Lett.*, 695:L40-L44, 2009, arXiv:0903.1582.

[25] M. H. Ahn*et al* . Measurement of Neutrino Oscillation by the K2K Experiment. *Phys. Rev.*, D74:072003, 2006, hep-ex/0606032.

[26] J. Ahrens et al. Sensitivity of the IceCube detector to astrophysical sources of high energy muon neutrinos. *Astropart. Phys.*, 20:507–532, 2004, astro-ph/0305196.

[27] J. Ahrens *et al* . Muon Track Reconstruction and Data Selection Techniques in AMANDA. *Nucl. Instrum. Meth.*, A524:169–194, 2004, astro-ph/0407044.

[28] M. Ambrosio *et al* . High energy cosmic ray physics with underground muons in MACRO. I. Analysis methods and experimental results. *Phys. Rev. D*, 56:1407–1417, 1997.

[29] F. Ameli *et al* . The Data Acquisition and Transport Design for NEMO Phse I. *IEEE Transactions of Nuclear Science*, 55:233–240, 2008.

[30] P. Amram *et al* . The ANTARES optical module. *Nucl. Instrum. Meth.*, A484:369–383, 2002, astro-ph/0112172.

[31] P. Amram *et al* . Sedimentation and fouling of optical surfaces at the ANTARES site. *Astropart. Phys.*, 19:253–267, 2003, astro-ph/0206454.

[32] P. Antonioli, C. Ghetti, E. V. Korolkova, V. A. Kudryavtsev, and G. Sartorelli. A three-dimensional code for muon propagation through the rock: MUSIC. *Astropart. Phys.*, 7:357–368, 1997, hep-ph/9705408.

[33] M. Ave, J. A. Hinton, R. A. Vazquez, A. A. Watson, and E. Zas. New constraints from Haverah Park data on the photon and iron fluxes of UHE cosmic rays. *Phys. Rev. Lett.*, 85:2244–2247, 2000, astro-ph/0007386.

[34] J. N. Bahcall. *Neutrino Astrophysics*. Cambridge University Press, Cambridge, U.K., 1989.

[35] D. Bailey. Km3 v2r1: user guide - Internal note ANTARES-SOFT/2002-002.

[36] D. Bailey. Genhen v5r1 : Software Documentation. 2002.

[37] Bailey, D. *Monte Carlo tools and analysis methods for understanding the ANTARES experiment and predicting its sensitivity to dark matter*. PhD thesis, Wolfson College, Oxford, U.K., 2002.

[38] D. Band *et al* . BATSE Observations of Gamma-Ray Burst Spectra: I. Spectral Diversity. *Ap. J.*, 413:281–292, 1993.

[39] A. S. Barabash. Double beta decay: present status. 2008, arXiv:0807.2948.

[40] B. Baret for the ANTARES Collaboration. Charge Calibration of the ANTARES high energy neutrino telescope. 2009, arXiv:0908.0810.

[41] S. W. Barwick *et al* . Constraints on cosmic neutrino fluxes from the ANITA experiment. *Phys. Rev. Lett.*, 96:171101, 2006, astro-ph/0512265.

[42] Y. Becherini, A. Margiotta, M. Sioli, and M. Spurio. A parameterisation of single and multiple muons in the deep water or ice. *Astropart. Phys.*, 25:1–13, 2006, hep-ph/0507228.

[43] J. K. Becker. High-energy neutrinos in the context of multimessenger physics. *Phys. Rept.*, 458:173–246, 2008, arXiv:0710.1557.

[44] J. K. Becker and P. L. Biermann. Neutrinos from active black holes, sources of ultra high energy cosmic rays. *Astropart. Phys.*, 31:138–148, 2009, arXiv:0805.1498.

[45] P. L. Biermann and P. A. Strittmatter. Synchrotron emission from shock waves in active galactic nuclei. *Astrophys. J.*, 322:643–649, 1987.

[46] J. Bluemer for the Pierre Auger Collaboration. The Pierre Auger Observatory: Results on Ultra-High Energy Cosmic Rays. 2008, arXiv:0807.4871.

[47] G. Bossard *et al* . Cosmic Ray Air Shower Characteristics in the Framework of the Parton-Based Gribov-Regge Model NEXUS. 2000, hep-ph/0009119.

[48] M. Bouwhuis for the ANTARES Collaboration. Concepts and performance of the Antares data acquisition system. 2009, arXiv:0908.0811.

[49] A. M. Brown for the ANTARES Collaboration. Positioning system of the ANTARES Neutrino Telescope. 2009, arXiv:0908.0814.

[50] J. Brunner. Analysis of 2007 and 2008 data with BBfit - Internal note ANTARES-PHYS/2009-006.

[51] J. Brunner. Simulation of ^{40}K signals - Internal note ANTARES-Site/1999-002.

[52] J. Brunner. The BBFit Reconstruction algorithm - Internal note ANTARES-SOFT/2009-003.

[53] E. V. Bugaev *et al* . Atmospheric muon flux at sea level, underground, and underwater. *Phys. Rev. D*, 58, 1998.

[54] Bunner, A. N. *Cosmic Ray Detection by Atmospheric Fluorescence*. PhD thesis, Cornell University, 1967.

[55] A. Capone *et al* . Recent results and perspectives of the NEMO project. *N.I.M. A*, 602:47–53, 2009.

[56] G. Carminati, A. Margiotta, and M. Spurio. MUons from PArametric formulas: A fast GEnerator of atmospheric mu-bundles for neutrino telescopes (MUPAGE). *Nucl. Instrum. Meth.*, A602:95–97, 2009.

[57] J. Carr. Data from the ANTARES Neutrino Telescope. *J. Phys. Conf. Ser.*, 136:022047, 2008.

[58] S. Cecchini. Comparison of primary cosmic ray energy spectra used in atmospheric cascade simulations, Internal note ANTARES-PHYS/2009-001.

[59] B. T. Cleveland *et al* . Measurement of the solar electron neutrino flux with the Homestake chlorine detector. *Astrophys. J.*, 496:505–526, 1998.

[60] T. DeYoung. Neutrino Astronomy with IceCube. *Mod. Phys. Lett.*, A24:1543–1557, 2009, arXiv:0906.4530.

[61] T. DeYoung *et al* . Results from Seven Years of AMANDA-II. *J. Phys. Conf. Ser.*, 136:022046, 2008, arXiv:0810.4513.

[62] D. Dornic and G. Lelaizant. Individual GRB sensitivity of a cubic-kilometer deep-sea neutrino telescope KM3NeT. *Nucl. Instrum. Meth.*, A602:123–125, 2009, arXiv:0810.1452.

[63] S. Escoffier. Bioluminescence studies with the ANTARES Protoype Sector Line - Internal note ANTARES-Site/2005-001.

[64] H. Falcke *et al* . Prospects for radio detection of ultra-high energy cosmic rays and neutrinos. *New Astr. Rev.*, 48:1487–1510, 2004.

[65] G. J. Feldman and R. D. Cousins. Unified approach to the classical statistical analysis of small signals. *Phys. Rev. D*, 57(7):3873–3889, 1998.

[66] R. Fisher. Combining independent tests of significance. *American Stat.*, 2:30, 1948.

[67] G. L. Fogli *et al* . Observables sensitive to absolute neutrino masses (Addendum). *Phys. Rev. D*, 78:033010, 2008, arXiv:0805.2517.

[68] C. Forti *et al* . Simulation of atmospheric cascades and deep-underground muons. *Phys. Rev. D*, 42:3668, 1990.

[69] Y. Fukuda *et al* . Evidence for oscillation of atmospheric neutrinos. *Phys. Rev. Lett.*, 81:1562–1567, 1998, hep-ex/9807003.

[70] T. K. Gaisser. *Cosmic Rays and Particle Physics.* Cambridge University Press, Cambridge, U.K., 1990.

[71] R. Gandhi *et al* . Ultrahigh-energy neutrino interactions . *Astroparticle Physics*, 5:81–110, 1996.

[72] D. S. Gorbunov *et al* . On the interpretation of the cosmic-ray anisotropy at ultra-high energies. 2008, arXiv:0804.1088.

[73] P. W. Gorham, K. M. Liewer, and C. J. Naudet. Initial Results from a Search for Lunar Radio Emission from Interactions of >= 10^{19} eV Neutrinos and Cosmic Rays. 1999, astro-ph/9906504.

[74] K. Greisen. End to the cosmic ray spectrum? *Phys. Rev. Lett.*, 16:748–750, 1966.

[75] F. Halzen and A. O'Murchadha. Neutrinos from Auger Sources. 2008, arXiv:0802.0887.

[76] Hartmann, B. . *Reconstruction of neutrino-induced hadronic and electromagnetic showers in the ANTARES experiment.* PhD thesis, Erlangen University, Erlangen, Germany, 2006.

[77] D. Heck *et al* . Extensive Air Shower Simulations with CORSIKA: A User's Guide. 2009, available at http://www-ik.fzk.de/corsika.

[78] Heijboer, A. J. *Track Reconstruction and Point Source Searches with ANTARES.* PhD thesis, Amsterdam University, Amsterdam, The Netherlands, 2004.

[79] G. Hill and K. Rawlins. Unbiased cut selection for optimal upper limits in neutrino detectors: the model rejection potential technique. *Astropart. Phys.*, 19:393–402, 2003.

[80] J. R. Hoerandel. On the knee in the energy spectrum of cosmic rays. *Astropart. Phys.*, 19:193–220, 2003, astro-ph/0210453.

[81] P. J. Huber. *Robust Statistics*. Wiley, 1981.

[82] G. Ingelman, A. Edin, and J. Rathsman. LEPTO 6.5 - A Monte Carlo Generator for Deep Inelastic Lepton-Nucleon Scattering. *Comput. Phys. Commun.*, 101:108–134, 1997, hep-ph/9605286.

[83] K.-H. Kampert. Cosmic rays from the knee to the ankle: Status and prospects. *Nucl. Phys. Proc. Suppl.*, 165:294–306, 2007, astro-ph/0611884.

[84] A. Kappes, J. Hinton, C. Stegmann, and F. A. Aharonian. Potential Neutrino Signals from Galactic Gamma-Ray Sources. *Astrophys. J.*, 656:870–896, 2007, astro-ph/0607286.

[85] A. Kappes *et al* . KM3NeT: A Next Generation Neutrino Telescope in the Mediterranean Sea. 2007, arXiv:0711.0563.

[86] B. Kayser. Neutrino Oscillation Phenomenology. 2008, arXiv:0804.1121.

[87] B. Konovalov. Yakutsk Institute's cosmic ray research facility. *USSR Report Space*, pages 44–45, 1984.

[88] M. Kowalski and A. Mohr. Detecting neutrino transients with optical followup observations. *Astropart. Phys.*, 27:533–538, 2007.

[89] I. Kravchenko et al. Event Reconstruction and Data Acquisition for the RICE Experiment at the South Pole. 2007, arXiv:0705.4491.

[90] R. Lahmann for the ANTARES Collaboration. Status and First Results of the Acoustic Detection Test System AMADEUS. 2009, arXiv:0901.0321.

[91] J. G. Learned. DUMAND and other high energy neutrino astronomy projects. Prepared for International Symposium on Neutrino Astrophysics, Takayama / Kamioka, Japan, 19-22 Oct 1992.

[92] J. G. Learned and K. Mannheim. High-Energy Neutrino Astrophysics. *Annu. Rev. Part. Sci.*, 50:679–749, 2000.

[93] Lelaizant, G. . *Étude des Sursauts Gamma à partir des neutrinos de haute-énergie avec le télescope ANTARES -Analyse du positionnement acoustique du détecteur* . PhD thesis, Université de la Méditérranée- Aix Marseille II , Marseille, France, 2008.

[94] G. Lim for the ANTARES Collaboration. First results on the search for dark matter in the Sun with the ANTARES neutrino telescope. 2009, arXiv:0905.2316.

[95] J. Linsley. The cosmic ray spectrum above 10(19) EV at Volcano Ranch and Haverah Park. In F. C. Jones, editor, *International Cosmic Ray Conference*, volume 9 of *International Cosmic Ray Conference*, pages 475–+, 1986.

[96] P. Lipari and T. Stanev. Propagation of multi-TeV muons. *Phys. Rev. D*, 44:3543–3554, 1991.

[97] M. S. Longair. *High Energy Astrophysics vol. 1 , 2.* Cambridge University Press, Cambridge, U.K., 1981.

[98] K. Mannheim *et al* . Cosmic ray bound for models of extragalactic neutrino productio . *Phys. Rev. D*, 63, 2001.

[99] D. G. Michael *et al* . Observation of muon neutrino disappearance with the MINOS detectors and the NuMI neutrino beam. *Phys. Rev. Lett.*, 97:191801, 2006, hep-ex/0607088.

[100] Naumann-Godo, M. *Sensitivity of the Antares neutrino telescope to gamma-ray bursts* . PhD thesis, Erlangen University, Erlangen, Germany, 2007.

[101] S. I. Nikolsky *et al* . Composition of cosmic radiation at energies approximately 10^{15} eV and above. *Sov. Phys. JETP*, 60, 1984.

[102] E. W. Otten and C. Weinheimer. Neutrino mass limit from tritium beta decay. *Rept. Prog. Phys.*, 71:86–201, 2008.

[103] G. Pavalas and N. Picot Clemente for the ANTARES Collaboration. Search for Exotic Physics with the ANTARES Detector. 2009, arXiv:0908.0860.

[104] T. Piran. Gamma-Ray Bursts and the Fireball Model. *Phys. Rept.*, 314:575–667, 1999, astro-ph/9810256.

[105] W. H. Press. *Numerical Recipes in C.* Cambridge University Press, Cambridge, U.K., 1993.

[106] J. P. Rachen and P. L. Biermann. Extragalactic ultrahigh-energy cosmic rays. 1. Contribution from hot spots in FR-II radio galaxies. *Astron. Astrophys.*, 272:161–175, 1993, astro-ph/9301010.

[107] J. P. Rachen, R. J. Protheroe, and K. Mannheim. The relation of extragalactic cosmic ray and neutrino fluxes: The logic of the upper bound debate. 1998, astro-ph/9908031.

[108] F. Rademakers, M. Goto, P. Canal, and R. Brun. Root status and future developments. *CoRR*, cs.SE/0306078, 2003.

[109] J. Ranft. Baryon stopping in high energy collisions and the extrapolation of hadron production models to Cosmic Ray energies. *Phys. Rev. D*, 51:64, 1995, hep-ph/0002137.

[110] G. Riccobene and A. Capone. Deep seawater inherent optical properties in the southern Ionian Sea. *Astropart. Phys.*, 27:1–9, 2007, astro-ph/0603701.

[111] D. Saltzberg et al. Observation of the Askaryan effect: Coherent microwave Cherenkov emission from charge asymmetry in high energy particle cascades. *Phys. Rev. Lett.*, 86:2802–2805, 2001, hep-ex/0011001.

[112] E. Scapparone. HEMAS: a Monte Carlo code for hadronic, electromagnetic and TeV muon components in air shower, 1999.

[113] T. Schwetz, M. A. Tortola, and J. W. F. Valle. Three-flavour neutrino oscillation update. *New J. Phys.*, 10:113011, 2008, arXiv:0808.2016.

[114] G. Sigl, D. N. Schramm, and P. Bhattacharjee. On the origin of highest energy cosmic rays. *Astropart. Phys.*, 2:401–414, 1994, astro-ph/9403039.

[115] T. Sjostrand, S. Mrenna, and P. Skands. PYTHIA 6.4 Physics and Manual. *JHEP*, 05:026, 2006, hep-ph/0603175.

[116] C. Spiering. Future high-energy neutrino telescopes . *Nucl. Phys. Proc. Suppl.*, 91:445–452, 2001, astro-ph/0012532.

[117] T. Stanev. A comment on the Auger events correlation with AGN. 2008, arXiv:0805.1746.

[118] T. Stanev, P. L. Biermann, J. Lloyd-Evans, J. P. Rachen, and A. A. Watson. The arrival directions of the most energetic cosmic rays. *Phys. Rev. Lett.*, 75:3056–3059, 1995, astro-ph/9505093.

[119] The ANTARES Collaboration. A deep sea telescope for high energy neutrinos. astro-ph/9907432.

[120] S. Toscano. Golden-list for a point source search in ANTARES - Internal note ANTARES-PHYS/2009-002.

[121] J. Vandenbroucke, G. Gratta, and N. Lehtinen. Experimental study of acoustic ultra-high-energy neutrino detection. *Astrophys. J.*, 621:301–312, 2005, astro-ph/0406105.

[122] M. Vecchi, A. Capone, and J. P. Schuller. in preparation.

[123] M. P. Véron Cetty and P. Véron. A catalogue of quasars and active nuclei: 12th edition. *Astron. Astrophys.*, 455:773–777, 2006.

[124] E. Waxman and J. N. Bahcall. High energy neutrinos from astrophysical sources: An upper bound. *Phys. Rev. D*, 59:023002, 1999, hep-ph/9807282.

[125] J. Wdowczyk and A. W. Wolfendale. Predicted anisotropy in the arrival directions of cosmic gamma-rays at 10**14-eV. *J. Phys.*, G16:1399–1407, 1990.

[126] R. Wischnewski *et al* . The BAIKAL neutrino experiment - physics results and perspectives. 2008, arXiv:0811.1109.

[127] G. T. Zatsepin and V. A. Kuzmin. Upper limit of the spectrum of cosmic rays. *JETP Lett.*, 4:78–80, 1966.

Ringraziamenti

Questo lavoro di tesi è dedicato prima di tutto ai miei genitori, è grazie al loro sostegno e al loro affetto che ho potuto intraprendere questa strada.
Alla fine di questo lungo lavoro vorrei ringraziare il Prof. Antonio Capone per il costante interesse ed incoraggiamento verso il mio lavoro di ricerca, nonché per le oppurtunità di confronto e discussione che mi sono state offerte all'interno del gruppo ANTARES di Roma.
Un caloroso ringraziamento va al Dr. Fabrizio Lucarelli, sotto la cui paziente supervisione ho svolto il mio lavoro di ricerca nell'ultimo anno di dottorato.
Nella fase iniziale del mio lavoro all'interno della Collaborazione ANTARES un prezioso aiuto mi è stato offerto da Niccolò Cottini, che mi ha dato una mano a districarmi tra le "trappole" del software di ANTARES.
Questo di lavoro di tesi è stato possibile anche grazie ai consigli di Giada Carminati e di Annarita Margiotta, che mi hanno iniziata al mondo delle tecniche di simulazione e in particolare ai programmi usati all'interno della Collaborazione ANTARES.
Un enorme grazie va a Carla Distefano, per la sua disponibilità e i suoi suggerimenti, che si sono rivelati fondamentali per lo studio della sensibilità, del model rejection factor e del discovery potential.

I am really grateful to all the members of the ANTARES Collaboration for sharing with me this exciting experience. I would like to thank in particular all the people who were involved in the unblinding procedure of this analysis: Dr. Paschal Coyle, the ANTARES Spokesperson, and Dr. Juan Jose Hernandez-Rey, the ANTARES Deputy Spokesperson, Dr. Alexander Kappes, who was appointed as internal referee for this analysis, Dr. Juan de Dios Zornoza-Gomez and Dr. Antoine Kouchner, coordinators of the Astronomy Working Group.